Fault Diagnosis and Fault Handling for Autonomous Aircraft

Hansen, Søren; Blanke, Mogens; Adrian, Jens

Publication date:
2012

Document Version
Publisher's PDF, also known as Version of record

Technical University of Denmark

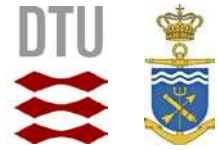

Søren Hansen

Fault Diagnosis and Fault Handling for Autonomous Aircraft

PhD thesis, October 2012

DTU Electrical Engineering
Department of Electrical Engineering

www.elektro.dtu.dk
Department of Electrical Engineering
Automation and Control (AUT)
Technical University of Denmark
Elektrovej
Building 326
DK-2800 Kgs. Lyngby
Denmark
Tel: (+45) 45 25 35 76
Fax: (+45) 45 88 12 95
Email: info@elektro.dtu.dk

ISBN 978-87-92465-61-0

Summary

Unmanned Aerial vehicles (UAVs) or drones are used increasingly for missions where piloted aircraft are unsuitable. The unmanned aircraft has a number of advantages with respect to size, weight and manoeuvrability that makes it possible for them to solve tasks that an aircraft previously has been unable to solve. The primary cause that UAVs has reached the current level of development is their military potential. Both for surveillance operations and direct strikes, UAVs has many benefits compared to manned aircraft, and the biggest of those are that no pilots are put in direct contact with enemy troops. Gradually UAV's are also being introduced in civilian applications. In this setting they have reduced the difficulty of tasks such as photo inspections of large buildings and rescue missions at sea. All in all UAVs have shown their great potential within the recent years.

The increasing use of UAVs causes them to coexist with manned aircraft and in areas where humans are present on ground. This of course carries demands to the safety and reliability of the aircraft. It is inevitable that components onboard a UAV will fail at some point in time. When this happens it is important that the fault is discovered in time such that appropriate actions can be taken. That could either be the aircraft controlling computer taking the fault into account or a human operator that intervenes. Detection of faults that occur during flight is exactly the subject of this thesis.

Safety towards faults for manned aircraft is often achieved by making most of the systems onboard redundant. This is an easy way to obtain safety since no single system fault is catastrophic. The failed subsystem can be disconnected and the redundant systems can take over the tasks of the failed system. For smaller UAVs both price and weight of the aircraft is very important meaning that redundant hardware will not be an applicable safety solution. This is why focus of this thesis have been on methods where redundancies are obtained by models and knowledge about the aircraft behaviour.

Based on telemetry data from a specific UAV, used by the Danish military, it is investigated how a number of critical faults can be detected and handled.

One of the challenges using telemetry data for the fault diagnosis is the limited bandwidth in the radio link between the aircraft and the base-station on ground. This combined with noise on the signals makes it difficult to use precise models for the fault diagnosis. This is solved by using statistical distributions to describe the aircraft's normal behaviour and deviations from this, indicating different faults.

To increase the applicability of the models, used for fault diagnosis, these are adaptive to some extent. This makes small discrepancies between aircraft and wind conditions to have less influence on the performance of the fault diagnosis with respect to time to detect and false alarms. It also means that less adjustment is needed if the methods should be applied to another type of aircraft with different parameters.

Amongst the main findings of this research project is a method to handle faults on the UAV's pitot tube, which measures the aircraft speed. A set of software redundancies based on GPS velocity information and engine thrust are used to detect abnormal airspeed signals. Another contribution worth mentioning considers diagnosis of control surface faults. Here a set of low-complexity models between the aircraft's turn rates and input deflections are used in the fault detection. Both methods has been verified against data from incidents where the respective faults occurs, and show good potential.

The thesis consists of a summary of the different methods, investigations and results obtained during the project. Detailed descriptions are found in a number of papers submitted to research conferences and journals during the project. These have been enclosed in the last part of the thesis.

Resumé

Ubemandede flyvemaskiner (UAV'er) eller droner bliver i stigende grad brugt i missioner hvor bemandede fly ikke egner sig. De ubemandede fly har en række fordele med hensyn til størrelse, vægt og manøvredygtighed som gør at de kan løse opgaver som fly før i tiden ikke kunne løse. Den primære årsag til at udviklingen af UAV'er er nået til det niveau vi ser i dag er at militæret har set potentialet i dem. Både til overvågnings operationer og direkte angreb har UAV'erne mange fordele frem for de bemandede fly, hvoraf den største nok er at piloterne ikke direkte kommer i kontakt med fjenden. Efterhånden har UAV'erne dog også fundet vej til civil anvendelse. Her har de kunne lette opgaver som foto-inspektion af store bygningsværker og redningsaktioner til havs. Alt i alt har UAV'er inden for de sidste år vist deres mangfoldige potentiale.

Den stigende brug af UAV'er betyder også at de skal færdes sammen med bemandede fly og i områder hvor mennesker færdes på jorden. Dette stiller selvsagt nogle krav til flyenes sikkerhed og pålidelighed. Det er uundgåeligt at komponenter ombord på en UAV på et eller andet tidspunkt vil fejle. Når dette sker, er det vigtigt at fejlen opdages i tide således at en passende indgriben kan iværksættes. Enten kan flyets styrecomputer tage højde for den opståede fejl eller en menneskelig operatør kan gribe ind. Detektion af fejl der opstår under flyvningen er netop emnet for denne afhandling.

For bemandede fly består sikkerheden overfor fejl ofte i at de fleste systemer ombord er redundante. Derved opnår man let en høj grad af sikkerhed da fejl på et enkelt system ikke er katastrofale. Det fejlede delsystem kan udkobles og de redundante systemer kan overtage det fejlede systems opgave. For mindre UAV'er hvor både pris og flyets vægt er af høj betydning vil redundant hardware i mange tilfælde ikke være en brugbar sikkerhedsløsning. Derfor er der i denne afhandling fokuseret på metoder hvor redundanser i stedet opnås ved hjælp af modeller og viden om flyets opførsel.

Med udgangspunkt i telemetri data fra en specifik UAV, benyttet af det danske forsvar, undersøges hvordan en række kritiske fejl kan detekteres og håndteres. En af udfordringerne ved at benytte telemetri data til fejldiagnose er den be-

grænsede båndbredde i radioforbindelsen mellem flyet og base-stationen på jorden. Sammen med denne begrænsning gør støj på de enkelte signaler det vanskeligt at bruge præcise modeller til fejldiagnosen. Dette er løst ved at bruge statistiske fordelinger til at beskrive flyets normale opførsel og afvigelser fra denne, som indikerer forskellige fejl.

For at øge anvendeligheden er de modeller, der bliver brugt til fejldiagnose, til en hvis grad selvindstillende. Det gør at mindre afvigelser mellem fly og vindforhold ikke har så stor indflydelse på fejldiagnosens ydelse i form af detektions tid og afvisning af falske alarmer. Det betyder også mindre justering hvis metoderne skal anvendes på en ny type fly med andre parametre.

Et af hovedresultaterne af dette forskningsprojekt er en metode der kan finde fejl på en UAV's pitot rør, der måler flyets hastighed. En række software redundanser baseret på hastigheds information fra GPS samt motorens trækkraft bruges til at detektere unormale hastigheds signaler. Et andet bidrag, der er værd at nævne, omhandler diagnose af fejl på styreflader. Her benyttes en række modeller med lav kompleksitet mellem flyets drejehastigheder og styrefladernes udslag til fejldetektionen. Begge metoder er blevet verificeret mod data fra hændelser hvor de respektive fejl optræder, og viser lovende resultater.

Afhandling består af et resume af de forskellige metoder, undersøgelser og resultater fundet i forbindelse med projektet. Mere detaljerede beskrivelser findes i en række artikler indsendt til videnskabelige konferencer og tidsskrifter i løbet af projektet. Disse er vedlagt i sidste del af afhandlingen.

Preface

This thesis is written as conclusion of my PhD project at Technical University of Denmark, Department of Electrical Engineering. The research of this project was carried out from June 2009 to October 2012. The main supervisor of the project was Professor Mogens Blanke.

The project was funded by the Danish Naval Weapons School. The project was co-supervised by B.Sc.E. Jens Adrian, head of research and development at the Danish Forces Joint UAV Team.

This thesis constitutes a collection of research articles which has been submitted for conferences and journals during the course of the PhD project. The articles follow a brief summary of related work and the main results obtained during the project.

The subject of the thesis is fault diagnosis for unmanned aircrafts. The main focus has been on developing methods which uses telemetry data from an unmanned aircraft to detect faults in sensors and actuators. The methods can be used as an aid to aircraft operator or as part of a fault tolerant control system.

Søren Hansen
Lyngby, 2012

List of Publications

Papers included in the thesis

The following papers are included in the thesis. They are listed in order of submission.

(A) S. Hansen, M. Blanke and J. Adrian. Diagnosis of UAV Pitot Tube Defects Using Statistical Change Detection. In *proceedings of 7th Symposium on Intelligent Autonomous Vehicles*, 2010.

(B) S. Hansen and M. Blanke. Control Surface Fault Diagnosis for Small Autonomous Aircraft. In *proceedings of 1st Australian Control Conference*, 2011.

(C) T. Hahn, S. Hansen and M. Blanke. Contingency Estimation of States for Unmanned Aerial Vehicle using a Spherical Simplex Unscented Filter. In *proceedings of 16th IFAC Symposium on System Identification*, 2012.

(D) S. Hansen and M. Blanke. In-flight Fault Diagnosis for Autonomous Aircraft via Low-rate Telemetry Channel. In *proceedings of 8th IFAC Symposium on Fault Detection, Supervision and Safety for Technical Processes*, 2012.

(E) S. Hansen and M. Blanke. Diagnosis of Airspeed Measurement Faults for Unmanned Aerial Vehicles. *IEEE Transactions on Aerospace and Electronic Systems*, 2012. Submitted.

(F) P. de Lamberterie, S. Hansen, T. Perez and M. Blanke. A Low-complexity Actuator Fault-tolerant Flight Controller for Unmanned Aircraft. *IEEE Transactions on Aerospace and Electronic Systems*, 2012. Submitted.

Papers not included in the thesis

The following papers were published during the study but not included in the thesis.

- S. Hansen, E. Bayramoglu, J. C. Andersen, O. Ravn, N. A. Andersen and N. K. Poulsen. Orchard Navigation using derivative free Kalman filtering. In *proceedings of the 2011 American Control Conference*, 2011.
- M. Blanke, S. Hansen and M. R. Blas. Diagnosis for Control and Decision Support in Complex Systems. In *Special International Conference on Complex Systems: Synergy of Control, Communications and Computing*, 2011.
- E. Bayramoglu, S. Hansen, O. Ravn and N. K. Poulsen. Derivative free filtering using Kalmtool. In *13th International Conference on Information Fusion*, 2010.
- S. Hansen, E. Bayramoglu, J. C. Andersen, O. Ravn, N. A. Andersen, N. K. Poulsen. Derivative free Kalman filtering used for orchard navigation. In *proceedings of 13th International Conference on Information Fusion, Edinburgh*, 2010.
- L. V. Mogensen, S. Hansen, O. Ravn, N. K. Poulsen. Comparing mobile robot localisation algorithms using Kalmtool. In *proceedings of 15th IFAC Symposium on System Identification*, 2009.
- L. V. Mogensen, S. Hansen, J. C. Andersen, O. Ravn, N. A. Andersen, M. Blanke, N. K. Poulsen. Kalmtool used for laser scanner aided navigation in orchard. In *proceedings of 15th IFAC Symposium on System Identification*, 2009.
- S. Hansen, M. Blanke and J. C. Andersen. Autonomous Tractor Navigation in Orchard - Diagnosis and Supervision for Enhanced Availability. In *proceedings of 7th IFAC Symposium on Fault Detection, Supervision and Safety of Technical Processes*, 2009.

Acknowledgements

I would like to thank my main supervisor Professor Mogens Blanke for the time and guidance he has given me during this PhD project. He has always been prepared to discus and guide me through the different challenges during the project. With a positive and humoristic attitude he has disseminated his knowledge in a very inspirational manner.

I would also like to thank my company supervisor B.Sc.E Jens Adrian from the Naval Weapons School. His enthusiastic approach to technical problems has been very motivating and his large knowledge within all sorts of engineering systems has been a great help.

I would also like to thank Associate Professor Tristan Perez, who was my supervisor during my visit to The University of Newcastle in Australia. He made me feel very welcome on the other side of the planet and I had a very rewarding cooperation with him. Thanks should also go to his group for contributing to a fun and inspirational working environment, especially Pierre de Lamberterie for the good collaboration we had.

My colleagues at my work places both at Technical University of Denmark (DTU) in Lyngby and at the Naval Weapons School at Sjællands Odde should be acknowledged for always making it fun and interesting to go to work. The people at the Automation and Control Group at DTU-Elektro have made it possible for me to participate in interesting research and problem solving on a high level. At the Joint Drone Team at Sjællands Odde the people has always shown interest in my project and helped me with my "crazy" experiments.

I would also like to thank the people at the Danish Navy involved in setting up the funding and framework for my project.

Finally I would like to thank my family for their interest and support during the course of my project.

Contents

List of Figures

Chapter 1

Introduction

Small Unmanned Aerial Vehicles has potential in a great number of applications both for military and civil purposes. The potential of having a small autonomous flying unit that is easy to operate, is build from relatively cheap materials and can move around with the freedom of a bird is very large. Mainly due to recent development in technologies, especially Micro-Electro-Mechanical Systems (MEMS) it is possible to buy an inertial navigation suit featuring accelerometers, gyros and magnetometers in all three axes at a very affordable price. Adding a standard GPS receiver and a small computer with interface to the actuators, one has all that is needed to make a remote controlled hobby aircraft fly autonomously. At least in theory, though, because to achieve this practically means solving a variety of theoretical and technical issues.

One of the challenges when dealing with aircraft, manned as well as unmanned, is that they are extremely sensitive when a component of the craft fails. A simple sensor that suddenly starts giving faulty signals can very easy lead to a catastrophic event. This is why the use and maintenance of aircraft today are controlled meticulously. There are precise routines that must be performed before each take-off and in case of a problem en route an already prepared procedure must be conducted. Furthermore, each flight has to be approved by the authorities controlling the airspace, in particular in a crowded airspace.

On the technical side aircraft have redundancies of the vital systems, such that in case of an issue in one system or sensor that can be switched off and the remaining parts can be used instead. The switch-over can sometimes be done automatically, or by the pilot that follows predefined procedures.

This level of safety is not present when dealing with UAV's, in particular UAV's of the cheaper categories. Since flight time and weight are counteracting each other the lighter an aircraft can be constructed the longer is the endurance.

Therefore adding double or even triple redundant systems on a small UAV might make it unusable for its purpose. These simple constructions are fine as long as each system is working as intended, but when the inevitable fault happens while flying, the aircraft might crash. Because of this the usage of UAV's in many countries, which Denmark is amongst, is very limited.

Because of the big potential in using UAV's a lot of people and organisations are pushing to open the airspace more. But the risks involved in UAV flight are not neglected and several organisations have looked at the UAV's safety [130]. A couple of the milestones on the road to achieving this are to insure sufficient safety and reliability of the drones and a more elaborate education of the operators. With respect to safety it is vital that the UAV is equipped with the capability to detect faults and procedures to accommodate them.

1.1 Background

The project described in this thesis was started on the basis of an event leading to a loss of one of the Danish navy's target drones of the Banshee type (Figure 1.1). The drone was flying as a part of a mission to train the crew of a frigate to deal with airborne threats. At around 20 minutes into the otherwise normal flight the drone started speeding up and in a banking manoeuvre shortly after it crashed. The investigation of the incident found that the airspeed sensor of the drone was faulty. The investigation also showed that the fault was apparent from the data the aircraft sent to the operator at ground for long enough time for him to react. But because the interface he is using for operating the drone is focused on flying the mission and not on health monitoring of the aircraft, it is very hard for him to spot that something is wrong.

1.2 Objectives

The diagnosis of faults on the drone's data stream, the so-called telemetry, could with advantage be done by a computer. Then the operator could focus on performing his mission and only when the computer indicates problems he needed to concentrate on fault handling. The investigation in this project is then to find out which faults can be diagnosed from telemetry and are the diagnosis early enough for the operator to react on them.

The objective of this research project is to investigate whether critical faults can be detected using only the telemetry data coming from the aircraft. This would facilitate timely operator intervention that could save aircraft. Alternatively it might be possible to implement fault-tolerance in the autopilot controlling the aircraft, and thereby take faults into account automatically. This would mean

Figure 1.1: Banshee drone is prepared for launch during a training exercise for the Danish military.

that the software of the autopilot should be rewritten, which in some cases might not be feasible. The drones operated by the Danish navy are bought 'as is' in the sense you get a full package including the aircraft and all its components, a ground station and various other equipment used in the daily operation of the drone. The autopilot is bought as a part of the full package and can only be changed if the company selling the drones chooses to. Listening to the telemetry on the other hand only requires knowledge of the protocol and is therefore much less intrusive and can be implemented as a supervisory function in the ground station software.

1.3 Literature survey

Fault detection and isolation (FDI) of control systems and technical processes has been an active research field since the 1970s and recently, several methods using systematic approaches have been developed. The basis of these methods is laid in [54] and [70], amongst others. This has also led to several textbooks being published in the area. Among those are textbooks by Basseville and Nikiforov [8], Gustafsson [61], Isermann [72], Blanke, Kinnaert, Lunze and Staroswieki [19] and Ding [41].

Fault diagnosis for aircrafts and in particular fault tolerant control for aircrafts has been researched vastly and is still interesting as new methods are found, faster computers and better sensors are developed. For UAV's the field is also maturing as the UAV themselves mature and become available for more and more applications. In 2009, Ducard [44] gave a thorough insight in one way of making the control system of an UAV tolerant towards faults. The focus of the book was on actuator faults, since these directly affect the UAV's ability to manoeuvre. Reconfigurations of the control and guidance systems were done to accommodate the reduced capabilities of the aircraft. The FDI was achieved by using an extended version of multiple model adaptive estimation (MMAE) first reported in [87]. The drawbacks of the standard MMAE approach and the enhancements made by the authors were presented in [43]. The faults were modelled as an unknown signal controlling the actuators, which were then estimated by extended Kalman filters in the enhanced MMAE method.

The interest in fault tolerant capabilities for UAV's overlaps with the same interest for conventional aircrafts as many of the methods can be employed regardless of whether the aircraft is manned or not. A recent overview [47] highlights the major advances in the recent years within the field of fault tolerant control for both manned and unmanned aircrafts. The book focuses on both theoretical fault diagnosis and accommodation methods and application of the theories to different aircraft systems. One of the subjects of the book is online model identification. The so-called two-step identification procedure where the aircraft states based on kinematics are estimated first and based on these estimates the remaining aerodynamic parameters are estimated. If instruments of sufficient precision are available onboard the aircraft this method works well for identifying the model. Using a Recursive Least Squares (RLS) parameter estimation method ensures easy implementation. The method was shown working with a model based flight controller but only operational, in the event of an actual fault. Another topic of the book was the use of sliding mode control (SMC) and sliding mode observer to achieve fault tolerant flight control. Implementation of fault tolerant controllers for different flight simulators based on civil aircraft were shown, amongst those the Boeing 747. The controllers were shown to work well in simulation of both nominal and flights with both structural damage and loss of power. No reconfiguration was needed when faults occur as the same controller handles both faulty and the nominal case. A further elaboration of sliding modes used in connection with aircraft control is given later in the section. The Boeing 747 model has also been analysed with respect to actuator failures with residual based methods with respect to the model of [89]. Assessment of different fault tolerant flight control systems were also discussed in the book. A benchmark based on both diagnosis performance such as detection time and false alarm ratio is combined with four different flight scenarios containing both flight and landing manoeuvres are presented. The flight scenarios are chosen such that different flight characteristics are triggered which makes the assessment able to

pin-point particular advances or disadvantages of the tested methods.

In [103] fault diagnosis for general aerospace applications were discussed. An overview of different approaches to diagnosis was given with emphasis on model based techniques to form analytic redundancies. Statistical hypothesis test like the General Likelihood Ratio Test (GLRT) were employed to decide between multiple hypotheses signifying faulty parts of the aircraft. The development in model based approaches for fault detection and isolation [71] has recently spawn a number of different approaches for aircrafts.

In [40] a simplified model of a vertical takeoff and landing aircraft exposed to actuator faults were considered. Using a geometric approach ([39]) a residual generator consisting of an observable subspace of the true plant model, which was not affected by disturbances was found. It was shown in the paper that fault isolation was possible using the method. However actual detectors for the residuals as well as the effect of noisy measurements were not considered.

Further investigation of the geometric approach was done in [17] where the method was compared to a polynomial approach to residual generation for an aircraft application. Also disturbance decoupling of residuals based on data-driven methods such as neural networks and model based approaches based on Kalman filter descriptions were considered in the comparison. Actuator faults were considered in the analysis and the research showed that each of the tested methods performance was comparable both with regard to detection time and robustness towards false alarms.

In [120] a small radio controlled model aircraft was used to test a recursive parameter identification scheme for identifying the aircrafts parameters, both under nominal conditions and when faults were present. The paper focused on actuator and general aircraft failures such as engine loss or issues with the aircrafts structural integrity. It was shown that a recursive least square (RLS) algorithm was effective in identifying the parameters even though substantial noise was present due to the low end sensors utilised. The used algorithm was based on an implementation of the theoretical findings shown in [24].

Sensor faults for a smaller aircraft without sufficient sensor redundancies, were considered in [25]. The work was based on a model of a Piper aircraft under different conditions. A general setup was considered where measurements of the aircrafts control surface deflections, IMU data, and air data was available at high data rates. Residual signal for the diagnosis was created as polynomials. In [26] and [27] the polynomial method for residual generation was compared with a nonlinear geometric approach, an unknown input observer and artificial intelligence in form of neural networks. The polynomial method and nonlinear geometric approach was further developed in [31] to include estimates of the

sensor faults size.

In [14] fault tolerant control for a small UAV of the Aerosonde type [1] was investigated. The paper builds on previous results published in [11], [12], and [13] regarding stability and the aircrafts designed flight envelope. Faults on the control surfaces were considered for an aircraft that was not equipped with surface position sensors. The fault detection was achieved with unknown input decoupled functional observers. Because of the UAV's redundant actuators active diagnosis was used to isolate faults. The active isolation was done by exciting a combination of the control surfaces by a sinusoid and investigate if the redundancies were still present.

In [101] the flight envelope protection for commercial aircraft was investigated. Assessment of the flight envelope and how this can be used to design the aircraft controller, as well as FDI using a h_∞ based filter was considered. The filter was designed to accommodate aileron failures and fault detection time was within a few seconds.

The use of sliding mode control to achieve robustness against structural failures was presented in [121]. A cascade of two SMC's was used with the inner loop controlling the aircrafts rates based on set-points of Euler angles processed by the outer loop. However the presented method only handles partly loss of the aircrafts control surfaces and was not able to handle total control surface loss. Another use of SMC was seen in [81] and [82]. Here the SMC was used as a learning algorithm for an artificial neural network which controls a small UAV via nonlinear model inversion. The authors test degradation of the aircrafts handling possibilities but does not consider total loss of control surfaces. Atmospheric disturbances were also included. Also in [5] SMC has been used together with control allocation for flight control. The theoretical setup in [3] was implemented in the research flight simulator SIMONA. The implemented system relies on a methodology for identification and reconstruction of faults using sliding mode observers described in [46] and [123]. The Sliding mode based fault diagnosis has also been applied to the ADDSAFE benchmark problem. In [4] the authors solves both a sensor fault and an actuator runaway problem. Reconstruction of the fault signal was shown to work for both problems.

Due to the general non-linear behaviour of aircraft and models with learning capabilities are interesting, and therefore artificial neural networks have been proposed for FDI. In [97] sensor faults were isolated using neural networks and in [118] a validation scheme for UAV sensors were described. The longitudinal motion was considered and a pitch rate model based on a neural network which took a subset of longitudinal states was used. The residual made from a squared difference between the output model and the actual measurement was padded with a number of values equal to the minimum residual in the considered win-

dow. This way a better outlier rejection was achieved. In [119] the above methods were compared with the more common Extended Kalman filter approach where only parameters in a model with fixed structure description were estimated. The authors concluded that the learning based approach showed great potential for systems with poorly modelled dynamics, which is the case for small UAV's.

Other data based methods such as artificial immune systems ([37]) for fault detection has also been investigated with respect to aircrafts. In [95] results developed in [109] was used to infer a scheme where the aircrafts angular rates were combined with estimates of angular accelerations to generate parameters useful for the diagnosis. Data from an aircraft simulator were used to generate the data needed to identify features synonymous to fault-free behaviour. In [96] the artificial immune system were used to assess the impact different failures has on the aircrafts handling and by this predict reductions to the flight envelope in case of faults. The method has also been applied to failures of subcomponents of the aircraft such as engines in [110].

A model based approach to sensor faults were taken in [30]. Here the authors developed an adaptive diagnosis method for linear MIMO systems with uncertainties. The methodology were demonstrated on a model of an electro-hydrostatic actuator.

In [16] eigenstructure assignment was utilised to achieve a fault tolerant control of an aircraft. The authors find an optimal gain, offline, which was tolerant towards a class of control surface failures including surfaces stuck at random positions.

Diagnosis filters for aircrafts based on h_∞ optimisation methods were discussed in [68] and [90] amongst others. In [90] a h_∞ based FDI filter for the longitudinal motion of a passenger aircraft was investigated. Additive faults on both sensors (pitch rate channel) and actuators (elevators) were handled. The found filter is able to isolate faults both for input and output but the performance rely heavily on the tuning weights used in the optimisation. The application of [68] is errors in the thrusters of a small satellite. Two FDI filters based on h_∞ design was compared, and emphasise was put on the fact that even faults compensated by the satellites controller can be isolated, because the FDI were embedded within it.

In [136] partial loss of control surface action for general aircraft equipped with hydraulic driven surfaces were considered. The effectiveness of a failed controller was represented by a multiplicative fault model with a gain in the range between 0 and 1 to signify how much control action was accomplished under a given fault scenario. A fault tolerant control strategy, which applies a two step fault accommodation strategy, was suggested. First a passive accommodation which

was able to stabilise the aircraft when exposed to the fault that has not yet been diagnosed and then when the fault is sufficiently determined a new controller which utilises the aircrafts degraded performance optimally, was switched in. The actual fault diagnosis was not considered in the paper. The ADMIRE [49] aircraft model was used for verification of the method. In [135] the authors consider accommodation of control surface impairments with the faulty aircraft modelled as a polytopic linear parameter varying system. The proposed method was shown to perform better than a robust and reliable controller with no fault information.

The level of maturity and importance in the field is also seen by the industrial interest shown by for instance Airbus seen in [57], [58], [59], and [60]. The last describes the validation process involved with the European research project "Advanced Fault Diagnosis for Sustainable Flight Guidance and Control" (ADDSAFE).

1.4 Contributions

The main contribution in this work is that the derived methods have been based on the actual telemetry data available from an existing UAV platform. Since data from flights where faults occurred also were available it has been possible to try out the methods against actual incidents. Diagnosis of airspeed sensor faults was done using a new approach which utilises two airspeed estimates. One were made from ground speed measured by an onboard GPS receiver that was transformed into an airspeed estimate using wind information. Another estimate stems from a non-linear adaptive observer which estimate the engine's delivered thrust and from that make a second airspeed estimate. The method also included a feature to detect a return to normal operation which was shown to be able to reject false returns.

A control surface fault detection system using limited band-width telemetry data was also developed. Models of sufficient simplicity were derived and parameter estimation was combined with detection of change of the prediction error between measurements and the prediction made by a model using the parameters being adapted to.

Loss of GPS information for an UAV were also treated. A method using simplified model structures, with model parameters having a physical meaning was used to do parameter identification and state estimation for the complete aircraft. The model was obtained using a spherical simplex unscented filter. Position estimates was made available but the growth of the error made the suggested method less usable for practical purposes.

1.5 Structure and Outline of the Thesis

The remaining parts of this thesis consist of a summary containing an introduction to aircraft modelling, a brief description of the identification and change detection methods used. After this three fault cases which have been the center of investigation are described. Appendencies A to F contains papers in which the results obtained during the project have been disseminated. The summary aims to highlight the main approach to UAV fault diagnosis applied during the project as well as to give an introduction to the specific types of faults investigated.

Chapter 2

Aircraft description

This chapter gives a short introduction to modelling of fixed wing aircraft. This is mostly based on [122] and [80] that both gives a more elaborate description of all the major aspects of aircraft modelling and control. Furthermore a small section is added, that introduces the Banshee UAV [92] and its operating system. This is the specific UAV system that most of the diagnosis in this thesis is developed for.

2.1 Basic aircraft model

An aircraft is modelled by its dynamic and kinematic equations which describes its motion through the air. It is necessary to use a number of reference frames to describe the aircraft pose and movement seen from different perspectives.

2.1.1 Reference frames

A fixed wing aircraft is usually described by a body-axis system positioned in the aircrafts center of mass. The x-axis is pointing in the direction of the aircrafts nose, the y-axis out through the right wing and the z-axis down through the belly. These axes are fixed relative to the aircraft and therefore follow its motions. The axis are shown in Figure 2.1 and denoted $\{x_b, y_b, z_b\}$. The aerodynamic forces working on the aircraft are determined by the flow of wind over the body. This is determined in the wind reference frame denoted $\{x_w, y_w, z_w\}$. This system is rotated with respect to the body system by the aircrafts angle of attack, α, and sideslip, β. The aerodynamic lift force (F_L) works in parallel with z_w but with opposing direction. The drag (F_D) works in parallel with x_w also with opposing direction.

In between these two systems is the stability axes, which is offset from the body axis only by α (see Figure 2.1. This is denoted $\{x_s, y_s, z_s\}$ and is usually used

Figure 2.1: Body, stability and wind frames for the standard aircraft model.

when analysing steady-state flight control.

To navigate the aircraft it is necessary to have a coordinate system relating the aircrafts position to earth. To this avail a vehicle carried north-east-down (NED) system is used. The vehicle carried system has its origin in the aircraft's center of mass but is fixed to the earth, in the sense that the x-axis is always pointing north, the y-axis is pointing to the east and the z-axis is pointing towards the center of the earth. The aircraft's attitude is described by the Euler angles $\mathbf{\Phi}$. These are used to describe the rotation between the vehicle carried coordinate frame and the body frame of the aircraft and are denoted

$$\mathbf{\Phi} = \begin{bmatrix} \phi & \theta & \psi \end{bmatrix}^{\mathrm{T}} \tag{2.1}$$

It is customary to use the rotation sequence $\psi \rightarrow \theta \rightarrow \phi$ when dealing with aircrafts. To avoid the non-linearity in the Euler rotation sequence a quaternion [63] representation is sometimes used instead, especially when dealing with inertial measurement units.

2.1.2 Aircraft motion parameters

If we use the body reference frame as basis the aircraft's motion can be described by its velocities in the three axes.

$$\boldsymbol{v}_b = \begin{bmatrix} u & v & w \end{bmatrix}^{\mathrm{T}} \tag{2.2}$$

and the rotational motion around the body axes.

$$\boldsymbol{\omega} = \begin{bmatrix} p & q & r \end{bmatrix}^{\mathrm{T}} \tag{2.3}$$

The basic UAV instrumentation includes an IMU which measures both $\boldsymbol{\Phi}$ and $\boldsymbol{\omega}$. This is sufficient to create an attitude control system for the aircraft.

2.1.3 Kinematics

The kinematics of the aircraft relates the angular velocities $\boldsymbol{\omega}$ to the rate of change in the Euler angles $\dot{\boldsymbol{\Phi}}$, which are used in the rotation between body and earth coordinate systems. This is given by the following relations

$$\dot{\boldsymbol{\Phi}} = H(\boldsymbol{\Phi})\boldsymbol{\omega} \quad ; \quad H(\boldsymbol{\Phi}) = \begin{bmatrix} 1 & \tan\theta\sin\phi & \tan\theta\cos\phi \\ 0 & \cos\phi & -\sin\phi \\ 0 & \sin\phi/\cos\theta & \cos\phi/\cos\theta \end{bmatrix} \tag{2.4}$$

The change in position in the earth reference frame can be described by the rotating the translational velocities to the navigation frame.

$$\dot{\boldsymbol{p}_E} = C_{b2E}\boldsymbol{v}_b \tag{2.5}$$

where C_{b2E} is the rotation matrix from body to earth coordinates which is a function of $\boldsymbol{\Phi}$.

2.1.4 Dynamics

The airplane is seen as a rigid body moving through the air. Newton's 2. law must be satisfied all the time, which means we can relate the forces and moments acting on the rigid body to the velocities and accelerations. Since we are flying over at low speed and height over a relatively small area, we assume that the earth is flat and an inertial frame, such that we can neglect Coriolis forces.

Forces

The airplane is affected by a thrust force from the engine $\boldsymbol{F}_T$, an aerodynamic force $\boldsymbol{F}_A$ arising from the lift and drag from the airplane body, and naturally the gravitational force from the earth $\boldsymbol{F}_G$. With the mass m given this relationship is:

$$\frac{d}{dt}(m\boldsymbol{v}_b) = \sum \boldsymbol{F} = \boldsymbol{F}_T + \boldsymbol{F}_A + \boldsymbol{F}_G \tag{2.6}$$

Since this equation is expressed in the inertial frame (the earth system) we use the equation of Coriolis to take the derivative.

$$m\dot{\boldsymbol{v}}_b + \boldsymbol{\omega} \times m\boldsymbol{v}_b = \boldsymbol{F}_T + \boldsymbol{F}_A + \boldsymbol{F}_G \tag{2.7}$$

Moments

The aircraft is affected by two torques or moments: The aerodynamic moment $\boldsymbol{M}_A$ and the moment created by the engine $\boldsymbol{M}_T$. The aircrafts inertia is denoted $\boldsymbol{J}$.

$$\frac{d}{dt}\left(\boldsymbol{J}\boldsymbol{\omega}\right) = \sum \boldsymbol{M} = \boldsymbol{M}_T + \boldsymbol{M}_A \tag{2.8}$$

Taking the derivative:

$$\boldsymbol{J}\dot{\boldsymbol{\omega}} + \boldsymbol{\omega} \times \boldsymbol{J}\boldsymbol{\omega} = \boldsymbol{M}_T + \boldsymbol{M}_A \tag{2.9}$$

The engine is usually mounted almost in parallel with x_b such that it only creates a force in this direction and a torque around this axis. Since most UAV's are driven by propellers $\boldsymbol{F}_T$ and $\boldsymbol{M}_T$ depends on the propellers characteristics. In paper A and E a propeller model is used.

Dimensionless Coefficients

The aerodynamic forces and moments that are included in the above equations depend on a number of different parameters. It is customary to split them up according to their effect on the aircraft. This is done to have a common base between different aircraft's physical parameters such as wing characteristics and the dynamic pressure $q_{dyn} = \frac{1}{2}\varrho v_{rel}^2$, with ϱ being the air density and v_{rel} the relative velocity of the air over the aircraft fuselage. Since v_{rel} is directly given in the wind axes this reference frame is usually used in the segregation into dimensionless constants. The lift, drag and side force together with their corresponding moments are (following Stevens and Lewis [122]) given as

Drag force	$F_D = q_{dyn}SC_D$	Roll torque	$M_\phi = q_{dyn}SbC_\phi$
Side force	$F_C = q_{dyn}SC_C$	Pith torque	$M_\theta = q_{dyn}ScC_\theta$
Lift force	$F_L = q_{dyn}SC_L$	Yaw torque	$M_\psi = q_{dyn}SbC_\psi$

with b being the aircrafts wing span, c being the mean aerodynamic chord, S the wing area and C_j the non-dimensional coefficients.

2.2 Banshee Unmanned Aircraft System

The Banshee UAV is a part of a military weapons training system developed by Meggitt Defence Systems UK [93]. The system consists of the UAV itself and an operator unit placed on ground. The two parts are communicating via radio links. The uplink or command link sends reference velocity, height, heading and other commands to the aircraft. In return the ground station gets telemetry and other status data from the aircrafts avionic.

2.2.1 Banshee UAV

The Banshee UAV is a delta wing aircraft equipped with a small rear mounted gasoline engine. The thrust is delivered by a 2 bladed wooden propeller. It is launched from a catapult system and lands by parachute. It is therefore not equipped with any landing gear. The aircraft itself is a carbon fibre shell. With the standard engine it can achieve speeds up to 90 m/s but is usually flown around 65 m/s in order to save the fuel. The endurance is up to three hours on the 25 liters of fuel onboard. Depending on payload the aircraft can have a starting weight of up to 90 kg.

The drone has a relatively limited range of sensors onboard, but this is common for many lower cost UAV's. A three axes accelerometer and a three axes gyro coupled with a standard GPS receiver forms the attitude estimate for the aircraft. Apart from these pressure sensors to measure the airspeed and height has been fitted. The control surfaces are actuated by standard hobby servo motors, which means no position feedback is available.

The aircraft is controlled by a basic autopilot which keeps the attitude and follows the references set by the operator. The reference commands is sent from the ground station according to what the operator wishes done. The aircraft can be operated in a number of different modes depending on how much control is left to the autopilot, and it is possible, though difficult, to fly without any aid from the autopilot via a handheld remote control. However most flights are done in a fully controlled mode where height, heading and airspeed are sent according to a route chosen by the operator.

Even though the precise implementation of the autopilot is not known it has been inferred that it consist of a number of cascade coupled PID controllers for the lateral and longitudinal channels. These are similar to the descriptions in chapter 4 of [122]. The autopilot has been fine-tuned for the specific aircraft and works well as long as all sensors and actuators behave as expected. It has not been attempted to include the autopilot in the models used for fault diagnosis because of the limited information in the data-stream from the aircraft.

2.2.2 Diagnosis via telemetry data

In order to make a diagnosis system which does not intrude with the existing parts of the UAV the radio transmitted telemetry data is used as the single source of information. The only necessary information is then the telemetry protocol such that the relevant data can be extracted. In Figure 2.2 the suggested diagnosis setup is outlined. The fault detection is done online based on the measurements received from the aircraft and a model of the subsystem which should be diagnosed, for example a sensor or an actuator. In the figure a model

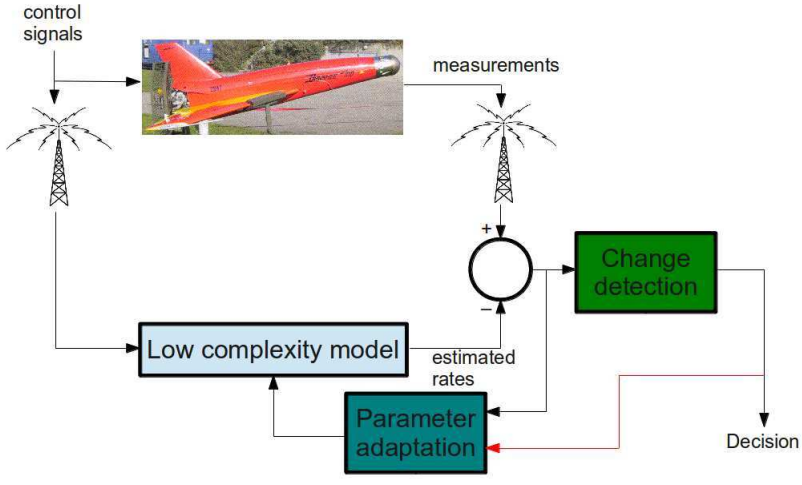

Figure 2.2: Sketch of the signal routes of a possible diagnosis setup based on the telemetry signals only.

of "low-complexity" is suggested. This has several benefits, but the main reason is related to the bandwidth of the telemetry channel.

The packages send from the Banshee to the ground station consist of 26 bytes where at most 16 bytes contains actual data values. The rest is header information and CRC checksum. These are in normal operating conditions send with a rate of approximately 12 Hz. Each package contains a specific message type signifying which values are included in the packages. Important messages like gyro information are send more often than messages about the current controller settings. But still this means that rate information is very sparse even though the rate gyro might sample with 50 Hz it is not send to the ground with remotely that rate. This makes it difficult to identify high-order models for an aircraft which can make roll motion of 20 to 25 deg/s.

This restriction in model data availability might make it impossible to diagnose some faults, but in practice it is shown that many of the common faults for the aircraft are visible in the telemetry data. So the purpose of this work is to find ways to automatically discover these signs of problems and present them to the operator.

As shown in Figure 2.2 adaptations of the chosen model based on differences between its output and the measurements are considered. Since aerodynamic models of the Banshee are not available and if they were they would probably be less useful due to the low sampled nature of the data, the system needs to learn model parameters while flying. Several methods for this have been explored as shown in the next chapter.

Chapter 3

Identification of model for diagnosis

When a component of a system fails the system behaviour will change from the nominal case. By measuring relevant signals on the system it is possible to observe this behaviour change and thereby infer that a fault has occurred. If the specific component that has failed should be identified it is necessary to have a good description of the system such that the faulty behaviour can be related to the component. This is the general idea of fault diagnosis, namely the ability to detect a fault and identify its root cause. In fault diagnosis socalled residuals, which contain fault information for the system, are usually employed. The difference between actual measured signals and those expected from the system description are one particular type of residuals that contain information of faults in the system, but in general, residuals need be generated from dynamic operations on input and output. Techniques for generating residuals are well known from the literature for both linear and nonlinear systems if the model parameters are known with reasonable precision. The literature is rich on this subject, since the seminal paper by [35], see e.g. the textbooks [104], [55], [32], [41]. If models are uncertain, parameter estimation [55] or adaptive filtering [61] could be employed.

In the previous chapter the complete aircraft model was given. This could be used for the task of design of diagnosis operators, but usually not all elements of this model are known for standard UAVs. Therefore an approach where model parameters are found online based on measurements has been pursued in this research. This task of identifying a suitable model for diagnosis is described in this chapter.

Model based diagnosis has been proven successful using a fixed plant model based on for example physical descriptions like ordinary differential equations.

Residual signals created from the difference between model output and actual plant measurements can then easily be used to detect changes in the plant behaviour. The drawback is that an almost perfect model of the plant is needed such that disturbances and noise is taken into account. For many systems like UAV's very complicated non-linear physics are involved when a complete description of behaviour is needed. Therefore diagnosis based on a fixed plant description is not feasible and methods where model parameters are estimated online are more attractive.

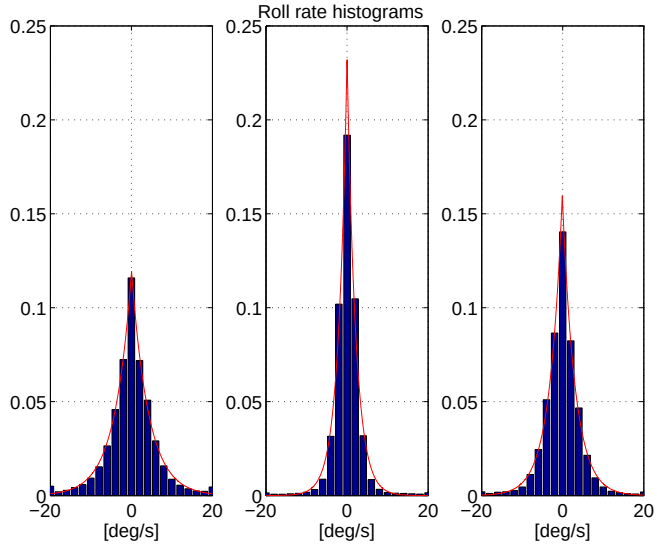

Figure 3.1: Histograms of the gyro roll rate for three different segments of fault free flying. The aircraft is flying wings-level straight ahead in all three cases.

Another reason for using an adaptive model is small discrepancies between different aircraft. For the Banshee UAV there is a not insignificant variation between sensor noise and biases from aircraft to aircraft. As an example of this histograms of roll rates from three different Banshee flights are shown in Figure 3.1. Each dataset is a segment of straight flight where no manoeuvring is done. Each dataset is fitted to a Laplacian distribution with the following density function:

$$f(x|\mu, b) = \frac{1}{2b} \exp\left(-\frac{|x-\mu|}{b}\right) \tag{3.1}$$

The parameters are shown in the table below.

Flight	μ	b
1	0.0427	4.192
2	0.0112	2.147
3	−0.1025	3.133

As can be seen both in the figure and from the table a large variation is shown in the data. All data is collected from healthy and fault free flights so the variation stems from the aircraft. This illustrates that adaptive models are needed.

3.1 Adaptive diagnosis model

This section gives a description of the different adaptive methodologies used for creating models for diagnosis purposes. Emphasis is put on their application to the diagnosis problem and not on derivation and proofs of their validity. In general low-order models are sought which have adequate information to describe the aircraft in its normal operating modes and in combination with statistical change detection reject the disturbances. The low-order models are chosen such that they contain identifiable parameters from the telemetry data.

3.1.1 Recursive Least Squares

Recursive least squares (RLS) filters employ a least squares method to minimise a cost index based on the error function between measurements and algorithm output. The algorithm is based on a general ARX (AutoRegressive models with eXternal signals) description of the following form

$$\begin{aligned} y[k] &= b_0 x[k] + b_1 x[k-1] + \cdots + b_{n_b} x[k-n_b] \\ &\quad -a_1 y[k-1] - \cdots - a_{n_a} y[k-n_a] \end{aligned} \tag{3.2}$$

where the parameters $a_{1\ldots n_a}$ and $b_{1\ldots n_b}$ should be estimated. Putting the inputs x and measurements y into a vector $\boldsymbol{\varphi}$ and the unknown parameters into $\boldsymbol{\Theta}$ the RLS algorithm can be summarised as follows

$$\varepsilon[k] = y[k] - \boldsymbol{\varphi}[k]^{\mathrm{T}} \hat{\boldsymbol{\Theta}}[k-1] \tag{3.3}$$

$$P[k] = \left(\lambda_f P[k-1]^{-1} + \boldsymbol{\varphi}[k]\boldsymbol{\varphi}[k]^{\mathrm{T}}\right)^{-1} \tag{3.4}$$

$$\hat{\boldsymbol{\Theta}}[k] = \hat{\boldsymbol{\Theta}}[k-1] + P[k]\boldsymbol{\varphi}[k]\varepsilon[k] \tag{3.5}$$

The forgetting factor λ_f scales the weight put on past estimates compared to the current measurement.

This algorithm was used in paper D and F for identifying low-order models between actuator input and rate responses of the aircraft, which are used to diagnose control surface faults. The recursive nature and relative fast convergence makes it well suitable for online estimation.

3.1.2 Spectral Analysis

Another approach to model identification is to transfer the data to the frequency domain. The transfer function $H_{yx}(s)$ between input x to output y, relates cross spectrum G_{yx} to power spectrum G_{xx} in the following manner

$$G_{yx}(s) = H_{yx}(s)G_{xx}(s) \Rightarrow \hat{H}_{yx}(s) = \frac{G_{yx}(s)}{G_{xx}(s)} \tag{3.6}$$

where $\hat{H}_{xy}(s)$ is the estimated transfer function.

In the practical implementation described in paper B this method shows to be very sensitive towards both noise and having enough excitation of the signal. By using a Coherence function

$$\gamma_{yx}^2(\varpi) = \frac{|G_{yx}(\varpi)|^2}{G_{xx}(\varpi)G_{yy}(\varpi)} \quad ; \quad \gamma_{yx}^2 \in [0;1] \tag{3.7}$$

it was shown to reject those data windows which do not contain useful information.

3.1.3 Kalman filters

Several variations to the standard Kalman filter can be used for estimating states in systems. It is customary to use a standard system description with state $\boldsymbol{x}$, input $\boldsymbol{u}$ and measurement $\boldsymbol{y}$ given by

$$\boldsymbol{x}_k = \boldsymbol{f}(\boldsymbol{x}_{k-1}, \boldsymbol{u}_{k-1}) + v_k \tag{3.8}$$

$$\boldsymbol{y}_k = \boldsymbol{g}(\boldsymbol{x}_k) + w_k \tag{3.9}$$

where the process noise is denoted v_k and the measurement noise is denoted w_k. These noise processes are assumed zero-mean and Gaussian distributed. When dealing with non-linear system functions $\boldsymbol{f}$ and $\boldsymbol{g}$ the Extended Kalman Filter (EKF) has become the de facto standard. With the EKF Taylor series are used to linearise the system around the working point. This means that derivatives of $\boldsymbol{f}$ and $\boldsymbol{g}$ should exist for the EKF to be applied to the problem.

The EKF was used in paper E to estimate wind parameters in a 2D plane. Since the non-linearity's of this problem is well behaved the estimation works well. In paper E the results of the estimation are shown.

When the systems non-linearities are significant or the derivatives of $\boldsymbol{f}$ and $\boldsymbol{g}$ are hard to obtain several other filters can be used. The Unscented Kalman Filter (UKF) [74] and the Divided Difference Filters (DDF) [100]. In paper D the Spherical Simplex Unscented Filter (SSUF) has been used to do a full estimation of states and parameters for the Banshee drone. The SSUF is an advanced

Kalman filter for non-linear systems based on the unscented transformation and using sigma points chosen by the spherical simplex method. This method was developed by Julier [75] and is better behaved numerically than the usual symmetric choice of points, employed in Unscented Kalman Filters (UKF). The SSUF method utilises that it is easier to estimate the probability distribution than the non-linear state propagation relationship itself. An unscented filter estimates the nonlinear mapping to the next state by propagating a number of sigma points $\mathcal{X}_k$ through the system. The sigma points are chosen to lie on a hypersphere around the mean using the method shown in [75]. As usually in Kalman filters the propagation procedure consists of two steps: A time update and a measurement update. To avoid taking the matrix square-root of the state covariance at each time update the square-root form of the UKF algorithm is used. The square-root unscented filter is described in details in [125].

The SSUF is used in paper C to estimate a reduced model of the Banshee UAV based on the telemetry data. The algorithm proves to work well in the sense that with the limited data available it is possible to get a sufficiently good aircraft model that can be used in case that vital sensors are lost. The algorithm also has benefits on the implementation side since the square root form used in the implementation has guaranteed numerical stability.

3.2 Adaptive filters used for diagnosis

The adaptive methods used during this project all have a general commonality. The estimated parameters are updated using a residual type signal made from the difference between system output and the estimated model output. In Figure 3.2 this pcinciple is illustrated on a block diagram. The model is fed the same input signal as the system and differences in output between the two are used to adjust the model to fit the system better. It makes sense also to use this signal for the fault diagnosis since it encompasses differences between model and system indicating a fault. A residual signal that does not lie within the noise deviation of zero indicates a fault. This can be detected using the change detection algorithms described in chapter 4.

If the adaption algorithm is tuned such that it quickly adapt to differences between system and model, the residual signal cannot be used for diagnosis. The periods where the signal is not close to the zero value will be too small to detect and the model will quickly adapt to any faults that occur in the system. On the other hand too little adaption will entail a model that does not fit the system correctly which could trigger false alarms in the change detector. The solution to this is to find a satisfactory middle ground between these two cases. Because of the large amount of data from real flights available for the Banshee UAV, including data with faults, it has been possible to empirically find a good adap-

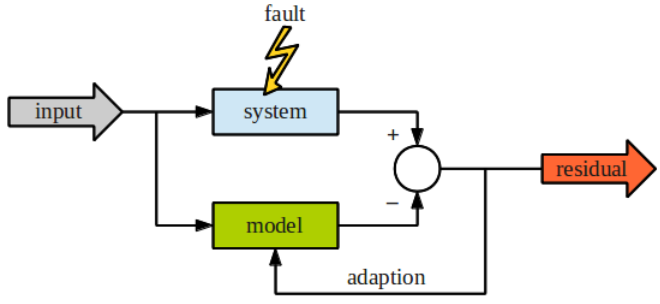

Figure 3.2: Residuals based on an adaptive model of the system.

tion gain for the adaption gains used on here. However simulations could also be used to find the correct gain. When an alarm is raised by the change detector the adaption algorithm is stopped and the model parameters are locked at their current values. This way adapting to the faulty model over time is avoided.

Another way of managing the adaption to a faulty model is to include change detectors on the adapted parameters. A sudden change in these also indicates that a fault has occurred in the system. This will in general have higher detection time than detections on the residual, but less sensitive towards noisy sensors.

Chapter 4

Change Detection

A main component in a fault detection scheme based on residual signals is the change detector, which should be able to distinct signals indicating a fault from "false positives" caused by noisy sensor values and unmodelled disturbances to the plant in question. By analysing the residual the change detector should raise an alarm when an indication of a fault is observed on the signals. This represents therefore the decision part of the diagnosis system. This chapter will outline the change detection methods used in this research.

4.1 Detecting abrupt changes based on statistical properties

The main methods for statistical change detection are described in the books by Basseville and Nikiforov [8] and Kay [77]. The methods are based on hypothesis testing of the signals in question, which in our case are the residual signals. Residuals are usually constructed to be close to zero in the nominal case, and deviate from zero only when a fault occurs in the plant. This produce the following two hypothesis that the residual signal x could belong to.

$$\mathcal{H}_0 \quad : \quad x[n] = w[n] \tag{4.1}$$

$$\mathcal{H}_0 \quad : \quad x[n] = f[n] + w[n] \tag{4.2}$$

where w is noise and f is a signal different from zero. To easier distinguish between the two hypothesis the change detection algorithm should take the actual statistical distribution of w for the signal into account.

The distribution of w can be determined in several ways. The Kolmogorov-Smirnov test can be used to decide whether a sample of data belongs to a known distribution. By substituting the parameters of the distribution by their maximum likelihood estimates (MLE) it is possible to test data against different types of distributions. This is done in paper D to reject the Gaussian distribution

for data. Graphical methods where data is plotted on statistical paper following known distributions can also be used to visually give an indication of the distribution.

To distinguish between the two hypotheses two methods are employed in this work. Starting with the CUSUM algorithm ([8]) which theoretically is applicable for detecting signal changes with known magnitude. If we denote the probability of a series of measurements $\boldsymbol{x}$, belongs to $\mathcal{H}_i$ by $P_i(\boldsymbol{x};\boldsymbol{\Theta})$ the CUSUM can be formulated as

$$S[k] = \sum_{j=1}^{k} \ln \frac{P_1(\boldsymbol{x};\boldsymbol{\Theta})}{P_0(\boldsymbol{x};\boldsymbol{\Theta})} \tag{4.3}$$

This sum of the log-likelihood ratios given known distributions and observations $\boldsymbol{x}[\boldsymbol{n}]$ exhibits negative drift when $\mathcal{H}_0$ is most likely and a positive drift when the alternative hypothesis $\mathcal{H}_1$ is the more likely of the two hypothesis. Therefore a direct comparison between a threshold values can be done to detect a change known magnitude. In reality the value of a change is not known, but an empirical value can be chosen based on previously seen fault developments.

Another method is the generalised likelihood ratio test (GLRT), which is derived from same likelihood ratio as the CUSUM.

$$L_G(\boldsymbol{x}) = \frac{P_1(\boldsymbol{x};\hat{\boldsymbol{\Theta}}_1)}{P_0(\boldsymbol{x};\hat{\boldsymbol{\Theta}}_0)} \tag{4.4}$$

where the distribution parameters $\boldsymbol{\Theta}$ are substituted with their MLEs. The GLRT does not have the recursive nature of the CUSUM, therefore a window of data is collected and processed at each sample.

4.2 Determine parameters for decision function

The threshold of the two change detectors must be found as a trade-off between false-alarm probability P_{FA} and the probability to detect P_D. For Gaussian distributions theoretical results relating these quantities to the threshold value exists. For the CUSUM the average run-length (ARL) function can be used in the analysis. An ARL function indicating the expected alarm time for the given distribution and change magnitude is used approximate values for P_D and P_{FA} given a wanted detection time value. In [8] the ARL is derived to the following expression

$$L(\mu_s) = \left(\exp\left(-2\left(\frac{\mu_s\gamma}{\sigma_s^2} + 1.166\frac{\mu_s}{\sigma_s}\right)\right) - 1 + 2\left(\frac{\mu_s\gamma}{\sigma_s^2} + 1.166\frac{\mu_s}{\sigma_s}\right)\right)\left(\frac{\sigma_s^2}{2\mu_s^2}\right) \tag{4.5}$$

with γ being the chosen threshold value. If we assume the signal has zero mean in the nominal case and the changes to the known mean h when the $\mathcal{H}_1$ is valid, the mean, μ_s, and variance, σ_s^2, of the CUSUM increments can be calculated by

$$\mu_s = \frac{h^2}{2\sigma^2} \qquad \text{and} \qquad \sigma_s = \frac{h^2}{\sigma^2} \tag{4.6}$$

for the case of $\mathcal{H}_1$. Thus $L()$ will give an estimate of the mean detection time $\hat{\bar{\tau}}$ with these parameters. For the case of $\mathcal{H}_0$ the values are:

$$\mu_s = -\frac{h^2}{2\sigma^2} \qquad \text{and} \qquad \sigma_s = \frac{h^2}{\sigma^2} \tag{4.7}$$

For these parameters $L()$ estimates the mean time between false alarms $\hat{\bar{T}}$. By choosing values for $\hat{\bar{\tau}}$ and $\hat{\bar{T}}$, that are appropriate for the analysed system, it is possible to calculate a value for the detector performance using these expressions.

For the GLRT asymptotic performance is given for the case where parameters of the signal distribution for the $\mathcal{H}_0$ hypothesis, denoted $\boldsymbol{\Theta}_0$, is known. It is shown in [77] that the asymptotic distributions for (4.4) are given by

$$2 \ln L_G(\boldsymbol{x}) \sim \begin{cases} \chi_r^2 & \text{under } \mathcal{H}_0 \\ \chi_r^2(\lambda) & \text{under } \mathcal{H}_1 \end{cases} \tag{4.8}$$

where the non-centrality parameter λ is a function of the distribution parameters and r is the number of parameters. A similar result does not exist for the general case where $\boldsymbol{\Theta}_0$ is unknown, however for some systems approximation of the $\mathcal{H}_0$ distribution is possible. In Figure 4.1 plots of P_{FA} and P_D are shown for a system following (4.8) for a number of different threshold parameters. The optimal choice of threshold can be found by maximising the probability for $P_D - P_{FA}$. This is indicated by the vertical line in the figure.

A different approach is shown in [52] and [48] where the actual distribution of the output of the GLRT or CUSUM is considered. This is done because output of the change detectors do not always follow the χ^2 distribution well, when the input is not close to being Gaussian distributed.

If we look at the GLRT and define the output of L_G to be distributed according to the function $F(\boldsymbol{x}; \boldsymbol{\Theta})$. For a series of data in the $\mathcal{H}_0$ case the right-tail probability connected to F indicates the probability that samples of F will go beyond a certain threshold. In Figure 4.2 an example is shown where output data of a GLRT is plotted on probability paper and fitted to a distribution. In this case the Weibull distribution is used because this is the one found for the residuals in both paper D and E. However in principle any distribution would

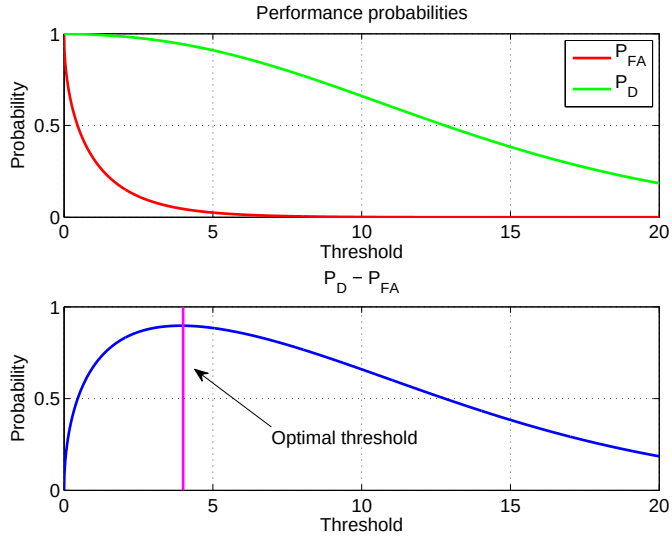

Figure 4.1: Illustration of detector performance and choice of threshold.

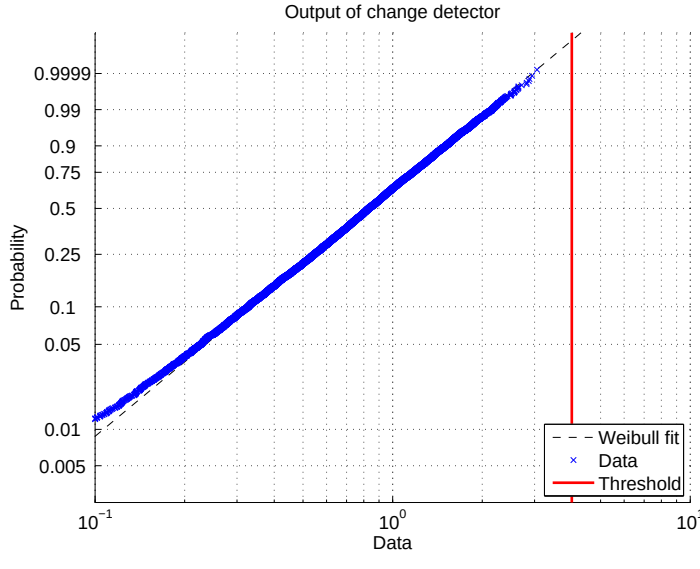

Figure 4.2: Probability plot of change detector output and corresponding threshold.

do. The threshold value is indicated on Figure 4.2 with the red vertical line corresponding to a probability of above 0.9999. Hence the right-tail probability will be below 0.0001 corresponding to a probability of having samples above the threshold in the $\mathcal{H}_0$ case. In paper E the exact calculation of the false alarm rate for a Weibull distributed GLRT output given a certain sample rate is shown.

Similar to the principle above data for the $\mathcal{H}_1$ case can analysed to find P_D given a certain choice of threshold. The right-tail distribution of the $\mathcal{H}_1$ data will tell the probability of data lying below and above the chosen threshold and thereby P_D. However there is a hurdle in doing this. Data from the $\mathcal{H}_0$ case is usually very easy to obtain as systems runs fault free most of the time. But data from $\mathcal{H}_1$ are harder to obtain. For system like UAV's critical faults usually causes an end of flight very quickly after the fault appears, which means that the amount of data available for the $\mathcal{H}_1$ case is very limited. This data might not be enough to make a sufficiently good match to a probability distribution. Another thing is that it might be hard to contain the data from the fault in one distribution since things like sensor saturations might change the properties of the data completely. An attempt to resolve the P_D value from data is made in paper E. Since the residual in this particular case crosses zero some time during fault development the data used has been cut before the end. It is found that 85% of the data lays above the threshold for the given choice of distribution. With the different uncertainties in determining the data for $\mathcal{H}_1$ and the general noise level of the data, this is quite satisfying.

Chapter 5

Summary of fault diagnosis cases

This chapter will cover the three main fault diagnosis cases investigated during the project. All these cases are derived from actual incidents with the UAV used by the Danish Navy. The three sections will cover the basic diagnosis setup used in each case as well as a summary of the main results obtained.

5.1 Pitot tube fault diagnosis

This section treats the incident that started this project. As stated in the introduction a faulty airspeed sensor in one of the Danish Navy's Banshee UAVs caused the aircraft to be lost during flight.

5.1.1 Aircraft airspeed measurement

In order to measure the airspeed aircraft usually employs a pitot static system. The system operates basically by measuring the pressure difference between two ports mounted on the body of the aircraft. One port is in the pitot tube, which is

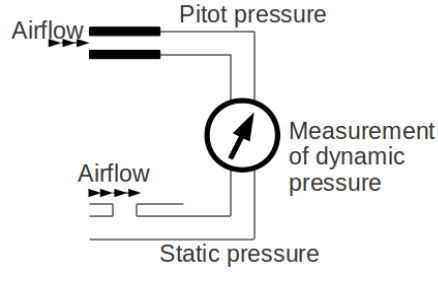

Figure 5.1: Schematic drawing of the airspeed measurement system.

pointing in the aircrafts direction of flight or the body x-axis. A pressure builds

up in the tube, P_{pitot}, as a result of the airflow that streams into the tube. The second port is measuring on the side of the UAV's fuselage and therefore measures the surrounding or static pressure P_{static}. Using Bernoulli's equation these measurements can be related to the dynamic pressure and thereby the airspeed can be found

$$P_{pitot} = P_{static} + \tfrac{1}{2}\varrho V^2 \Rightarrow V = \sqrt{\frac{2\left(P_{pitot} - P_{static}\right)}{\varrho}}, \tag{5.1}$$

with ϱ being the air density.
Sometimes pitot tubes are mounted on air-vanes that compensates for the aircrafts angle of attack or side slip, but on cheaper UAV's the tubes are fixed on the body so the measured stream is the forward body-fixed velocity. For most standard flight attitudes the imprecision resulting from this is neglectable.

5.1.2 Fault detection for pitot tube

The pitot static system is very sensitive towards clogging of the ports. Especially moist or dew on the aircraft that tends to freeze up as the aircraft reaches higher altitudes. This phenomenon called icing is especially a problem for the pressure ports. According to the final report of Bureau d'Enquêtes et d'Analyses pour la sécurité de l'aviation civile [29] investigating the accident of the Air France flight AF447 that was lost on June 1st 2009 on the route between Rio de Janeiro and Paris, the initiating event leading to the crash was inconsistent airspeed readings due to clogged pitot tubes. Clogged airspeed sensors has also been causing crashes with the Banshee.

Manned aircrafts usually employs heating elements in the tubes to cope with icing, but since clogging can happen due to several other reasons this is not always enough to completely avoid problems. Also on UAV's where both weight and power are limited the heating system might not be feasible. A software solution is therefore sought. In fault tolerant control systems airspeed sensor faults are usually treated as a part of the overall solution to recover from sensor faults. A specific treatment of faults on the airspeed sensor system is usually not employed, but only considered included in a robust or fault tolerant controller. However for existing UAV's with a fixed controller detection of airspeed sensor faults is very valuable.

Airspeed related to GPS information

With the limited sensor suite available on low cost UAV's, the only direct redundancy to the speed measurement is the GPS velocity. Standard GPS receivers gives a measure of the receivers current velocity based on a combination between averaging over the last position estimates from the Kalman filter and by

a measure of the Doppler shift in the carrier signals from the satellites. With the standard deviation $\sigma_{gps} \simeq 3$ m, this method gives the best results at higher speeds where the Doppler effect has most impact. For fixed wing UAV's this is advantageous since they are always moving with some velocity while flying, but for helicopters and similar vehicles, which can operate at zero velocity the GPS information is not precise enough for a usable speed reference. Since only fixed wing aircrafts are considered in this thesis the GPS velocity is useful.

The main issue encountered when using the GPS velocity is that it measures ground speed where the pitot-static system measures airspeed. In order to relate these two speed measurements in a way useable for fault diagnosis purposes it is necessary to infer the transformation between the two. This also means that using GPS solely when controlling the aircraft's speed can lead to stall situations. If the UAV is exposed to a strong tail wind the wings might not be able to produce sufficient lift to keep the aircraft flying at velocities that are adequate, seen from ground.

By estimating the wind velocity and direction the relation between ground speed and airspeed is obtained (as seen in Figure 2.1). A static wind field with an empirically determined height correction was used in paper A, which proved to work only for steady wind conditions was used in paper A. A more elaborate estimate based on the method first introduced by Cho et. al. in [33] was presented in paper E. Only 2D information containing wind speed and direction is necessary for the proposed diagnosis method so a full 3D wind velocity vector is not needed. The wind estimate is created from the vector sum relating the relative speed through air affecting the UAV, $\boldsymbol{v}_{rel}$, to the ground speed $\boldsymbol{v}_g$.

$$\boldsymbol{v}_g = \boldsymbol{v}_{rel} + \boldsymbol{v}_w \tag{5.2}$$

with the wind vector being $\boldsymbol{v}_w$. The size of the airspeed can then be formulated using the standard cosine rule for the triangle related to the vector sum.

$$v_{rel}^2 = v_w^2 + v_g^2 - 2v_g v_w \cos(\psi) = v_w^2 + v_g^2 - 2v_g v_w \cos(\psi_w - \psi_g) \tag{5.3}$$

where the angle ψ_w is the wind direction and the aircraft's course over ground is ψ_g. The triangle relation is illustrated in Figur 5.2.
In this equation two parameters needs to be estimated namely the two wind parameters v_w and ψ_w. By using an EKF as described in 3.1.3 these parameters are modelled as Gaussian random walk processes. A gain factor can be used to cope with the imprecision due to angle of attack and side slip if a body fixed pitot tube is used. This factor is also included in the EKF states. As shown in paper E this is able to estimate wind parameters sufficiently for diagnosis.

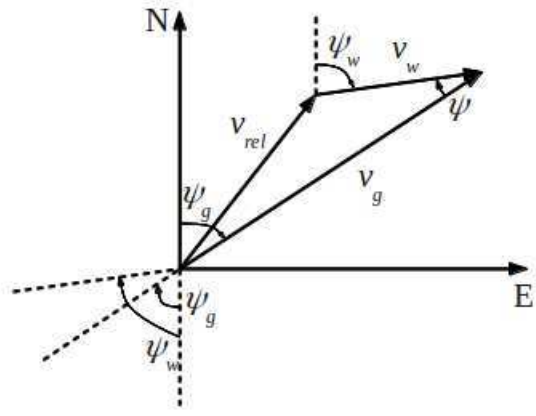

Figure 5.2: Triangle relating airspeed to speed over ground using the vector relation of (5.2). The compass north (N) and east (E) directions are also given.

Airspeed related to thrust

A less obvious redundancy to the airspeed is the thrust delivered by the UAVs engine. Throttle position or if available the engines rotational speed can be used to infer the thrust produced and combined with knowledge of the drag force this can be related to the aircraft relative velocity. For the Banshee UAV a measurement of engine speed is available but if this is not the case the rotational speed must be derived from the throttle position via an appropriate engine and load model.

The magnitude of the thrust force F_T delivered by the propeller can be derived from calculating dimensional lift and drag on it, and it is found that thrust is related to advance speed v and propeller angular speed n by the bi-linear expression

$$F_T = T_{nn}n^2 + T_{nv}nv \tag{5.4}$$

Here the thrust coefficients T_{nn} and T_{nv} relate to the propellers characteristics. This is further elaborated in papers A and E.
This thrust force is part of the force equilibrium for the aircraft described in section 2.1.4. Since both the engine and the pitot tube are mounted in the

aircrafts body x-axis, the force equation for this direction is used.

$$\begin{aligned} m\dot{u} &= m(rv - qw) + F_{Ax} - mg\sin(\theta) + F_T \\ &= m(rv - qw) + F_{Ax} - mg\sin(\theta) + T_{nn}n^2 + T_{nv}nu \end{aligned} \tag{5.5}$$

where F_{Ax} is the aerodynamic force for the x-direction. This mainly consists of drag when the aircraft is flying wings level and can therefore be approximated by an appropriate model for the drag. The following two models has been tested

$$F_{Ax} = \tfrac{1}{2}\varrho S u^2 \left(\Theta_{uu} + \Theta_{uu\alpha}\alpha\right) \tag{5.6}$$

and

$$F_{Ax} = \tfrac{1}{2}\varrho S u^2 \Theta_{uu}. \tag{5.7}$$

where Θ_{uu} and $\Theta_{uu\alpha}$ are parameters to be estimated. A dependency on the attack angle α as in (5.6) is founded in that drag is very depending on this. However since α is not measured on the Banshee, the estimate in (5.7) has been used instead. Because the aircraft fly most of the time in wings level condition the impact of not including α is not critical. The estimate of u is found using a high-gain observer which also estimates the parameters. The estimate of u can be used as a direct redundancy to the pitot tube measurement.

Residuals for diagnosis

If the airspeed measurement is denoted v_{pitot}, the GPS and wind based estimate of this value v_{gps} and the thrust based velocity estimate v_{thrust} a voting scheme based on these can be created. This is illustrated in the following table.

Residual	v_{pitot}	v_{gps}	v_{thrust}
R_1	1	1	0
R_2	1	0	1
R_3	0	1	1

When a 1 is shown in table the velocity estimate of that column is related to the residual of the given row. This means that the residual is sensitive to faults on that estimate. This means that if v_{pitot} starts to diverge from v_{gps} and v_{thrust} this will be visible in R_1 and R_2. However R_3 will indicate that v_{gps} and v_{thrust} agree and therefore strengthen the believe in their estimates. If multiple fault occur simultaneously it will not be possible to determine which value is correct using this scheme.

Fault Detection

In this section the detection scheme is tested against the fault described in the introduction. The detection approach has been described in paper A and E. The figures shown in this section are extracted from paper E. The recorded velocity

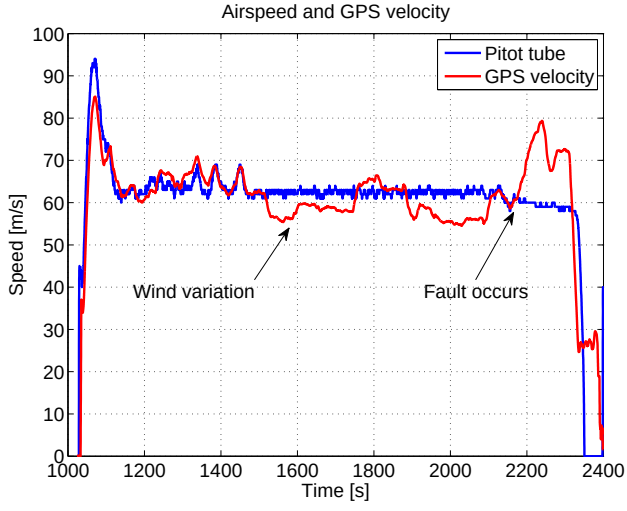

Figure 5.3: Airspeed and GPS velocity for incident involving a clogged airspeed sensor on a Banshee.

data from the Banshee lost due to pitot tube clogging is shown if Figure 5.3. Velocities measured by the pitot tube (airspeed) and the GPS (ground speed) are shown in the figure along with indications of different events. The small fluctuations in the GPS velocity is due to the aircraft changing heading and therefore experience different wind influence. Around $t = 2140$ s a high increase in GPS velocity is seen. This is where the pitot tube measurement fails. As the autopilot is unaware of this the velocity controller speeds up the aircraft. A manoeuvre done at this high velocity near $t = 2260$ s causes an actuator to fail and control of the aircraft is lost. In Figure 5.4 the aircraft roll angle and aileron deflection is shown for the last minutes of flight. It is seen that after $t = 2300$ s large aileron deflections are done without much response from the aircraft. The operator could have intervened and the aircraft saved had he been made aware that the pitot tube measurement was faulty and disabled the velocity controller.

The time development of the three residuals is shown in Figure 5.5 with an indication of the fault's starting point. As expected a large response is seen on R_1 and R_2 which both triggers an alarm by the corresponding change detector. A small variation is also observed in R_3. This is a consequence of the two airspeed estimators starting running open loop as the airspeed measurement is assessed as being faulty. This means that after a while the estimates will diverge. Another interesting observation from Figure 5.5 is that both R_1 and R_2 changes sign in the time period where the fault is present. If unhandled this behaviour will cause the change detector to lower the alarm for the period when the signal crosses

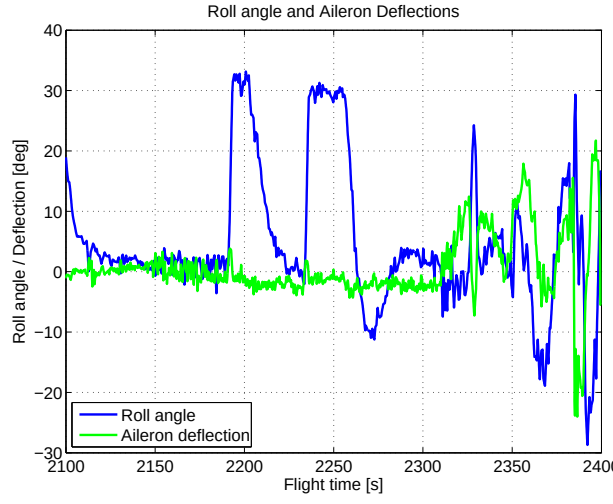

Figure 5.4: Roll angle and aileron deflection for the last minutes of Banshee with faulty pitot tube.

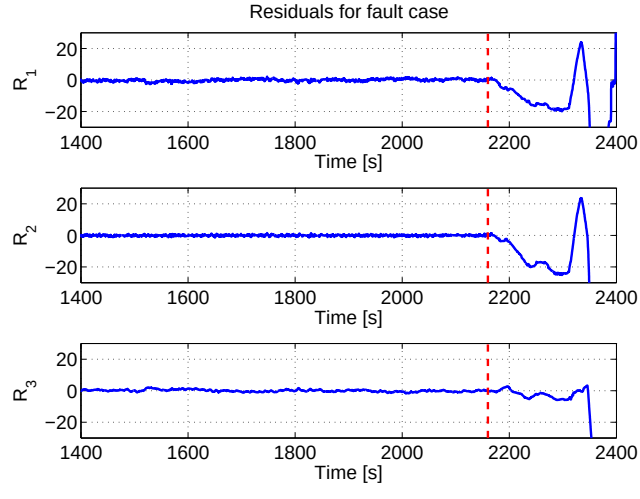

Figure 5.5: All three residuals development for the faulty flight data. The vertical dashed line indicates the beginning of the fault.

zero. This is not big problem since in most cases when an alarm is raised the UAV should be brought down to ground and inspected as quick as possible. But if the system where to be used automatically or the possibility of a fault

vanishing should be considered, this is not an optimal behaviour. Theoretically icing in the pitot tube could melt when the aircraft is brought down in lower altitudes and the flight could be continued. By looking at the residuals derivative over a small window of time it is possible to counteract the problem with the residual zero crossings. This is further ellaborated in paper E.

5.2 Handling of GPS loss

This section treats the case of loss of GPS signal for a small UAV, with the Banshee drone as basis.

5.2.1 GPS usage

The position of an UAV is usually determined by a GPS receiver onboard the vessel. With the normal position standard deviation of $\sigma_{gps} \simeq 3$ m a standard GPS sensor is more than adequate to determine UAV positions unless very tight manoeuvring, around buildings or similar, is needed. For the Banshee the GPS receiver is vital for operation even though the GPS is not directly involved in controlling the aircraft. Since the aircraft has a nominal velocity of over 200 km/h and a range of up to 100 km away from the base station there is no visual contact with the UAV as it fly. This means that the only way of knowing the position is by GPS. Furthermore the autopilot uses GPS information to follow the path specified by the operator and when GPS signal is lost this will not be possible.

Knowing an approximate aircraft position based on its manoeuvres from the loss of GPS is therefore very valuable. Even a very crude estimate may contribute to bring back the aircraft to base.

5.2.2 UAV position model

Compared to the previous mentioned pitot tube fault a loss of GPS does not require any detection. The sensor either gives positions or not. The difficult task here is to recreate the position information without the GPS. Using the aircraft model described in chapter 2 a dead-reckoning based on the last good GPS position is possible. If an exact model is known this will also lead to a good estimate. However if only a few easily measurable parameter such as the aircraft mass, inertias and wing dimensions are known, the task of calculating a position is much harder.

Based on the available telemetry data and using the generic model for an aircraft an estimate of its position is sought. In order to do this the complete state of the aircraft is estimated. This is given by the kinematics (2.4) and (2.5) and the

dynamics (2.7) and (2.9). For completion these are repeated here:

$$\dot{\boldsymbol{x}} = \begin{bmatrix} \dot{\boldsymbol{v}}_b \\ \dot{\boldsymbol{\omega}} \\ \dot{\boldsymbol{\Phi}} \\ \dot{\boldsymbol{p}}_E \end{bmatrix} = \begin{bmatrix} \frac{1}{m}(\boldsymbol{F}_T + \boldsymbol{F}_A + \boldsymbol{F}_G) - \boldsymbol{\omega} \times \boldsymbol{v}_b \\ \boldsymbol{J}^{-1}\left(\boldsymbol{M}_T + \boldsymbol{M}_A - \boldsymbol{\omega} \times \boldsymbol{J}\boldsymbol{w}\right) \\ H(\boldsymbol{\Phi})\boldsymbol{\omega} \\ C_{b2E}\boldsymbol{v}_b \end{bmatrix}. \tag{5.8}$$

The aerodynamic coefficients described at page 14 are reduced to the following simplified model:

$$\begin{aligned} C_D &= K_{D0} + K_{D\alpha}\alpha + K_{Dv}\left|\boldsymbol{v}_b\right| && (5.9)\\ C_C &= K_{C0} + K_{C\beta}\beta && (5.10)\\ C_L &= K_{L0} + K_{L\alpha}\alpha + K_{Lv}\left|\boldsymbol{v}_b\right| && (5.11)\\ C_\phi &= K_{\phi 0} + K_{L\delta_a}\delta_a + K_{\phi p}p + K_{\phi\beta}\beta && (5.12)\\ C_\theta &= K_{\theta 0} + K_{\theta\delta_e}\delta_e + K_{\theta q}q + K_{\theta\alpha}\alpha && (5.13)\\ C_\psi &= K_{\psi 0} + K_{\psi\beta}\beta + K_{\psi p}q\alpha && (5.14) \end{aligned}$$

where δ_a and δ_e are the aileron and elevator deflection respectively. The angular rates around the body x axis is p, the rate around the y axis is q and the body velocity is denoted $\boldsymbol{v}_b$. All the coefficients K need to be estimated as well as the states. The coefficients are modelled as constants affected by Gaussian noise.

Using the available output: Accelerometer data, gyro data, attitude estimates, airspeed and GPS position, it is possible to set up a filter to estimate the states. A Spherical Simplex Unscented Filter described in section 3.1.3 is used. When GPS data are lost these are removed from the measurement vector and the state estimates only relies on the remaining sensors.

In paper C this approach is described in more detail. Figure 5.6 shows the data from a flight where a GPS loss is simulated. From the GPS signal is lost to the aircraft has returned to its starting position, the aircraft has flown over 6 km and its position error is about 600 m. This might suffice to spot the aircraft visually on a clear day in order to bring it down safely, but for any practical use this is not precise enough. One could do a change of the returning pattern as soon as the error occurs. The error on the heading estimate is small which means that if the aircraft is directed towards the base immediately after the GPS dropout it will pass within visual range.

5.3 Control surface fault diagnosis

One of the most critical faults that can happen to an aircraft is partly or totally loss of one of the control surfaces. This reduces manoeuvrability of the aircraft significantly and will in many cases lead to a crash even with an experienced

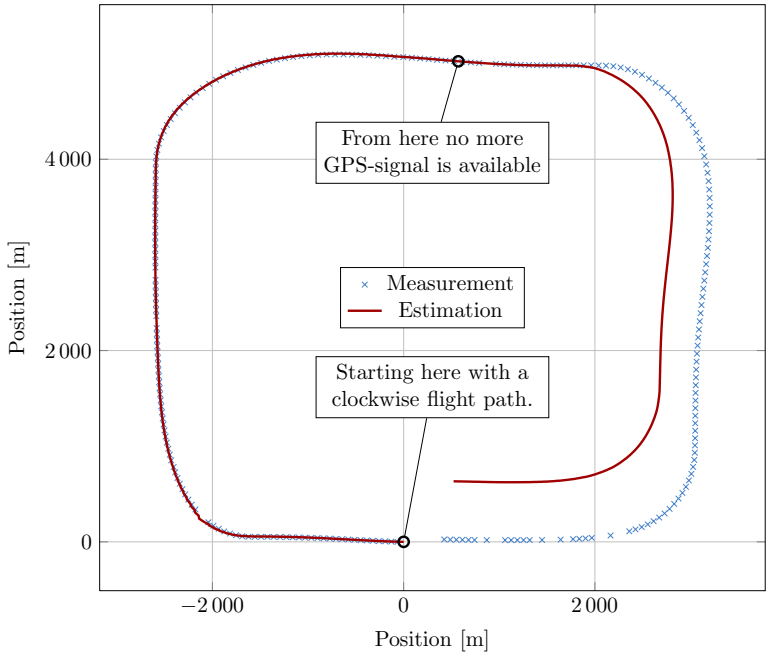

Figure 5.6: Estimation of the aircraft position after a loss GPS reception.

pilot flying. If a non-robust autopilot is used on a UAV which suddenly loses manoeuvrability partly, it will most likely result in a crash for similar reasons. For the Banshee drone only a few things can be done to save the aircraft in a case of control surface loss if the onboard avionic should not be modified. In most cases shutting of the engine and deploying the parachute will be the only way to safely get the drone down to ground. In these situations every second sooner the AVO reacts will heighten the chance of saving the aircraft, therefore fast detection is critical.
This section will present an overview of the approach taken for detecting control surface faults for the Banshee and also how this method perform on the simulated UAV described in paper F. Autonmous robustness and fault tolerance could be achieved by the means treated in paper F, but this require full control over the avionic software.

5.3.1 Control Surfaces

The control surfaces of the Banshee are mounted side by side on the trailing edge of the delta wing as seen in Figure 5.7. The ailerons are the outermost pair of flaps and operate in opposite directions to each other. The elevators are mounted closest to the aircraft body and are in charge of creating pitch moment.

Figure 5.7: The control surfaces of on the wing of the Banshee drone.

The left and right aileron do not operate independently of each other. This also applies to the left and right elevator.

The surfaces are operated via a metal linkage, which is hidden under the small lid in the wing. Servo motors, which are mounted inside the wing provide the actuation. When the aircraft is exposed to wind gusts, or if the hinges have become worn flaps have been lost completely. Several cases have shown that the flaps rips off in their mounting points or the linkage point is torn off.

Another related fault is that the servo skips a tooth in the gear linking the motors rotor shaft to the linkage arm. This is usually not critical although this could potentially cause an actuator to saturate and thereby create less actuation to one side. Therefore, this case would also need to be diagnosed.

5.3.2 Surface fault detection

Aerodynamic forces and torques are created by the aircraft's wings, body and control surfaces and are usually modelled by a set of non-dimensional coefficients relating each force and moment to a complex dependency on aircraft attitude and control surface deflection. This corresponds to the equations given on page 14, which relate the non-dimensional coefficients to actual forces and torques. To get a complete description of the non-dimensional coefficients involved, wind-tunnel experiments or fluid dynamic simulations of the aircraft wings and body must be carried out. Obtaining such a model is time consuming and it will not be fully utilised in this application, because of the limited dynamics visible on the telemetry data from the UAV. Instead a low complexity model is derived based on the information available in the telemetry data.

Low Complexity Actuation Model

A set of transfer function can be defined between the control input of the surfaces and the aircraft reaction. Since almost all UAVs have gyros measuring the turn rates around the three body axes (defined in Figure 2.1 on page 12) using

these are generic. In Figure 5.8 the equations are shown for the available controls of the Banshee. The division in a lateral and longitudinal channel seen in

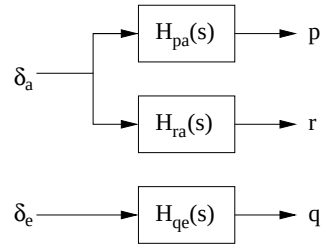

Figure 5.8: Transfer functions between the aircraft actuators and rates.

Figure 5.8 is very often done when control systems for aircraft are designed [122].

The transfer functions can be obtained in several ways. When low-rate telemetry data is used as the only source of information it is only possible to obtain an approximate linear relationship between the inputs and rates. Therefore, a set of time-domain relations can be used with success. This ends up with the following three relations for roll, pitch and yaw calculated at sample k.

$$p[k] = a_{pa}\delta_a[k] + b_{pa} \quad (5.15)$$

$$q[k] = a_{qe}\delta_e[k] + b_{qe} \quad (5.16)$$

$$r[k] = a_{ra}\delta_a[k] + b_{ra}r[k-1] + c_{ra} \quad (5.17)$$

where b_{pa}, b_{qe} and c_{ra} are bias terms and a_{pa}, a_{qe} and a_{ra} are gain factors. Equation 5.17 includes the integrating effect between the aileron and yaw rate in the b_{ra} term. Using the RLS algorithm described in 3.1.1 these parameters can be estimated using the ARX model structure. The residual signals used for the diagnosis is directly obtained from the residuals used in the RLS algorithm.

Fault signature

Several types of effects from control surface faults are usually considered in the literature [47]. These include surfaces stuck in one position, slower reacting actuators, surfaces flapping in the wind stream over the wing and several other fault types. In order to be able to distinguish between these different cases relative precise sensor values are needed, in particular feedback of the control surfaces position would be valuable for analysis of faults affecting the actuator dynamics. With the low-sampled data available from the telemetry used in the approach pursued in this thesis, this is not easy. Therefore only faults which have a stepwise effect on the aircraft are considered. Faults like complete loss of a control surface or slip of the servo link will have such an effect, and these are also the typical faults seen in practise.

Results Obtained

The loss of actuators fault is investigated in papers C, D and F, using the above mentioned low-complexity model approach. In paper C frequency domain functions corresponding to those shown in Figure 5.8 are found by spectral methods. By also estimating the spectral coherence of the involved signals it was possible to reject data without relevant information. A dataset from the Banshee, where a servo-slip occurs just at takeoff, is used as verification of the approach. The main disadvantage of this approach it its relatively intensive computational-wise especially in the spectral estimation of the transfer functions.

In paper D time-domain equations (5.15), (5.16) and (5.17) has been used as model instead. This reduces the cost in computing the residuals significantly since RLS is used. Since this reduced order model does not cover the complete system behaviour the residuals of the RLS are correlated time wise. As a consequence a whitening process was applied such that the signals were made suitable for the change detection.

In paper F the RLS based approach has been modified to be used as the basis for fault detection in a fault tolerant control system. The UAV described in paper F has independent actuation of all its control surfaces. This means that in order to diagnose a fault it is necessary to add a system that can isolate which control surface is faulty. An active diagnosis approach has been used to achieve this. When a fault is detected a test signal is applied to each of the control surfaces individually and the aircraft reaction is monitored. If a surface does not force the anticipated reaction it is considered faulty. The diagnosis result is used to reconfigure the controller of the aircraft and the faulty device is omitted from the control action. This entails more actuation of the remaining surfaces and could lead to saturation of the surfaces. Anti-windup was implemented in the controllers to prevent negative effects of this in most cases.

Chapter 6

Conclusion and Perspectives

6.1 Conclusion

In this thesis fault diagnosis possibilities for small unmanned aerial vehicles was investigated. The focus has been on developing methods that use the available instrumentation and do not require adding sensors, which reduces the aircraft endurance. Mathematical redundancies have been utilised instead of hardware redundancies. Diagnosis methods are developed with the intend of using them for a specific aircraft, namely the Banshee drone, but since only a small amount of aircraft specific modelling is used, there should be no hindrance in applying the results to a different UAV.

Three common fault scenarios has been identified and treated based on flight experiences with the Banshee drone. In all three cases the objective have been to create a reliable system for diagnosing the fault, which could be used by either an UAV operator or as input to a fault tolerant autopilot.

Fault detection for the pitot tube, which measure the vehicles airspeed was one of the faults considered and the detection of this type of fault was one of the main contributions of this research. A fault diagnosis setup was suggested, which utilises velocity estimations from engine thrust and GPS velocity. Two dimensional wind field estimation was used to convert the ground speed measured by the GPS to the airspeed to create a redundancy. This was combined with a non-linear observer estimating aircraft velocity based on an engine and thrust model. From these estimates three residual signals were created and collected in a voting scheme such that isolation of the fault was achieved. Changes in the residual signals indicating faults were done using hypothesis tests based on Generalised Likelihood Ratio testing. In papers A and E these methods was treated and a combination of use of data from prior flights with online estimation made it possible to obtain detection with the specified false alarm probability. In pa-

per E detection of changes from fault to normal was considered by employing a statistical test of a residual containing both amplitude and rate of change information. This was shown to reject false revert to normal hypotheses in real events.

A scheme for detecting faults for aircraft which has lost control surface action has also been suggested. This scheme utilises that the control surfaces have direct influence on the body angular rates. A number of low-order models of this effect were suggested. These models where all adaptive and did not require detailed information about the aircraft aerodynamic parameters. Using the models to create residual signals and by designing change detectors for these it was possible to detect control surface faults. The combination of statistical change detection with the parameter adaptive models showed to be successful and it was possible to advise the operator about sudden occurrences of faults for scenarios with real incidents. The diagnosis scheme was treated in papers B, D and F. In paper B model estimation was done using spectral analysis and it was shown how to distinguish time-slots with useful information from noisy measurements. An estimation method that requires less computational power was used in papers D and F. Furthermore in paper F the methods were used as the diagnosis part of a robust and fault tolerant autopilot. It was shown that the method were able to do timely diagnose such that reconfiguration of the autopilot could be initiated and an aircraft that would otherwise have crashed was able to continue flying.

Loss of position information has also been treated. When flying UAV's GPS positions are very critical for safe mission execution. The detection of GPS dropout has not been treated since this usually is easy to determine. Instead a backup solution for position information was investigated. By estimating the aircraft states and a number of relevant aerodynamic parameters using a Spherical Simplex Unscented Filter the position information could be made available when needed. Unfortunately did the position error grow rapidly over time which made the suggested method unusable for practical purposes. The solution was presented in paper C.

6.2 Perspectives

Fault diagnosis systems for UAVs have, in general, a great potential and they are a vital part of the necessary components that UAVs should have, to increase their reliability in operation. The different diagnosis algorithms described in this thesis all has good performance both in simulation and when tested using real life recordings. However a number of improvements could be done to further enhance their value.

For the diagnosis system that should be used with the Banshee UAV and Meg-

gitt's UAS the logic next step would be to see how these work in real operations where the UAV operator gets information from the diagnosis system while he is flying. While the algorithms detection times are sufficient for accommodating faults in theory, it might not be so in practice because several outside factors play in.
Another different path to take would be integrating the algorithms in the aircraft avionic. This would eliminate many of the difficulties because of low-sampled data and approaches to this path has already been made in the work of paper F.

The airspeed fault detection scheme assumes that the UAV is powered by a propeller based engine. Recent developments within small jet turbines has made those available for UAVs and therefore enhancing the detection scheme for a jet powered aircraft would be a interesting step. Another interesting part of this system is the return to normal detection. Further enhancements could be made to this by using a vector based residual.

Several of the described diagnosis algorithms assume that the aircraft is fault-free when they are initiated. By incorporating past knowledge of similar aircraft parameters it should be possible to detect if faults are present from the second the algorithms are started. Initial values has been used with the surface fault detector with success, but for the pitot tube diagnosis system using atmospheric data might also be necessary to achieve good results.

Bibliography

[1] Aerosonde Pty Ltd., 2010. URL `http://www.aerosonde.com/`.

[2] E. Alcorta-Garcia, A. Zolghadri, and P. Goupil. A nonlinear observer-based strategy for aircraft oscillatory failure detection: A380 case study. *IEEE Transactions on Aerospace And Electronic Systems*, 47 (4):2792–2806, 2011.

[3] H. Alwi and C. Edwards. Sliding mode ftc with on-line control allocation. In *45th IEEE Conference on Decision and Control, IEEE Publications*. IEEE, 2006.

[4] H. Alwi and C. Edwards. Second order sliding mode observers for the addsafe benchmark problem. In *8th IFAC Symposium on Fault Detection, Supervision and Safety of Technical Processes*, 2012.

[5] H. Alwi, C. Edwards, O. Stroosma, and J. A. Mulder. Fault tolerant sliding mode control design with piloted simulator evaluation. *AIAA Journal of Guidance, Control, and Dynamics*, 31(5):1186–1201, 2008.

[6] B. Anderson, S. Dasgupta, P. Khargonekar, F. J. Kraus, and M. Mansour. Robust strict positive realness: Characterization and construction. *IEEE transaction on Circuits and Systems*, 37:869–875, 1990.

[7] N. Balakrishnan and M. Kateri. On the maximum likelihood estimation of parameters of weibull distribution based on complete and censored data. *Statistics and Probability Letters*, 78:2971–2975, 2008.

[8] M. Basseville and I. V. Nikiforov. *Detection of Abrupt Changes: Theory and Application*. Information and System Science. Prentice Hall, New York, 1993.

[9] M. Basseville. Detecting changes in signals and systems - a survey. *Automatica*, 24(3):309–326, 1988.

[10] A. Bateman, D. Ward, J. Monaco, and Z. Lin. Stability analysis for reconfigurable systemn with actuator saturation. In *Proc. American Control Conference, Anchorage, AK*, pages 4783–4788, 2002.

[11] F. Bateman, H. Noura, and M. Ouladsine. Actuators fault diagnosis and tolerant control for an unmanned aerial vehicle. In *16th IEEE International Conference on Control Applications*, 2007.

[12] F. Bateman, H. Noura, and M. Ouladsine. A fault tolerant control strategy for an unmanned aerial vehicle based on a sequential quadratic programming algorithm. In *Proceedings of the 47th IEEE Conference on Decision and Control*, 2008.

[13] F. Bateman, H. Noura, and M. Ouladsine. Active fault detection and isolation strategy for an unmanned aerial vehicle with redundant flight control surfaces. In *16th Mediterranean Conference on Control and Automation*, 2008.

[14] F. Bateman, H. Noura, and M. Ouladsine. Fault diagnosis and fault-tolerant control strategy for the aerosonde uav. *IEEE Transactions on Aerospace and Electronic Systems*, 47(3):2119–2137, 2011.

[15] F. Bateman, H. Noura, and M. Ouladsine. Fault tolerant control strategy based on the doa: Application to uav. In *7th IFAC Symposium on Fault Detection Supervision and Safety of Technical Processes*, 2009.

[16] A. I. Belkharraz and K. Sobel. Fault tolerant flight control for a class of control surface failures. In *American Control Conference. Proceedings of the 2000*, volume 6, pages 4209–4213, 2000.

[17] M. Benini, M. Bonfè, P. Castaldi, W. Geri, and S. Simani. Design and analysis of robust fault diagnosis schemes for a simulated aircraft model. *Journal of Control Science and Engineering*, 2008:7:1–7:18, 2008.

[18] D. Bernstein and A. Michel. A chronological bibliography on saturating actuators. *International Journal of Robust and Nonlinear Control*, 5(5): 375–380, 1995. doi: 10.1002/rnc.4590050502.

[19] M. Blanke, M. Kinnaert, J. Lunze, and M. Staroswieki. *Diagnosis and fault tolerant control*. Springer, second edition, 2006.

[20] M. Blanke. *Ship propulsion Losses Related To Automatic Steering And Prime Mover Control*. PhD thesis, Technical University of Denmark, 1981.

[21] M. Blanke and M. Staroswiecki. Structural design of systems with safe behavior under single and multiple faults. In *6th IFAC Symposium on Fault Detection, Supervision and Safety of Technical Processes SAFEPROCESS*, pages 511–516, Beijing, P. R. China, September 2006.

[22] M. Blanke, R. Izadi-Zamanabadi, and T. Lootsma. Fault monitoring and re-configurable control for a ship propulsion plant. *Journal of Adaptive Control and Signal Processing*, 12:671–688, 1998.

[23] M. Bodson. Evaluation of optimisation methods for control allocation. *Journal of Guidance, Control and Dynamics*, 25 (4)(4):703–711, July 2002.

[24] M. Bodson. A reconfigurable nonlinear autopilot. *Journal of Guidance, Control, and Dynamics*, 26(5):719–727, 2003.

[25] M. Bonfè, P. Castaldi, W. Geri, and S. Simani. Fault detection and isolation for on-board sensors of a general aviation aircraft. *International Journal of Adaptive Control and Signal Processing*, 20:381–408, 2006.

[26] M. Bonfè, P. Castaldi, W. Geri, and S. Simani. Design and performance evaluation of residual generators for the fdi of an aircraft. *International Journal of Automation and Computing*, 4(2):156–163, 2007.

[27] M. Bonfè, P. Castaldi, W. Geri, and S. Simani. Nonlinear actuator fault detection and isolation for a general aviation aircraft. *Space Engineering, Telecommunication, System Engineering and Control*, 27:107–113, 2007. Special Issue on Automatic Control in Aerospace.

[28] R. G. Brown and P. Y. C. Hwang. *Introduction to Random Signals and Applied Kalman Filtering.* John Wiley & Sons, 1997.

[29] Bureau d'Enquêtes et d'Analyses pour la sécurité de l'aviation civile. Final Report On the accident on 1st June 2009 to the Airbus A330-203 registered F-GzCP operated by Air France flight AF 447 Rio de Janeiro - Paris. Technical report, Ministère de l'Écologie, du Développement durable, des Tarnsports et du Logement, 2012. URL `http://www.bea.aero/docspa/2009/f-cp090601.en/pdf/f-cp090601.en.pdf`.

[30] J. O. Burkholder and G. Tao. Adaptive detection of sensor uncertainties and failures. *AIAA Journal of Guidance, Control, and Dynamics*, 34(6): 1605–1612, 2011.

[31] P. Castaldi, W. Geri, M. Bonfè, S. Simani, and M. Benini. Design of residual generators and adaptive filters for the fdi of aircraft model sensors. *Control Engineering Pratice*, 2009.

[32] J. Chen and R. J. Patton. *Robust Model-based Fault Diagnosis for Dynamic Systems.* Kluwer Academic Publishers, 1999.

[33] A. Cho, J. Kim, S. Lee, and C. Kee. Wind estimation and airspeed calibration using a uav with a single-atenna gps receiver and pitot tube. *IEEE Transactions on Aerospace and Electronic Systems*, 47:109–117, 2011.

[34] Y. M. Cho and R. Rajamani. A systematic approach to adaptive observer synthesis for nonlinear systems. *IEEE Transactions on Automatic Control*, 42(4):534–537, April 1997.

[35] E. Y. Chow and A. S. Willsky. Analytical redundancy and the design of robust failure detection systems. *IEEE Transactions on Automatic Control*, AC-29(7):603–614, 1984.

[36] G. Chowdhary and R. Jategaonkar. Aerodynamic parameter estimation from flight data applying extended and unscented Kalman filter. *Aerospace Science and Technology*, 14(2):106–117, 2010.

[37] D. Dasgupta, editor. *Artificial Immune Systems and Their Applications*. Springer, 1999.

[38] S. Dasgupta and A. Bhagwat. Conditions for designing strictly positive real transfert functions for adaptive output error identification. *IEEE Trans, Circuits Syst.*, CAS-34:731–737, 1987.

[39] C. De Persis and A. Isidori. A geometric approach to nonlinear fault detection and isolation. *IEEE Transactions on Automatic Control*, 46(6): 853–865, 2001.

[40] C. De Persis, R. De Santis, and A. Isidori. Nonlinear actuator fault detection and isolation for a vtol aircraft. In *Proceedings of the American Control Conference*, 2001.

[41] S. X. Ding. *Model-based Fault Diagnosis Techniques - Design Schemes, Algorithms, and Tools*. Springer, 2008.

[42] J. Dong, M. Verhaegen, and F. Gustafsson. Robust fault detection with statistical uncertainty in identified parameters . *IEEE Transactions on Signal Processing*, 60 (10):5064–5072, 2012. doi: 10.1109/TSP.2012.2208638.

[43] G. Ducard and H. P. Geering. Efficient nonlinear actuator fault detection and isolation system for low-cost uavs. *AIAA Journal of Guidance, Control, and Dynamics*, 31(1):225–237, January 2008.

[44] G. J. J. Ducard. *Fault-tolerant Flight Control and Guidance Systems*. Springer Verlag, 2009.

[45] W. Durham. Constrained control allocation. *Journal of Guidance, Control, and Dynamics*, 16(4):717–725, July 1993.

[46] C. Edwards, S. S. K., and R. J. Patton. Sliding mode observers for fault detection. *Automatica*, 36:541–553, 2000.

[47] C. Edwards, T. J. J. Lombaerts, and M. H. Smaili, editors. *Fault Tolerant Flight Control: A Benchmark Challenge*. Springer, 2010.

[48] S. Fang, M. Blanke, and B. J. Leira. Mooring system diagnosis and structural reliability control for position moored vessels. *Control engineering Practice*, 2012.

[49] L. Forsell and U. Nilsson. Admire the aero-data model in a research environment version 4.0, model description. Technical report, Totalforsvarets forskningsinstitut, 2005.

[50] M. L. Fravolini, V. Brunori, G. Campa, M. R. Napolitano, and M. La Cava. Structured analysis approach for the generation of structured residuals for aircraft fdi. *IEEE Transactions on Aerospace and Electronic Systems*, 45 (4):1466–1482, 2009.

[51] A. Freddi, S. Longhi, and A. Monteriu. A model-based fault diagnosis system for unmanned aerial vehicles. In *7th IFAC Symposium on Fault Detection, Supervision and Safety of Technical Processes*, 2009.

[52] R. Galeazzi, M. Blanke, and N. K. Poulsen. Early detection of parametric roll resonance on container ships. *IEEE Transactions on Control Systems Technology*, 2012. doi: 10.1109/TCST.2012.2189399.

[53] E. R. Gelso and M. Blanke. Structural analysis extended with active fault isolation -methods and algorithms. In *Proc. 7th IFAC Symposium on Fault Detection, Supervision and Safety of Technical Processes, SAFEPROCESS'2009*, pages 597–602, 2009. doi: 10.3182/20090630-4-ES-2003.0009.

[54] J. J. Gertler. Fault detection and isolation using parity relations. *Control Engineering Practice*, 5(5):653–661, 1997.

[55] J. Gertler. *Fault detection and diagnosis in engineering systems*. Marcel Dekker, 1998.

[56] G. Goodwin, S. Graebe, and M. Salgado. *Control System Design*. Prentice-Hall Inc., New Jersey, 2001.

[57] P. Goupil. Airbus state of the art and practices on fdi and ftc. In *7th IFAC Symposium on Fault Detection, Supervision and Safety of Technical Processes*, 2009.

[58] P. Goupil. Oscillatory failure case detection in the a380 electrical flight control system by analytical redundancy. *Control Engineering Practice*, 18(9):1110–1119, 2010.

[59] P. Goupil. Airbus state of the art and practices on fdi and ftc in flight control system. *Control Engineering Practice*, 19(6):524–539, 2011.

[60] P. Goupil and A. Marcos. Industrial benchmarking and evaluation of addsafe fdd designs. In *8th IFAC Symposium on Fault Detection, Supervision and Safety of Technical Processes*, 2012.

[61] F. Gustafsson. *Adaptive Filtering and Change Detection.* John Wiley & Sons, Ltd, 2000.

[62] F. Gustafsson and J. Palmqvist. Change detection design for low false alarm rates. In *IFAC International Symposium on Fault Detetction, Supervision and Safety for Technical Processes (SAFEPROCESS'97)*, pages 1017–1022, 1997.

[63] W. R. Hamilton. On quaternions, or on a new system of imaginaries in algebra. *The London, Edinburgh and Dublin Philosophical Magazine and Journal of Science*, xxv:10–13, 1844.

[64] S. Hansen and M. Blanke. Control surface fault diagnosis for small autonomous aircraft. In *Proceedings of the 1st. Australian Control Conference*, 2011.

[65] S. Hansen, M. Blanke, and J. Adrian. Diagnosis of uav pitot tube defects using statistical change detection. In *7th Symposium on Intelligent Autonomous Vehicles*, 2010.

[66] O. Härkegård. Efficient active-set algorithms for solving constrained least-square problems in aircraft control allocation. In *IEEE Conference on Decision and Control*, December 2002.

[67] A. J. Healey and D. B. Lienard. Multivariable sliding mode control for autonomous diving and steering of unmanned underwater vehicles. *IEEE Journal of Oceanic Engineering*, OE-18(3):327–339, 1993.

[68] D. Henry. Fault diagnosis of the microscope satellite thrusters using h_∞/h_- filters. *AIAA Journal of Guidance, Control, and Dynamics*, 31 (3):699–711, 2008.

[69] G. Heredia, A. Ollero, M. Bejar, and R. Mahtani. Sensor and actuator fault detection in small autonomous helicopters. *Mechatronics*, 18:90–99, 2008.

[70] R. Isermann. Supervision, fault-detection and fault-diagnosis methods - an introduction. *Control Engineering Practice*, 5(5):639–652, May. 1997.

[71] R. Isermann. Model-based fault-detection and diagnosis – status and applications. *Annual Reviews in Control*, 29:71–85, 2005.

[72] R. Isermann. *Fault-diagnosis systems:An introduction from fault detection to fault tolerance.* Springer, 2005.

[73] H. Jamouli, D. Sauter, and J.-Y. Keller. A new adaptive kalman estimator for detection and isolation of multiple faults using modified glr test. In *Conf. on Control and Fault Tolerant Systems*, pages 76–81, Nice, October 2010.

[74] S. J. Julier and J. K. Uhlmann. A new extension of the kalman filter to nonlinear systems. In *Proceedings of AeroSense: The 11th international symposium on aerospace/defense sensing, simulation and controls*, 1997.

[75] S. Julier. The Spherical Simplex Unscented Transformation. In *American Control Conference*, volume 3, pages 2430–2434. IEEE, 2003.

[76] S. Julier and J. Uhlmann. Reduced Sigma Point Filters for the Propagation of Means and Covariances Through Nonlinear Transformations. In *American Control Conference*, volume 2, pages 887–892. IEEE, 2002.

[77] S. M. Kay. *Fundamentals of Statistical Signal Processing: Detection Theory*. Prentice-Hall PTR, 1998.

[78] W. B. Keegan. Terrestrial environment (climatic) criteria handbook for use in aerospace vehicle development.". Technical Report NASA-HDBK-1001, Nasa Technical Standards Program, 2000.

[79] H. K. Khalil. *Nonlinear Systems*. Prentice Hall, 3rd edition, 2002.

[80] V. Klein and E. A. Morelli. *Aircraft System Identification. Theory and Practice*. American Institute of Aeronautics and Astronautics, 2006.

[81] T. Krüger, P. Schnetter, R. Placzek, and P. Vörsmann. Nonlinear adaptive control using sliding mode online learning. In *International Joint Conference on Neural Networks*, pages 2897–2904, 2011.

[82] T. Krüger, P. Schnetter, R. Placzek, and P. Vörsmann. Fault-tolerant nonlinear adaptive flight control using sliding mode online learning. *Neural Networks*, 32:267–274, 2012.

[83] E. P. Lesley. Propeller tests to determine the effect of number of blades at two typical solidities. Technical report, National Advisory Committee For Aeronautics, 1939.

[84] R. Lin, E. Khalastchi, and G. A. Kaminka. Detecting anomalies in unmanned vehichles using the mahalanobis distance. In *IEEE International Conference on Robotics and Automation*, 2010.

[85] L. Ljung. Asymptotic behavior of the extended kalman filter as a parameter estimator for linear systems. *IEEE Transactions on Automatic Control*, 24 (1):36–50, 1979.

[86] J. Lozano, L. Carrillo, A. Dzul, and R. Lozano. Spherical Simplex Sigma-Point Kalman Filters: A comparison in the inertial navigation of a terrestrial vehicle. In *American Control Conference*, pages 3536–3541. IEEE, 2008.

[87] D. Magill. Optimal adaptive estimation of sampled stochastic processes. *Automatic Control, IEEE Transactions on*, 10:434–439, 1965.

[88] R. Mahony, M. Euston, J. Kim, P. Coote, and T. Hamel. A non-linear oberver for attitude estimation of a fixed-wing aerial vehicle without gps measurements. *Transactions of the Institute of Measurement and Control*, 33(6):699–717, 2011.

[89] A. Marcos and G. J. Balas. A boeing 747-100/200 aircraft fault tolerant and fault diagnostic benchmark. Technical report, Department of Aerospace and Engineering Mechanics, University of Minnesota, 2003.

[90] A. Marcos, S. Ganguli, and G. J. Balas. An application of h_∞ fault detection and isolation to a transport aircraft. *Control Engineering Practice*, 13(1):105–119, 2005.

[91] J. Marzat, H. Piet-Lahanier, F. Damongeot, and E. Walter. Model-based fault diagnosis for aerospace systems: a survey. *Journal of Aerospace Engineering*, 226(10):1329–1360, 2012.

[92] Meggitt Defence Systems Ltd. Banshee aerial target system, 2008. URL `http://www.meggittdefenceuk.com/PDF/Bansheeaerialtargetsystem.pdf`.

[93] Meggitt Defence Systems Ltd. Meggitt defence systems uk, 2012. URL `http://www.meggittdefenceuk.com/`.

[94] L. Meng, L. Li, and S. Veres. Comparison of linear and nonlinear aerodynamic parameter estimation approaches for an unmanned aerial vehicle using unscented kalman filter. *Journal of Beijing Institute of Technology*, 20(3), 2011.

[95] H. Moncayo, M. G. Perhinschi, and J. Davis. Aircraft failure detection and identification using an immunological hierarchical multiself strategy. *AIAA Journal of Guidance, Control, and Dynamics*, 33(4):1105–1114, 2010.

[96] H. Moncayo, M. G. Perhinschi, and J. Davis. Artificial-immune-system-based aircraft failure evaluation over extended flight envelope. *AIAA Journal of Guidance, Control, and Dynamics*, 34(4):989–1001, 2011.

[97] M. R. Napolitano, Y. An, and B. A. Seanor. A fault tolerant flight control system for sensor and actuator failures using neural networks. *Aircraft Design*, 3:103–128, 2000.

[98] H. Niemann. A setup for active fault diagnosis. *IEEE Trans. on Automatic Control*, 51(9):1572–1578, September 2006.

[99] H. D. Nissen. *Instrumentation and Control of Unmanned Air Vehicle*. PhD thesis, Technical University of Denmark, 2002.

[100] M. Nørgaard, N. K. Poulsen, and O. Ravn. New developments in state estimation for nonlinear systems. *Automatica*, 36:1627–1638, 2000.

[101] R. Pandita. *Dynamic Flight Envelope Assessment with Flight Safety Applications*. PhD thesis, University of Minnesota, 2010.

[102] W. Park, S. H. Lee, and J. Song. Fault detection and isolation of durumi-ii using similarity measure. *Journal of Mechanical Science and Technology*, 23:302–310, 2009.

[103] R. J. Patton. Fault detection and diagnosis in aerospace systems using analytical redundancy. *IEE Computing & Control Eng. J.*, 2(3):127–136, 1991.

[104] R. J. Patton, P. M. Frank, and R. N. Clark, editors. *Fault Diagnosis in Dynamic Systems, Theory and Application*. Control Engineering Series. Prentice Hall, New York, 1989.

[105] T. Perez, B. Williams, and P. de Lamberterie. Evaluation of robust autonomy and implications on UAS certification and design. In *28th International Congress of the Aeronautical Sciences (ICAS)*, Brisbane, Australia, September 2012.

[106] T. Perez. Anti-windup designs for ship dynamic positioning with control allocation. In *Proc. of the 8th IFAC International Conference on Manoeuvring and Control of Marine Craft*, Guaruja, Brazil, 2009.

[107] T. Perez, A. Donaire, P. de Lamberterie, and B. Willams. Joint motion control and control allocation design for UAS flight control systems. In *AIAA infotech@Aerospace, Saint Louis, Missouri*, 2011.

[108] T. Perez, A. Donaire, P. de Lamberterie, and B. Williams. A framework for testing robust autonomy of uas during design and certification. In *AIAA Infotech@Aerospace Conference and Exhibit*, volume 1, pages 303–315, 2011.

[109] M. G. Perhinschi, M. R. Napolitano, G. Campa, B. A. Seanor, J. Burken, and R. Larson. An adaptive threshold approach for the design of an actuator failure detection and identification scheme. *IEEE Transactions on Control Systems Technology*, 14(3):519–525, 2006.

[110] M. G. Perhinschi, J. Porter, H. Moncayo, J. Davis, and W. S. Wayne. Artificial-immune-system-based detection scheme for aircraft engine failures. *AIAA Journal of Guidance, Control, and Dynamics*, 5(5):1423–1440, 2011.

[111] J. A. M. Petersen and M. Bodson. Constrained quadratic programming techniques for control allocation. *IEEE Control Systems Technology*, 14 (1):91–97, January 2006.

[112] R. Pieper. Comparing estimation algorithms for camera position and orientation. *Department of Electrical Engineering, Linköpings universitet, SE581*, 83, 2007.

[113] L. Pivano, T. A. Johansen, and O. N. Smogeli. A four-quadrant thrust estimation scheme for marine propellers: Theory and experiments. *IEEE Transactions on Control Systems Technology*, 17 (1):215–226, 2009.

[114] N. K. Poulsen and H. Niemann. Active fault diagnosis based on stochastic tests. *International Journal of Applied Mathematics and Computer Science*, 18 (4):487–496, 2008.

[115] D. P. Raymer. *Aircraft Design: A Conceptual Approach*. AIAA Education Series, 4 edition, 2006.

[116] E. Ruth, O. Smogeli, T. Perez, and A. Sorensen. Antispin thrust allocation for marine vessels. *IEEE Transactions on Control Systems Technology*, 17 (6):1257 – 1269, Nov 2009. doi: 10.1109/TCST.2008.2006187.

[117] I. Samy, I. Postlethwaite, and D.-W. Gu. Unmanned air vehicle air data estimation using a matrix of pressure sensors: a comparison of neural networks and look-up tables. *Journal of Aerospace Engineering*, 225 (7): 807–820, 2011.

[118] I. Samy, I. Postlethwaite, and D.-W. Gu. Neural network based sensor validation scheme demonstrated on an unmanned air vehicle (uav) model. In *Proceedings of the 47th IEEE Conference on Decision and Control*, 2008.

[119] I. Samy, I. Postlethwaite, and D.-W. Gu. A comparative study of nn- and ekf-based sfda schemes with application to a nonlinear uav model. *International Journal of Control*, 83:1025–1043, 2010.

[120] D. Shore and M. Bodson. Flight testing of a reconfigurable control system on an unmanned aircraft. *AIAA Journal of Guidance, Control, and Dynamics*, 28(4):698–707, 2005.

[121] Y. Shtessel, J. Buffington, and S. Banda. Multiple timescale flight control using reconfigurable sliding modes. *Journal of Guidance, Control, and Dynamics*, 22(6):873–883, 1999.

[122] B. L. Stevens and F. L. Lewis. *Aircraft Control and Simulation*. John Wiley & Sons, 2nd edition, 2003.

[123] C. P. Tan and C. Edwards. Sliding mode observers for robust detection and reconstruction of actuator and sensor faults. *International Journal of Robust and Nonlinear Control*, 13:443–463, 2003.

[124] A. Tornambé. Use of asymptotic observers having high-gains in the state and parameters estimation. In *Proceedings of the 28th Conference on Decision and Control*, 1989.

[125] R. van der Merwe and E. A. Wan. The square-root unscented kalman filter for state and parameter-estimation. In *IEEE International Conference on Acoustics, Speech and Signal Processing*, 2001.

[126] R. van der Merwe and E. A. Wan. Sigma-Point Kalman Filters for Integrated Navigation. In *Proceedings of the 60th Annual Meeting of the Institute of Navigation (ION)*, pages 641–654. Citeseer, 2004.

[127] G. Verdier and N. H. A. J.-P. Vila. Adaptive threshold computation for cusum-type procedures in change detection and isolation problerms. *Computational Statistics and Data Analysis*, 52:4161–4174, 2008.

[128] H. Wagner, G. Nikolov, A. Bierig, and H. Spangenberg. Challenges for health monitoring of electromechanical flight control actuation systems. *SAE International Journal of Aerospace*, 4 (2):1315–1327, 2011.

[129] E. Walter and L. Pronzato. *Identification of Parametric Models form Experimental Data*. Springer, 1997.

[130] R. E. Weibel and R. J. Hansman. Safety considerations for operation of unmanned aerial vehicles in the national airspace system. Technical report, MIT International Center for Air Transportation, 2005.

[131] T. J. Wheeler, P. Seiler, A. K. Packard, and G. J. Balas. Performance analysis of fault detection systems based on analytically redundant linear time-invariant dynamics. In *Proc. 2011 American Control Conference (ACC 2011)*, pages 214–219, 2011.

[132] A. S. Willsky and H. L. Jones. A generalized likelihood ratio approach to detection and estimation of jumps in linear systems. *IEEE Transactions on Automatic Control*, 21:108–112, 1976.

[133] N. E. Wu, S. Thavamani, Y. Zhang, and M. Blanke. Sensor fault masking of a ship propulsion system. *Control Engineering Practice*, 14:1337—-1345, 2006.

[134] N. E. Wu. Coverage in fault-tolerant control. *Automatica*, 40:537–548, 2004.

[135] X. Yu and J. Jiang. Fault-tolerant flight control system design against control surface impairments. *IEEE Aerospace and Electronics Systems*, 20(4):871–886, 2012.

[136] X. Yu and J. Jiang. Hybrid fault-tolerant flight control system design against partial actuator failures. *IEEE Transactions on Control Systems Technology*, 20(4):872–876, 2012.

[137] W. Zeng, X. Zhu, Y. Li, and Z. Li. Less Computational Unscented Kalman Filter for Practical State Estimation of Small Scale Unmanned Helicopters. In *International Conference on Robotics and Automation*, pages 1658–1663. IEEE, 2011.

[138] X. Zhang. *Auxiliary signal design in fault detection and diagnosis*. Springer Verlag, 1989.

[139] K. Zhao and Z. You. Satellite Attitude Determination Filter using Square Root based Spherical Simplex Unscented Transformation. *International Journal of Computer Network and Information Security (IJCNIS)*, 3(4): 32, 2011.

[140] Q. Zhao and M. Kinnaert. Statistical properties of cusum based fault detection schemes for fault tolerant control. In *Proc.* 48^{th} *IEEE Conference on Decision and Control*, pages 7831–7836, 2009.

[141] W.-w. Zhou and M. Blanke. Identification of a class of non-linear state space models using rpe techniques. *IEEE Transactions of Automatic Control*, 34 (3):312–316, 1989.

[142] P. Zipfel. *Modeling and Simulation of Aerospace Vehicle Dynamics*. American Institure of Aeronautics and Astronautics (AIAA), 2007.

[143] A. Zolghadri. Advanced model-based fdir techniques for aerospace systems: Today challenges and opportunities. *Progress in Aerospace Sciences*, 53:18–29, 2012.

Paper A

Diagnosis of UAV Pitot Tube Defects Using Statistical Change Detection[1]

Søren Hansen, Mogens Blanke and Jens Adrian

Abstract

Unmanned Aerial Vehicles need a large degree of tolerance to faults. One of the most important steps towards this is the ability to detect and isolate faults in sensors and actuators in real time and make remedial actions to avoid that faults develop to failure. This paper analyses the possibilities of detecting faults in the pitot tube of a small unmanned aerial vehicle, a fault that easily causes a crash if not diagnosed and handled in time. Using as redundant information the velocity measured from an onboard GPS receiver, the air-speed estimated from engine throttle and the pitot tube based airspeed, the paper analyses the properties of residuals. A dedicated change detector is suggested that works on pre-whitened residuals and a generalised likelihood ratio test is derived for a Cauchy probability density, which the residuals are observed to have. A detection scheme is obtained using a threshold that provides desired quantities of false alarm and detection probabilities. Fault detectors are build based on raw residual data and on a whitened edition of these. The two detectors are compared against recorded telemetry data of an actual event where a pitot tube defect occurred.

[1]In proceedings of 7th Symposium on Intelligent Autonomous Vehicles, IAV2010.

A.1 Introduction

Defects on sensors can have catastrophic consequences for airplanes, specially smaller airplanes, which do not have the same sensor redundancy that is available on larger aircraft. It is therefore important to be able to detect whether a sensor defect has occurred. One of the most important sensors is the pitot tube that measures airspeed of the vehicle. This sensor is very exposed because of its position in the airstream and can easy be clogged by dust or water particles that freeze at higher altitudes, when they come in contact with the airplane body.

The solution to these clogging problems usually employed on larger aircrafts is to install several pitot tubes with build in heating devices to have a redundant system that can accommodate icing. Because of weight and space limitations, adding more sensors is usually not an option on smaller unmanned aerial vehicles (UAV). Therefore, a different approach must be taken to diagnose and accommodate faults. One way could be to have artifact readings detected and replaced with estimated values. Detection of faults and fault-tolerance for UAVs has a lot of focus and, as described in [44], many parts of the aircraft control and operation can benefit from using fault tolerant methods. A systematic approach to fault detection is described in [50] and some of the applications of these methods are, detection of mechanical defects, like stuck control surfaces. These were studied in [15] and [102] where active methods were used to isolate faults. Observer based fault diagnosis was investigated in e.g. [69]. Nonlinear models that describe the aircraft can also be used in fault diagnosis, this was demonstrated on small helicopters in [51].

This paper investigates the use of GPS velocity measurements and propeller thrust readings to generate speed information that is redundant compared to the pitot tube airspeed. Residual values are formed from which defects on the pitot tube can be isolated. The detection is done using statistical information gathered from telemetry records from a Banshee UAV (see fig. A.1). Advantage is taken of availability of real data to derive probability density functions and establish spectral properties of data. Dedicated change detection is derived based on observed signal properties and detectors are convincingly tested on real data from an incident involving icing of the pitot tube.

A.2 Platform

The UAV studied in this paper is a Banshee target drone build by the British company Meggitt Defence System.

The airplane is controlled by an autopilot and the operator sends set-point requests to height, speed and heading. Telemetry data are send from the plane and logged at a ground station. These data are the basis for the investigations presented in this paper.

The Banshee is a delta wing aircraft equipped with a small rear mounted engine.

The thrust is delivered by a two-bladed wooden propeller. It is launched from a catapult system (see fig. A.1) and lands by parachute. It is therefore not equipped with any landing gear.

Figure A.1: Banshee UAV ready for launch at the Danish Naval Weapons School at Sjællands Odde. (*Foto: VFD*)

A.3 Model

The airplane is modelled by the dynamic and kinematic equations, which describe its motion through the air. In order to describe these concepts mathematically, a number of reference frames are needed. These are the ECEF (Earth centred earth fixed) frame, the VCE (Vehicle carried earth) frame, the body frame and the wind frame, see e.g [122] for details.

A.3.1 Airplane motion parameters

The airplane's motion is described by its velocities in the body coordinate system

$$\boldsymbol{v}_b = [u, v, w]^\mathsf{T}, \tag{A.1}$$

and the rotational rate about the body axes,

$$\boldsymbol{\omega} = [p, q, r]^\mathsf{T}. \tag{A.2}$$

The Euler angles used to describe the rotation between the vehicle carried coordinate frame and the body frame of the aircraft are,

$$\boldsymbol{\Phi} = [\phi, \theta, \psi]^\mathsf{T}. \tag{A.3}$$

This is also the attitude and heading information.

A.3.2 Kinematics

The kinematics of the airplane relates the angular velocities $\boldsymbol{\omega}$ to the rate of change in the Euler angles $\dot{\boldsymbol{\Phi}}$, which are used in the rotation between body and the VCE coordinate system. This is given by the following relation

$$\dot{\boldsymbol{\Phi}} = \boldsymbol{L}(\boldsymbol{\Phi})\boldsymbol{\omega} \tag{A.4}$$

$$\boldsymbol{L}(\boldsymbol{\Phi}) = \begin{bmatrix} 1 & \tan\theta\sin\phi & \tan\theta\cos\phi \\ 0 & \cos\phi & -\sin\phi \\ 0 & \sin\phi/\cos\theta & \cos\phi/\cos\theta \end{bmatrix} \tag{A.5}$$

The change in position in the ECEF reference frame can be described by rotating the translational velocities $\boldsymbol{v}_b$ to the navigation frame. The transformation matrix involved in this depends on $\boldsymbol{\Phi}$.

A.3.3 Dynamics

The airplane is seen as a rigid body moving through the air. Newton's and Euler's laws for linear and angular momentum relate forces and moments acting on the rigid body to linear and angular velocities and accelerations. Since the UAV is flying at low speed and height over a relatively small area, we assume that the Earth is flat, and Coriolis forces and the centripetal force from the curvature of the Earth can be neglected.
The airplane is affected by a thrust from the engine $\boldsymbol{F}_T$, an aerodynamic force $\boldsymbol{F}_A$ arising from the lift and drag from the airplane body and, naturally, the gravitational force from Earth $\boldsymbol{F}_G$. With mass m,

$$\frac{d}{dt}(m\boldsymbol{v}_b) = \sum \boldsymbol{F} = \boldsymbol{F}_T + \boldsymbol{F}_A + \boldsymbol{F}_G \tag{A.6}$$

Since this equation is expressed in the inertial frame (the Earth system) the equation of Coriolis is used to find the derivative,

$$m\dot{\boldsymbol{v}}_b + \boldsymbol{\omega} \times m\boldsymbol{v}_b = \boldsymbol{F}_T + \boldsymbol{F}_A + \boldsymbol{F}_G \tag{A.7}$$

For an in depth description of airplane dynamics see for instance [122].

A.3.4 Thrust

The Banshees' thrust is delivered by a rear mounted internal combustion engine that drives a 2 bladed wood propeller. The actual force delivered depends on the physical dimensions of the propeller, the engines revolutions and the density of the air. Given a propeller with diameter d_p rotating at n revolutions per second the thrust force is given by:

$$F_T = k_T \varrho n^2 d_p^4 \tag{A.8}$$

where k_T is the thrust coefficient and ϱ is the density of air. Wind tunnel tests (see [83]) of propellers of the used type show that the thrust coefficient is approximately linear with the advance ratio J as seen in [83] figure 5. The advance ratio is given by:

$$J = \frac{v}{nd_p}. \tag{A.9}$$

In nominal flight the advancement ratio is in the range 0.9 to 1.1.
Propellers are usually characterised by their diameter d_p and pitch P_p. These values can be combined to a non-dimensional pitch given by:

$$P' = \frac{P_p}{d_p} \tag{A.10}$$

In [99] the following scaling for the thrust coefficient was proposed.

$$k_T(J) \simeq k_{T,\text{ref}}(J - (P' - P'_{\text{ref}})) \tag{A.11}$$

where $k_{T,\text{ref}}$ and P'_{ref} is the thrust coefficient and non-dimensional pitch of the reference signal respectively. The reference signals originates from different propellers tested in [83]. Since the 26×30 inch propeller used on the Banshee has P', which is equal to one of the tested propellers, the characteristics of this propeller is used from this point on.
The thrust coefficient can be expressed in two terms describing the linear area seen in figure 5 in [83].

$$k_T = k_{T0} + k_{T1}J \tag{A.12}$$

By calculating the lift force of the propeller it was shown in [20] that the thrust can be expressed by:

$$F_T = T_{nn}n^2 + T_{nu}nu \tag{A.13}$$
$$T_{nn} = k_{T0}\varrho d^4 \tag{A.14}$$
$$T_{nu} = k_{T1}\varrho d^3 \tag{A.15}$$

The thrust force works in the x-direction of the body system. This gives rise to the following force equation in the x-direction by using Equation (A.7):

$$m\dot{u} + m\left(qw - rv\right) = F_{Tx} + F_{Ax} + mg\sin\theta \tag{A.16}$$

The aerodynamic force F_{Ax} is a combination of lift and drag forces on the airplane body. Since the angle of attack α is usually small this force primarily consists of the drag on the airplane. This is modelled on basis of recorded data to vary with θ. It is assumed that the engine is aligned with the airplane body and therefore $F_{Tx} = F_T$. In straight and level flight with no accelerations present we can estimate the forward air speed of the plane by inserting the thrust expression from equation A.13.

$$\hat{u} = \frac{-T_{nn}n^2 - F_{Ax} - mg\sin\theta}{T_{nu}n} \tag{A.17}$$

While this simple estimate was found to suffice for the purpose of fault diagnosis, more elaborate and sophisticated nonlinear observers and estimators have been suggested in the literature. [141] described a way to estimate state and parameters in nonlinear systems with a structure similar to the thrust equation here, [22] applied an adaptive observer scheme and [113] showed nonlinear observer designs for thrust estimation.

A.4 Signal analysis

The airspeed of the UAV is measured by pressure differences between the pitot tube input and the static vent input. This gives the difference between the stagnation pressure and the static pressure which, according to Bernoulli's theorem, is the dynamic pressure $\bar{q}$,

$$\bar{q} = \tfrac{1}{2}\varrho V^2 \tag{A.18}$$

From this the planes airspeed V can be calculated.
In order to detect an error in the airspeed indicator this sensor value must be compared to similar measurements. The GPS receiver gives a speed from its internal Kalman filter. This corresponds to the speed in an ECEF reference frame, but using knowledge about the wind speed and direction it can be transformed to airspeed measured in the pitot tube.
As seen in the previous chapter the speed in the body x-direction can be derived from the thrust equations developed by the engine, by using equation A.17. This measure can also be converted to match the airspeed measured by the pitot tube system.
The estimation of the wind direction and wind speed are crucial for the correctness of these conversions. These values are also hard to estimate with common means. However the wind is measured at the ground station, and also estimated during takeoff where the airplane always climbs into the wind direction. These estimates prove to give good results in practice.
The simplest way of comparing the three airspeed measurements are by subtracting them from each other. This creates three residual signals which in the nominal case should have a values around 0. If we denote the airspeed measured by the pitot tube $v_{airspeed}$, the airspeed calculated from the GPS v_{gps} and the airspeed calculated from the engine velocity v_{thrust} the following parity matrix can be formed:

	$v_{airspeed}$	v_{gps}	v_{thrust}
R_1	s	s	0
R_2	s	0	s
R_3	0	s	s

(A.19)

An 's' in list A.19 means that errors on this value is strongly detectable by the given residual. All the residual are generated from the difference between measurements of the airspeed velocity. This means that if the residual is different from zero it indicates a fault, on one of the signals. Therefore an detection of

a DC-signal of unknown magnitude, different from zero, in the residual, would indicate an error.
Since only R_1 and R_2 contains pitot pressure information only these two residuals are analysed onwards, however the same methods are applied to R_3 to obtain fault isolation.

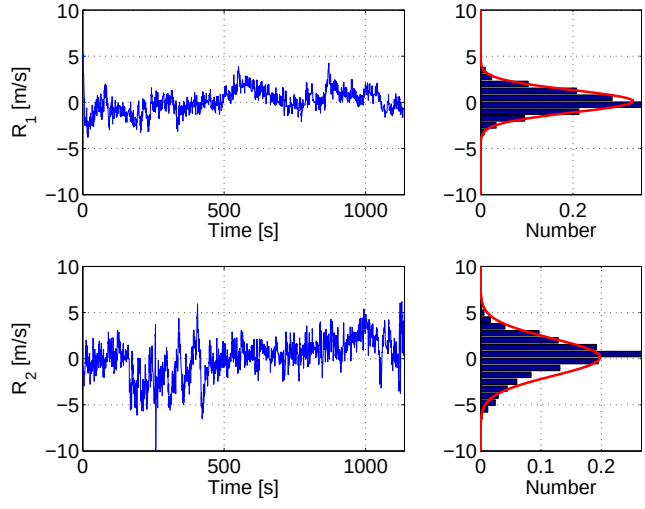

Figure A.2: Time development and histogram for residual R_1 and R_2 in the fault free case.

Figure A.2 shows a time history and a histogram for R_1 and R_2 in the fault free case.
As seen from the power spectrum densities in figure A.3 the noise present at the residual signals are not white. Since white noise is one of the requirements for most statistical change detectors to perform optimal, the low-pass filtered nature of the noise should be removed. One solution of dealing with coloured noise is to filter white noise through a suitable filter function to take into account the correlations present in the coloured noise. This can be created from a large record of data where all the signals properties are present. As indicated on figure A.3 the power spectrum density of the two residuals consists of a part which decreases with 40 dB/decade and a part which decreases with 80 dB/decade.
A filter function H which converts a white noise input to a coloured noise output according to

$$S_{rr}(\omega) = |H(\omega)|^2 S_{ww}(\omega) = H(j\omega)H^*(j\omega)S_{ww}(\omega) \tag{A.20}$$

can be created. The function should satisfy the shape given in figure A.3 and

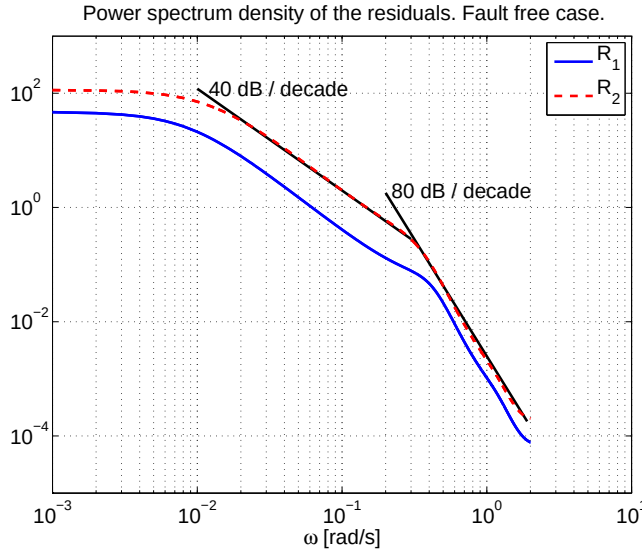

Figure A.3: Power spectrum densities for residual R_1 and R_2.

satisfy that

$$\frac{1}{2\pi}\int_{-\infty}^{\infty} S_{rr}(\omega)d\omega = \sigma_r^2 \tag{A.21}$$

where σ_r^2 is the variance of the residual noise. In order to satisfy the shape in the following PSD function is chosen.

$$\mathcal{P}(\omega) = K\frac{\tau_1\omega^2+1}{(\tau_1\omega^2+1)^2}\frac{\tau_2\omega^2+1}{(\tau_2\omega^2+1)^2} \tag{A.22}$$

where τ_1 is the reciprocal cut-off frequency between the 0 dB/decade and the -40 dB/decade parts and τ_2 is the time constant between -40 dB/decade and -80 dB/decade parts, and K is the magnitude. This corresponds to the following filter function.

$$\begin{aligned}\mathcal{P}(\omega) &= H(j\omega)H^*(j\omega) = \\ &\sqrt{K}\frac{\sqrt{\tau_1}j\omega+1}{\left(\sqrt{\tau_1}j\omega+1\right)^2}\frac{\sqrt{\tau_2}j\omega+1}{\left(\sqrt{\tau_2}j\omega+1\right)^2}\times \\ &\sqrt{K}\frac{-\sqrt{\tau_1}j\omega+1}{\left(-\sqrt{\tau_1}j\omega+1\right)^2}\frac{-\sqrt{\tau_2}j\omega+1}{\left(-\sqrt{\tau_2}j\omega+1\right)^2}\end{aligned} \tag{A.23}$$

The constants in the equation are found by optimising $H(j\omega)$ to fit the actual spectra.

Expressing the filter function function in terms of s gives

$$H(s) = \sqrt{K}\frac{\sqrt{\tau_1}s+1}{\left(\sqrt{\tau_1}s+1\right)^2}\frac{\sqrt{\tau_2}s+1}{\left(\sqrt{\tau_2}s+1\right)^2} \tag{A.24}$$

The filter is implemented digitally using an IIR representation. Since filtering white noise through $H(s)$ should create a noise signal with a power spectrum similar to the one in figure A.3 filtering R_1 and R_2 through $H^{-1}(s)$ should create a signal with a flat power spectrum. Figure A.5 shows the result of the

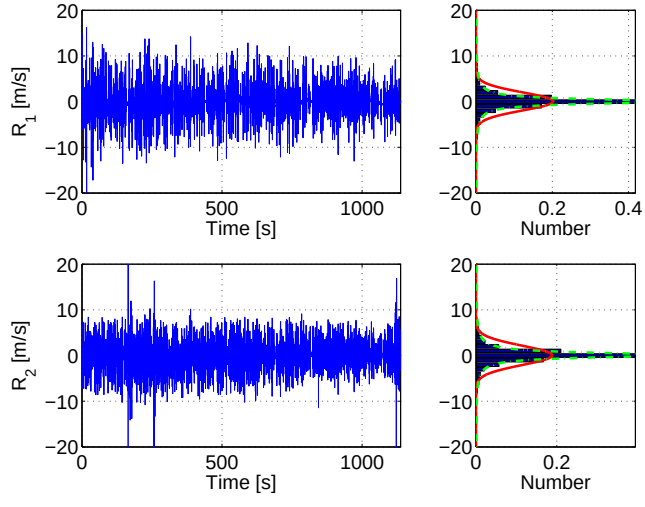

Figure A.4: Time development and histogram for the whitened residual R_1 and R_2 in the fault free case.

whitening. Both residuals features now white noise. In figure A.4 the time development and the histogram is plotted. Neither of the residuals are now Gaussian distributed. Instead they follow the Cauchy distribution (equation A.34) very well as indicated by the green dotted line in the histogram. The Gaussian nature that the residuals has before whitening comes from the effect of the low-pass filtering, which creates the power spectra observed. When this is removed during the whitening process the Gaussianity is also removed.

A.5 Detectors

Two approaches to change detection is investigated. In the first one the raw residual signals are used and the next one the whitened signals are used.

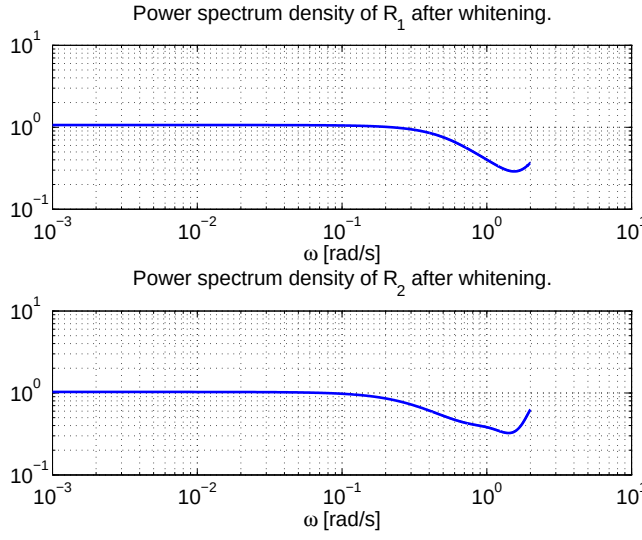

Figure A.5: Power spectrum densities after whitening for residual R_1 and R_2 in the fault free case.

A.5.1 Raw residual detector

If the vocabulary from statistical change detection is used the scenario that it is desirable to analyse is: Detect an unknown DC-level in Gaussian white noise. If the signal is denoted x we wish to distinguish between the following two hypotheses:

$$\begin{aligned} \mathcal{H}_0 : x[n] &= w[n] \\ \mathcal{H}_1 : x[n] &= A + w[n] \end{aligned} \tag{A.25}$$

The unknown parameters are: The DC-level A and the variance of the noise σ_w^2. The GLRT (Generalised Likelihood Ratio Test) for a linear model formulation can be used to solve such a problem. However, GLRT algorithm assumes that the signal noise is white. As emphasised, this is not the case for the raw residual. However, the algorithm is tested anyway using the raw residual, to see how it performs. The general GLRT detector is given by

$$L_G(\boldsymbol{x}) = \frac{p\left(\boldsymbol{x}; \hat{\boldsymbol{\Theta}}_1\right)}{p\left(\boldsymbol{x}; \hat{\boldsymbol{\Theta}}_0\right)} > \gamma \tag{A.26}$$

If the ration is larger than the threshold γ this decides $\mathcal{H}_1$. $\hat{\boldsymbol{\Theta}}_i$ is the maximum likelihood estimate (MLE) of the parameters when hypothesis $\mathcal{H}_i$ is true. In

general the GLRT test for the following two hypotheses:

$$\begin{aligned} \mathcal{H}_0 : \boldsymbol{A\Theta} &= \boldsymbol{b}, \quad \sigma_w > 0 \\ \mathcal{H}_1 : \boldsymbol{A\Theta} &\neq \boldsymbol{b}, \quad \sigma_w > 0 \end{aligned} \tag{A.27}$$

The linear model is given by $\boldsymbol{x} = \boldsymbol{H\Theta} + \boldsymbol{w}$. The problem given by equation A.25 can be transformed to this problem if we choose $\boldsymbol{\Theta} = [A]$, $\boldsymbol{A} = [1]$ and $\boldsymbol{b} = [0]$. The matrix $\boldsymbol{H}$ is chosen to be a column of 1 corresponding to the window size N.

$$T(\boldsymbol{x}) = (N-1)\frac{(\boldsymbol{A}\hat{\boldsymbol{\Theta}}_1 - \boldsymbol{b})^\mathsf{T}\left(\boldsymbol{A}(\boldsymbol{H}^\mathsf{T}\boldsymbol{H})^{-1}\boldsymbol{A}^\mathsf{T}\right)^{-1}(\boldsymbol{A}\hat{\boldsymbol{\Theta}}_1 - \boldsymbol{b})}{\boldsymbol{x}^\mathsf{T}(\boldsymbol{I} - \boldsymbol{H}(\boldsymbol{H}^\mathsf{T}\boldsymbol{H})^{-1}\boldsymbol{H}^\mathsf{T})\boldsymbol{x}} \tag{A.28}$$

Inserting the values of $\boldsymbol{A}$, $\boldsymbol{b}$, $\boldsymbol{H}$ and $\hat{\boldsymbol{\Theta}}_1$ gives

$$T(\boldsymbol{x}) = (N-1)\frac{\bar{x}^2}{\hat{\sigma_w}^2} \tag{A.29}$$

Where $\bar{x}$ is the sample mean and the MLE of the variance is given by:

$$\hat{\sigma_w}^2 = \frac{1}{N}\boldsymbol{x}^\top\left(\boldsymbol{I} - \boldsymbol{H}\left(\boldsymbol{H}^\top\boldsymbol{H}\right)^{-1}\boldsymbol{H}^\top\right)\boldsymbol{x} \tag{A.30}$$

which just ends up with being the variance of the test data. The final test statistic is therefore

$$T(\boldsymbol{x}) = (N-1)\frac{\bar{x}^2}{\mathrm{var}(\boldsymbol{x})} > \gamma' \tag{A.31}$$

A more elaborate derivation of the detector can be found in [77]. The probability of false alarms P_{FA} and the probability of detection P_D is given by:

$$P_{FA} = Q_{F_{r,N-p}}(\gamma') \tag{A.32}$$

and

$$P_D = Q_{F'_{r,N-p}(\varsigma)}(\gamma') \ ; \ \varsigma = \frac{N\ A^2}{\sigma_w^2} \tag{A.33}$$

where Q denotes the right tail probability.

A.5.2 Pre-whitened residual detector

The second detector works on the whitened residuals. Since these are distributed according to a Cauchy distribution (as seen from figure A.4) the following probability distribution function most be used

$$p(x; x_o, \beta) = \frac{\beta}{\pi\left(x - x_o\right)^2 + \beta^2} \tag{A.34}$$

The two parameters is the half-width half-maximum scaling, β, and the offset x_o. The hypotheses are the same as in the nonwhite case, is a DC-level present in the noise or not. The GLRT test statistic becomes

$$L_G(\boldsymbol{x}) = \frac{\prod_{i=1}^{N} p\left(x_i; \hat{x_o}, \hat{\beta}\right)}{\prod_{i=1}^{N} p\left(x_i; 0, \hat{\beta}\right)} > \gamma \tag{A.35}$$

The MLEs of $\hat{\beta}$ and $\hat{x_o}$ is found by fitting the data to equation A.34.
The performance can be calculated using these formulas:

$$P_{FA} = Q_{\chi^2}(\gamma') \tag{A.36}$$

and

$$P_D = Q_{\chi^2(\lambda)}(\gamma') \; ; \; \lambda = \frac{N \; A^2}{\sigma_w^2} \tag{A.37}$$

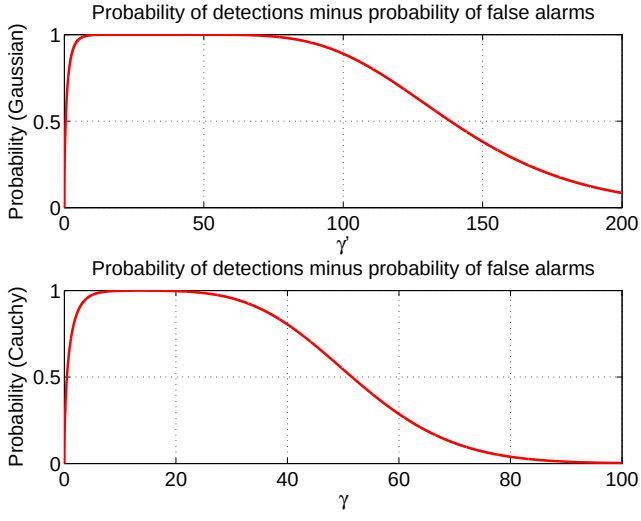

Figure A.6: Performance of the two detectors plotted as the difference between probability of detections and false alarms. Note that the value of γ and γ' can not be compared numerically.

Using the performance equations the compare value γ can be found. A plot of the detection performance minus the probability of false alarms for both the detector using the raw residual values and the one working on the whitened residuals are shown. For both performance curves a DC-level of 5 m/s has been chosen as the value wanted to be detected. Difference below this can be down to inaccuracies in the estimation of parameters in the velocity calculations.

A.6 Results

To test the two detectors, they were exposed to a data record containing a pitot tube defect. The results are shown together with the residuals in Figures A.7 and A.8.

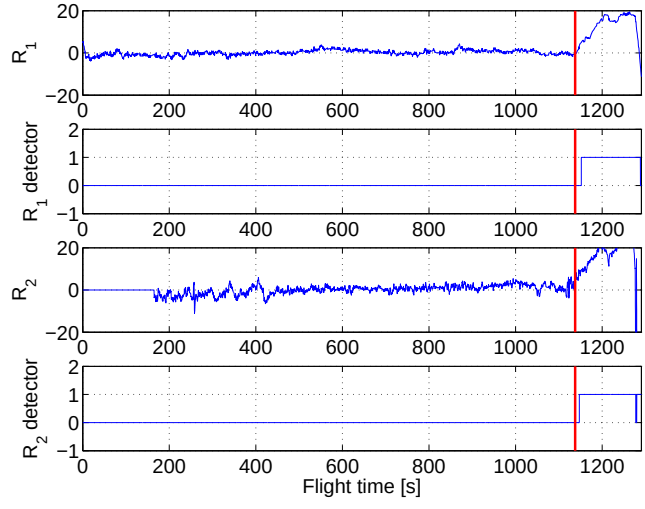

Figure A.7: Residuals and detector output. At approximately $t = 1140$ s the clogging of the pitot tube occurs (marked with the red vertical line).

As seen on the figures both detectors perform very well with the given data. They raise an alarm, indicated by a value of 1, about 14 seconds after the incident occurs. In order to get the raw residual detector to perform as shown in figure A.7 the comparison value γ' must be chosen 100 times larger than the one shown as maximal value in the top plot of figure A.6. The reason for this is the coloured noise degrading the performance.

A.7 Conclusion

The UAV's airspeed sensor faults were detected in this paper using a setup where inherent redundancies were used to generate residuals. Information from an onboard GPS receiver and the air speed estimated from engine thrust we used as sources of redundant information. Statistical properties of residuals were investigated and a whitening filter was designed to pre-whiten the residuals before applying a change detector. A dedicated detector was derived as a generalised likelihood ratio test for the log-likelihood ratio of probability density functions with and without faults. Change detection was obtained with thresholds calculated for the Cauchy distribution that pre-whitened residuals were found to

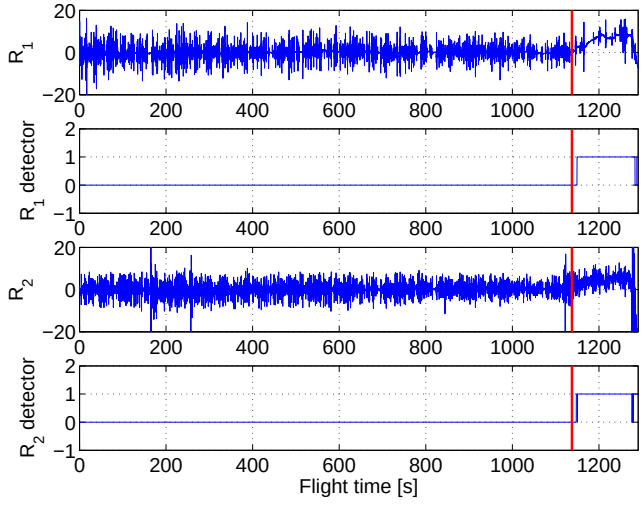

Figure A.8: Residuals and detector output. At approximately $t = 1140$ s the clogging of the pitot tube occurs (marked with the red vertical line).

follow. Detection thresholds were determined to find an optimal balance between probabilities for correct detection and false alarms. Two detectors were designed and tested against data records from an UAV with a pitot tube defect that developed while the UAV was in the air. Both detectors were able to detect the fault within an acceptable time frame and demonstrated that a *hard landing* could have been avoided with the proposed diagnostic system.

Paper B

Control Surface Fault Diagnosis for Small Autonomous Aircraft[1]

Søren Hansen and Mogens Blanke

Abstract

Small unmanned aerial vehicles require a large degree of fault-tolerance in order to fulfil their duties in an satisfactory way, both with respect to economy and safety in operation. Small aerial vehicles are commonly constructed without much redundancy in hardware, primarily for reasons of cost but also weight. Single point of failure solutions are therefore commonly used and operation is typically allowed only in closed airspace. In order to enhance dependability, fault prognosis and diagnosis are needed. This paper explores principal redundancies at an overall level, whether based on hardware or being analytical, and formulates residuals from which faults can be prognosed or diagnosed. An approach is suggested where detailed modelling is not needed but normal behaviour is learned from short segments of flight data using adaptive methods for learning. Statistical characterisation of distributions and change detection methods are employed to reach decisions about not-normal behaviour and it is shown how control surface faults can be diagnosed for a specific UAV without adding additional hardware to the platform. Only telemetry data from the aircraft are used together with a basic model of relations between measured state variables of the aircraft. Frequency domain methods are shown to be robust in exploring relevant properties of these signals. The detection is shown to work on data from a real incident where an aileron mechanism was damaged during launch of a UAV.

[1]In proceedings of 1st Australian Control Conference, AUCC2011.

B.1 Introduction

A common problem when using small unmanned aerial vehicles (UAV) is loss or partly loss of a control surface action. Because of redundancies in the control actions the airplane is some times able to continue flying within a reduced flight envelope. However the UAV operator may not be aware of the problem on the aircraft and therefore command a manoeuvre that exceeds the reduced flight envelope. This can cause dangerous situations if the autopilot looses control of the aircraft. It is therefore important to be able to diagnose these failures and alert the operator before the airplane lost. If the problem is diagnosed in time the operator may be able to bring down the airplane in a safe manner and avoid a hazardous situation.

Fault diagnosis and fault-tolerant control for airplanes has been explored by several authors. A structural analysis approach to diagnosis was considered in [50] where additive faults were diagnosed on sensors and actuators. Diagnosis of degraded control surfaces were studied in [15], [13], [11] and [102] where active methods were used to isolate specific faults. Observer based fault diagnosis was investigated in e.g. [69] and nonlinear models that describe the aircraft can also be used in fault diagnosis, which was demonstrated on small helicopters in [51]. Model-free methods were also proposed for instance by [84], where use of the Mahalanobis distance has been utilised to diagnose deviations from normal behaviour in autonomous vehicles. The topic of fault diagnosis for airplanes are not only of academic interest but is also important to the industry as seen in e.g. [57].

Diagnosis of loss or partial loss of a control surface is the subject in this paper. It is investigated how a relationship between inputs and measurements can be estimated and subsequently used for diagnosis of the faults, without detailed mathematical models. The cross spectrum and power spectrum between the UAV's angular rates, measured by an onboard gyro, are used to estimate the dynamic relation between the measured states. Using this relationship a residual signal can be formed. If a sudden change in this signal occurs, indicating that some normal relations are violated, a fault must have occurred.

The paper is divided into four sections. A short introduction to the mathematical equations, describing an aircraft, is first presented. Here emphasis is put on the controls available on a particular UAV, for which flight records are available with and without control surface faults. The theory behind generation and estimation of residuals based on data is then presented followed by a discussion of diagnostic properties when data based learning is used. The theory behind the change detection used to decide whether the aircraft is experiencing a normal or a not-normal behaviour is then treated and, finally, the developed diagnosis system is tested on data from a real UAV. Data from an incident where a control surface gets stuck during launch are analysed.

B.2 The Banshee Drone

The UAV considered in this paper is a Banshee target drone build by the British company Meggitt Defense System. The system is primarily used for target practice, but also surveillance and reconnaissance is possible. It can be equipped with various payloads for triggering and measuring the performance of the weapon system in use. The Banshee drone is used by the military in over 30 countries [92].

The UAV is a delta wing aircraft equipped with a small rear mounted engine. The thrust is delivered by a 2 bladed wooden propeller. It is launched from a catapult system and lands by parachute. It is therefore not equipped with any sort of landing gear. The airplane has an autopilot system and is operated from

Figure B.1: Banshee drone ready for launch at a Danish Defence exercise.

ground by an operator which commands the plane to fly between a number of waypoints.

Sensors and actuators

The aircraft has only two actuators, in addition to an engine throttle δ_t. These are aileron δ_a and elevator δ_e. These are placed side by side on the delta wing. The airplane uses a fixed tail which means that no rudder is present.

The Banshee is equipped with a barometric sensor which measures the flying height and a pitot tube to measure the airspeed. The onboard IMU estimates the attitude of the aircraft, based on measurements from INS sensors around the three axes of the aircraft. Apart from these a standard GPS is onboard to get the position of the aircraft and correct the attitude estimate.

B.3 Airplane model

An airplane can be modelled by the dynamic and kinematic equations which describes its motion through the air. To distinguish the coordinates describing the airplanes physical axes from the ones describing its attitude a number of reference frames are needed, see e.g. [122]. The body-frame and earth-frames are used in this paper.

B.3.1 Kinematics

The kinematics of the airplane relates the angular velocity in body coordinates $\boldsymbol{\omega}$ to the rate of change in the Euler angles $\dot{\Phi}$, related through $\dot{\Phi} = \mathbf{H}(\Phi)\boldsymbol{\omega}$ where $\mathbf{H}(\Phi)$ is a well-known function of the Euler angles. Translational velocities in body and navigation frames are related by the rotation $\mathbf{C}_{b2E}$ as $\dot{\boldsymbol{p}_E} = \mathbf{C}_{b2E}\boldsymbol{v}_b$.

B.3.2 Dynamics

The airplane is seen as a rigid body moving through the air. Newton - Euler equations relate the forces and moments acting on the rigid body to the velocities and accelerations. A flat earth assumption is employed.

Forces

The airplane is affected by a thrust force from the engine $\boldsymbol{F}_T$, an aerodynamic force $\boldsymbol{F}_A$ arising from the lift and drag from the airplane body, and the gravitational force from the earth $\boldsymbol{F}_G$. With the mass m,

$$\frac{d}{dt}\left(m\boldsymbol{v}_b\right) = \sum \boldsymbol{F} = \boldsymbol{F}_T + \boldsymbol{F}_A + \boldsymbol{F}_G \tag{B.1}$$

This equation is expressed in an inertial frame (earth centred system) and the derivative reads,

$$m\dot{\boldsymbol{v}_b} + \boldsymbol{\omega} \times m\boldsymbol{v}_b = \boldsymbol{F}_T + \boldsymbol{F}_A + \boldsymbol{F}_G. \tag{B.2}$$

Relating the gravity to each of the three body axes and assuming that the thrust is present only in the x-axis, the engine is aligned with the body x-axis such that the thrust force only affects the first equation,

$$\begin{aligned} m\dot{u} &= m(rv - qw) + F_{Ax} - mg\sin(\theta) + F_T \\ m\dot{v} &= m(pw - ru) + F_{Ay} + mg\cos(\theta)\sin(\phi) \\ m\dot{w} &= m(qu - pv) + F_{Az} + mg\cos(\theta)\cos(\phi) \end{aligned} \tag{B.3}$$

Moments

The airplane is affected by two moments: The aerodynamic moment $\boldsymbol{M}_A$ and the thrust moment $\boldsymbol{M}_T$. With airplanes inertia denoted $\boldsymbol{J}$,

$$\frac{d}{dt}\left(\boldsymbol{J}\boldsymbol{\omega}\right) = \sum \boldsymbol{M} = \boldsymbol{M}_T + \boldsymbol{M}_A \tag{B.4}$$

hence,

$$\boldsymbol{J}\dot{\boldsymbol{\omega}} + \boldsymbol{\omega} \times \boldsymbol{J}\boldsymbol{\omega} = \boldsymbol{M}_T + \boldsymbol{M}_A. \tag{B.5}$$

This results in the three familiar moment equations,

$$\begin{aligned} \dot{p}J_x - \dot{r}J_{xz} &= M_x - qr(J_z - J_y) + qpJ_{xz} \\ \dot{q}J_y &= M_y - pr(J_x - J_z) - (p^2 - r^2)J_{xz} \\ \dot{r}J_z - \dot{p}J_{xz} &= M_z - pq(J_y - J_x) - qrJ_{xz} \end{aligned} \tag{B.6}$$

where M_x, M_y and M_z contains both the aerodynamic and the thrust related moments, about each of the axis.

Introducing control surface actions in the above equations is usually done by introducing a number of control surface coefficients. These are made non-dimensional with respect to airplane characteristic like wing surface area, wingspan and the dynamic pressure of the surrounding air. If a thorough model of the airplane was identified it would be possible to create residuals for diagnosis based on structural analysis (see e.g. [19] and example in [50]) from such set of nonlinear equations of motion. The major obstacle with this approach is, however, that the model in this level of detail is not be easily achievable. Furthermore, the airplane's housekeeping telemetry, which is sent over a radio link with limited capacity, has a comparatively low sampling rate, and the fast dynamics of the model is not captured in the rate gyro and accelerometer information that is transmitted.

An alternative approach is to use real-time data to estimate simpler input-output relations and subsequently, with a bootstrapping procedure, also use these for diagnosis. This simpler model does not rely on accurate knowledge about the aerodynamics can be found based on the information actually present in the telemetry signals.

Figure B.2 illustrates the relations directly influenced by control surface actions on the particular UAV.

In classical airplane control, it is a common approximation to separate lateral from longitudinal states of the aircraft. Following this, transfer functions containing the signals of interest are straight forward to set up and identify. Figure B.2 shows those of interest to actuator faults. The associated linear transfer functions are defined as,

$$p(s) = H_{pa}(s)\delta_a(s) \tag{B.7}$$

$$r(s) = H_{ra}(s)\delta_a(s) \tag{B.8}$$

$$q(s) = H_{pa}(s)\delta_e(s) \tag{B.9}$$

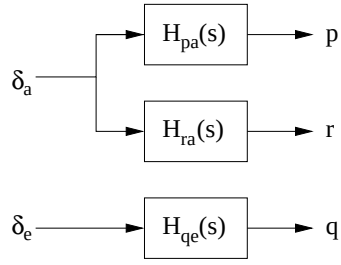

Figure B.2: Transfer functions between control inputs and rates.

Using this setup, another redundancy arises when exploring that δ_a affects both of p and r,

$$\begin{aligned} p(s) &= H_{pa}(s)H_{ra}^{-1}(s)r(s) \\ &= H_{pr}(s)r(s). \end{aligned} \tag{B.10}$$

The relations in Equations B.7 to B.10 are used for diagnostic tests and subsequent fault detection and isolation. It is noted that the transfer function in Equation B.10 can be identified directly from the rate signals r and p such that the transfer function H_{pr} need not be calculated from the ratio between H_{pa} and H_{ra}, but that this identification provides a separate consistency check on identification accuracy.

B.4 Residual Generator Estimation

When the relations illustrated in Figure B.2 are to be used for diagnosis, identification the transfer functions is needed.
One approach to signal-based transfer function estimation is to use the frequency domain, i.e. obtain transfer functions from power and cross spectra of the signals and use spectral techniques to determine the confidence of the estimate in various regions of frequency and over time. The latter is an essential part of model identification since flight patterns follow the control surface demands, and sufficient excitation is crucial for the quality of identification. Signal to noise relation is another concern that is handled by the spectral approach.
A transfer function $H_{yx}(s)$ between input x to output y, relates cross spectrum G_{yx} to power spectrum G_{xx} such that ideally, with no sensor or process noise,

$$G_{yx}(\varpi) = H_{yx}(\varpi)G_x(\varpi), \tag{B.11}$$

and H_{yx} would be estimated by,

$$\hat{H}_{yx}(\varpi) = \frac{G_{yx}(\varpi)}{G_x(\varpi)}. \tag{B.12}$$

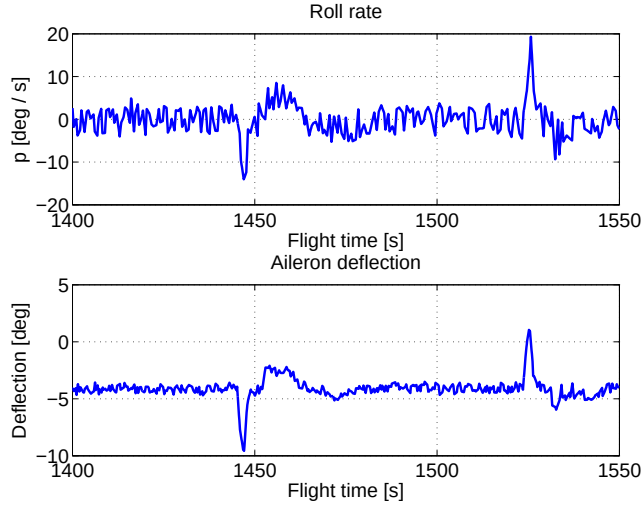

Figure B.3: Correlation between the given aileron deflection and the measured roll rate of the airplane in the fault free case. The aileron deflection of $-4°$ is to counteract the engines torque.

Figure B.3 shows an example of housekeeping telemetry data. Roll rate and aileron deflection are plotted for a period of time where a left and right turn manoeuvres are executed. A clear correlation is seen but the figure also reveals that significant noise is present on the data. Since an accurate estimate of the transfer function is essential for the subsequent diagnosis, signal noise need to be dealt with.
Quantifying the amount of noise requires calculation of a coherence function γ^2_{xy},

$$\gamma^2_{yx}(\varpi) = \frac{|G_{yx}(\varpi)|^2}{G_x(\varpi)G_y(\varpi)} \quad ; \quad \gamma^2_{yx} \in [0;1] \tag{B.13}$$

If measurements of the signals are corrupted by two uncorrelated noise sources m_x and m_y, as illustrated in Figure B.4, measured spectral densities are,

$$G_x(\varpi) = G_{xr}(\varpi) + G_{m_x}(\varpi) \tag{B.14}$$
$$G_y(\varpi) = G_{yr}(\varpi) + G_{m_y}(\varpi) \tag{B.15}$$
$$G_{yx}(\varpi) = G_{yrxr}(\varpi) \tag{B.16}$$

This gives a measured coherence,

$$\gamma^2_{yx}(\varpi) = \frac{|G_{yx}(\varpi)|^2}{\left(G_{xr}(\varpi) + G_{m_x}(\varpi)\right)\left(G_y(\varpi) + G_{m_y}(\varpi)\right)} \tag{B.17}$$

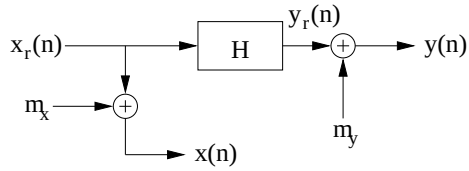

Figure B.4: System with noise on measurements.

Equation B.17 shows that $\gamma^2_{xy}(\varpi) < \gamma^2_{xryr}(\varpi)$, in particular for the frequencies where the signal to noise ratio is poor. This is used to identify the frequencies where the noise corrupts the signal, hence determining the range of frequencies that can be used for transfer function estimation and hence for creating the residuals.
Figure B.5 shows a plot of two typical coherence spectra. The solid (blue) curve is a time sequence where the low frequency part of the transfer functions can be used as coherence is close to 1, the dashed line (red) shows that no part of the spectrum is useful for estimation. In the case of the solid curve an estimate

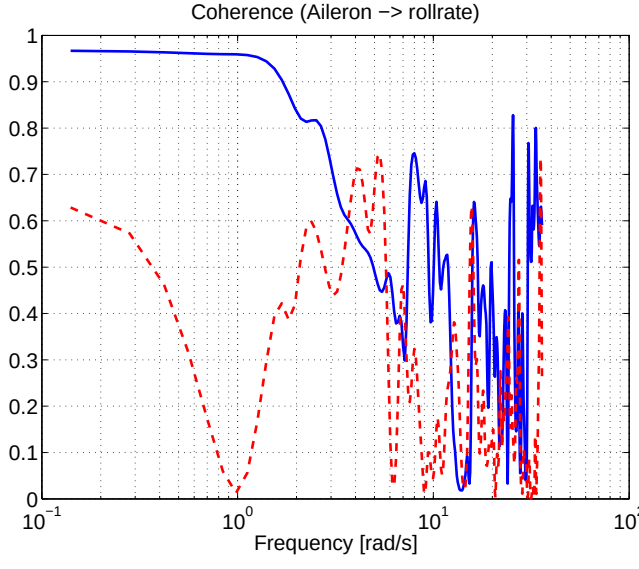

Figure B.5: Coherence of the aileron to roll rate relation for two samples of data from the Banshee. The blue solid curve represents a time-slot that is useable in the transfer function estimation, the red dashed curve shows a time-slot dominated by noise.

could be formed using equation B.12, for frequencies below 3 rad/s. In the case

Table B.1: Dependency matrix

	p	q	r	δ_a	δ_e
R_{pa}	1	0	0	1	0
R_{ra}	0	0	1	1	0
R_{qe}	0	1	0	0	1
R_{pr}	1	0	1	0	0
dect-,isolable	i	d	i	i	d

of the dashed curve the estimate is dominated by noise and need be discarded. The residual signal, used for evaluation, can then be created from the estimated dynamic function $\hat{H}$ between the given input and the output measurements. This gives rise to the following residuals based on equations B.7-B.10

$$R_{pa} = p - \hat{H}_{pa}\delta_a \tag{B.18}$$
$$R_{ra} = r - \hat{H}_{ra}\delta_a \tag{B.19}$$
$$R_{qe} = q - \hat{H}_{qe}\delta_e \tag{B.20}$$
$$R_{pr} = p - \hat{H}_{pa}\hat{H}_{ra}^{-1}r \tag{B.21}$$

This gives rise to the following incidence matrix
The Table shows that faults on p, r and δ_a are isolable, but faults on q and δ_e are only detectable. This could be remedied is an independent measurement of pitch angle was present.
An estimate of $\hat{H}$ using equation B.12 is illustrated in Figure B.6 for the Banshee UAV. This Figure shows the aileron to roll rate relation. Only the frequencies corresponding to a coherence close to 1 are used. In Figure B.6, these are to the left side of the vertical line. It is apparent, that only low-frequency range of the estimate can be used since noise dominates signal at higher frequencies.

Estimator conditions

Because of the adaptive way residuals are generated, a wrong model would adapted to if an error occurred and the estimator was running continuously. To address this, the estimation is stopped as soon as a deviation from normal is indicated by the change detector. Further, to avoid misdetection in the beginning of the flight, the estimated transfer functions are initialised with values from fault free flights.

B.5 Fault Detection

The fault detection is basically dealing with detecting an abrupt change in the residuals which drives them away from their zero value. As described in [19]

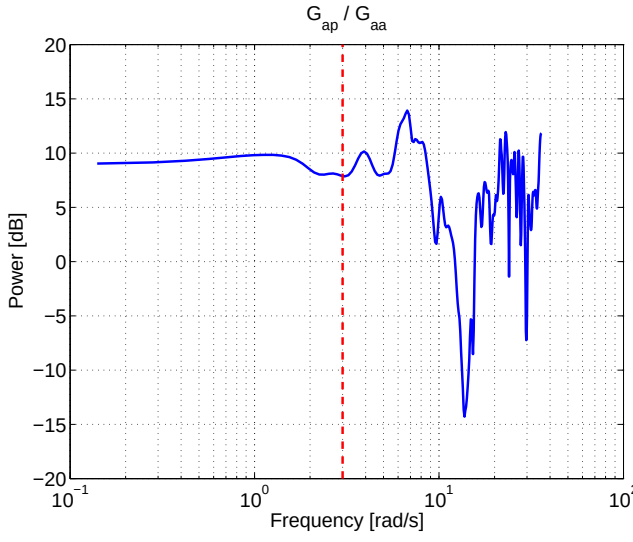

Figure B.6: The aileron to roll rate cross spectrum divided by the aileron power spectrum. The vertical red dashed line indicates the highest frequency useable according to the coherence.

several ways of creating residuals exists however the ones found above proves to be sufficient for the purpose of control surface failure diagnosis. Statistical change detection is used to diagnose changes in the residuals. Two hypotheses is used to test whether the each residual indicates nominal behaviour or whether a fault has occurred. In the vocabulary of statistical change detection the scenario that is analysed is the following: Detect an unknown DC-level in Gaussian white noise. If the signal is denoted x we wish to distinguish between the following two hypotheses:

$$\begin{aligned} \mathcal{H}_0 : x[n] &= w[n] \\ \mathcal{H}_1 : x[n] &= D + w[n] \end{aligned} \tag{B.22}$$

Both the constant level D and the variance of the noise σ_w^2 are unknown quantities which is estimated. The GLRT (Generalised Likelihood Ratio Test) for a linear model formulation can be used to test which of the hypotheses in B.22 is most likely. If the noise w is iid (independent and identically distributed) samples, the GLRT detector is

$$L_G(\boldsymbol{x}) = \frac{p\left(\boldsymbol{x}; \hat{\boldsymbol{\Theta}}_1\right)}{p\left(\boldsymbol{x}; \hat{\boldsymbol{\Theta}}_0\right)} > \gamma \tag{B.23}$$

If the ratio is larger than the threshold γ this decides $\mathcal{H}_1$ is true. $\hat{\boldsymbol{\Theta}}_i$ is the maximum likelihood estimate (MLE) of the parameters when hypothesis $\mathcal{H}_i$ is true.
In [77] the likelihood ratio for a general linear model is derived. With the linear model given by $\boldsymbol{x} = \boldsymbol{H\Theta} + \boldsymbol{w}$, the general expression for the two hypotheses are,

$$\begin{aligned} \mathcal{H}_0 : \boldsymbol{A\Theta} &= \boldsymbol{b}, \quad \sigma_w > 0 \\ \mathcal{H}_1 : \boldsymbol{A\Theta} &\neq \boldsymbol{b}, \quad \sigma_w > 0 \end{aligned} \tag{B.24}$$

Using as test quantity $T(\boldsymbol{x}) = \ln(L_G(\boldsymbol{x}))$, the standard result is ([77]),

$$T(\boldsymbol{x}) = \\ (N-1)\,\frac{\left(\boldsymbol{A}\hat{\boldsymbol{\Theta}}_1 - \boldsymbol{b}\right)^{\mathrm{T}} \left(\boldsymbol{A}(\boldsymbol{H}^{\mathrm{T}}\boldsymbol{H})^{-1}\boldsymbol{A}^{\mathrm{T}}\right)^{-1} \left(\boldsymbol{A}\hat{\boldsymbol{\Theta}}_1 - \boldsymbol{b}\right)}{\boldsymbol{x}^{\mathrm{T}}\left(\boldsymbol{I} - \boldsymbol{H}(\boldsymbol{H}^{\mathrm{T}}\boldsymbol{H})^{-1}\boldsymbol{H}^{\mathrm{T}}\right)\boldsymbol{x}} \tag{B.25}$$

and the estimate of the noise variance is given by

$$\hat{\sigma}_w^2 = \frac{1}{N-1}\boldsymbol{x}^{\top}\left(\boldsymbol{I} - \boldsymbol{H}\left(\boldsymbol{H}^{\top}\boldsymbol{H}\right)^{-1}\boldsymbol{H}^{\top}\right)\boldsymbol{x} \tag{B.26}$$

The specific problem, we wish to solve, given by equation B.22, can be transformed to this general formulation by choosing $\boldsymbol{\Theta} = [D]$, $\boldsymbol{A} = [1]$ and $\boldsymbol{b} = [0]$. The matrix $\boldsymbol{H}$ is a column of ones of dimension N, the window size.
Inserting the values of $\boldsymbol{A}$, $\boldsymbol{b}$, $\boldsymbol{H}$ and $\hat{\boldsymbol{\Theta}}_1$ in B.25 gives

$$T(\boldsymbol{x}) = (N-1)\frac{\bar{x}^2}{\hat{\sigma}_w^2} \tag{B.27}$$

Where $\bar{x}$ is the sample mean and the MLE of the variance stated in equation B.26 equals the variance of the test data,

$$\hat{\sigma}_w^2 = \frac{1}{N-1}\sum_{n=1}^{N}(x[n] - \bar{x})^2 \tag{B.28}$$

The test statistic is therefore [77],

$$T(\boldsymbol{x}) = (N-1)\,\frac{\bar{x}^2}{\hat{\sigma}_{\boldsymbol{x}}^2} > \gamma' \tag{B.29}$$

The threshold γ is found by maximising the detection probability and at the same time minimise the false alarm probability. Expressions for these probabilities are elaborated in [77].
To verify that the signal actually behaves as expected, the residual signal for the aileron is shown for a fault free (Figure B.7) and a faulty case (Figure B.8).

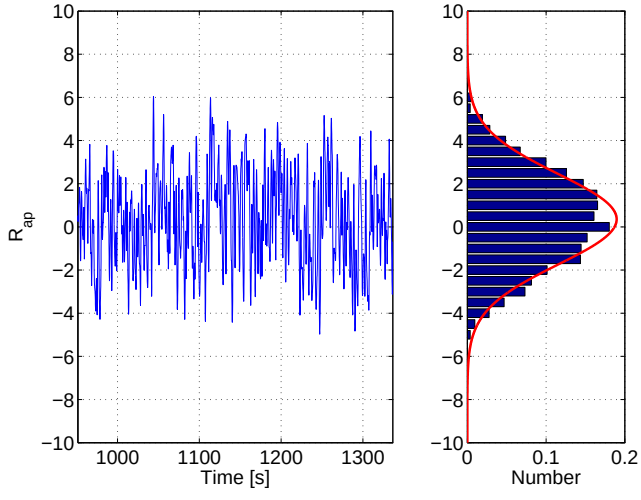

Figure B.7: Segment of the residual development over time with histogram.

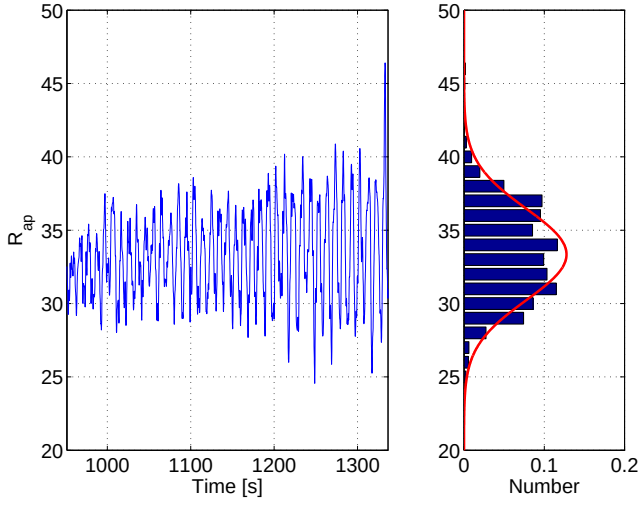

Figure B.8: Segment of the residual development over time with histogram in the faulty case.

As seen in the two figures the signal experiences a change in level. The signal in the fault free case has a satisfactory Gaussian fit, in the faulty case it is shifted and is only approximately Gaussian. This difference is detectable by the GLRT.

In order to have a sufficient data foundation to detect, a buffer size of $N = 100$ samples is used in the hypothesis test. With the used sample rate this buffer can be filled in approximately 8 seconds.

B.6 Results

In order to verify that the suggested methods work in reality they are tested using telemetry recordings of two different flights. First recordings from a standard mission of 70 minutes length is analysed with no faults present at the airplane. Then a telemetry recording of an incident where a UAV looses control over an aileron at launch. The plane manages to stay in the air for about 20 minutes before the operator commands the UAV to do a sharp right turn. This exceeds the reduced flight envelope and the plane tips over and is lost.

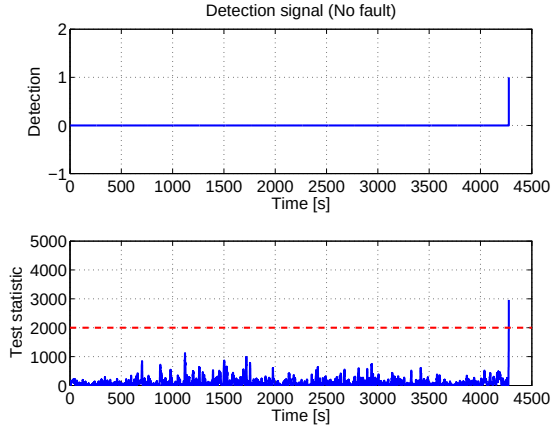

Figure B.9: The top plot shows the fault detection signal, which is 1 when a fault is diagnosed and otherwise 0. The bottom plot shows the development of the test statistic and the red dashed line indicates the decision threshold. The data is from a fault free flight.

Figure B.9 shows development over time of the decision signal for a residual of the form (B.18) together with the test statistic (equation B.29). The decision threshold γ is indicated by the dashed line. If this line is crossed an alarm is raised. The figure shows the signals development for a fault free flight. As seen in the figure only one false alarm is given in the 70 minutes of flight. This happens in the recovery phase just before the parachute is deployed and power to the UAV is cut. The airplane stalls on one wing which means the estimated relationship between aileron and roll rate no longer is satisfied.
Figure B.10 shows the same information as figure B.9 but for the faulty airplane. As seen on the figure an alarm is raised after 15 seconds of flight indicating a

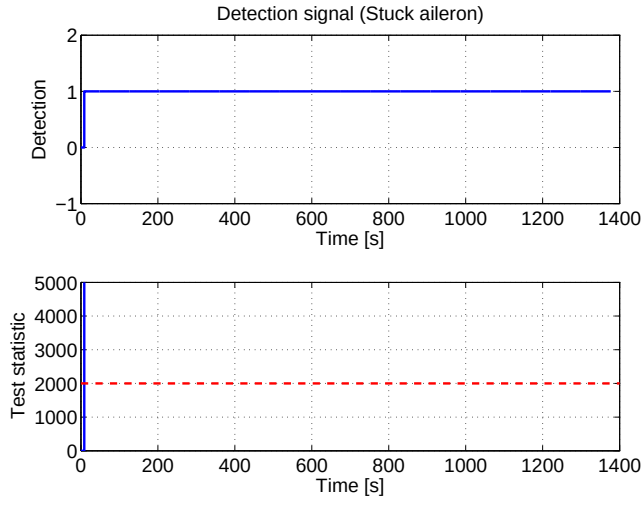

Figure B.10: The top plot shows the fault detection signal, which is 1 when a fault is diagnosed and otherwise 0. The bottom plot shows the development of the test statistic during the flight. Both signals are based on telemetry records from an UAV with a fault on one aileron.

fault. At this point the residual estimation is stopped in order to avoid adapting to an erroneous model. Since the aileron fails in the launch moment the detection of a fault is correct.

B.7 Conclusions

With the aim of finding diagnostic methods that do not rely on prior modelling, it was shown how diagnosis of faulty behaviour of UAV control surfaces could be achieved by applying spectral methods to different combinations of input and output signals from an UAV. Estimation of spectral coherence was employed to quantify slots in time and frequency where signals dominated by noise were sufficient to obtain model estimates for diagnosis. Generalised likelihood ratio tests were shown to be efficient to detect abrupt changes in the spectral estimates and uniquely indicate physical defects on the plane.
The method was tested on two datasets from Banshee UAV flights. One dataset contained no faults, the other was a case of a failure in one of the control surfaces. The method showed to be efficient in detecting what was after the flight found to be a physical issue with a control surface. The suggested methodology is simple to apply, it has no need for prior modelling and it is applicable for in-air diagnosis via telemetry to ground. Use of these results could enhance safety of autonomous UAV missions.

Paper C

Contingency Estimation of States for Unmanned Aerial Vehicle using a Spherical Simplex Unscented Filter[1]

Tobias Hahn, Søren Hansen and Mogens Blanke

Abstract

Aiming at survival from contingency situations for unmanned aerial vehicles, a square root spherical simplex unscented Kalman filter is applied for state and parameter estimation and a rough model is used for state prediction when essential measurements are lost. Processing real flight data, received by telemetry at quite low sampling rate, the paper shows that filter performance of reasonable quality can be achieved despite the low sampling rate and the result is a low order model that can be useful during contingency operation. It is shown that the filter-estimator approach can cope with the low rate measurements requiring very little system knowledge and very limited tuning efforts. A generic aircraft model is utilised as process model where the non dimensional coefficients are identified online with joint estimation of states. Numerical stability is guaranteed by mathematically efficient square root implementation of the filter algorithm. A case of loss of GPS signal demonstrates the use of the state estimates to obtain return of the UAV to close to it's home base where safe recovery is possible.

[1]In proceedings of 16th IFAC Symposium on System Identification, SYSID2012.

C.1 Introduction

Online estimation of the state and parameters of an aircraft has many applications. One is to enhance the safety and reliability by using estimates to replace sensor readings in case of sensor faults or signal artifacts. Position estimation after loss of GPS signal is a target of this work.

Several methods exist to do non-linear estimation. Most of these are based on extensions of the well-known Kalman filter like the Divided Difference filters [100] and the Unscented Kalman filter [74]. In this work the spherical simplex unscented filter is used. The spherical simplex unscented filter was developed in 2003 by Julier, it has been compared to it's alternatives [86] through applications to several practical problems [139] and it's advantages have been emphasised [137]. The loss of a GPS signal was also studied by [88], who employed non-linear observer techniques. However, other methods are needed when model information is absent except for the first principles relations.

This paper employs a spherical simplex unscented filter to the aircraft state estimation/parameter identification problem that is characterised by low-rate telemetry and a very slow sampling of on-board measurements. The paper demonstrates the benefits of this nonlinear filter-estimator for the difficult system set up at hand. The paper exploits telemetry data from a Banshee® drone (Meggitt Defense Systems Ltd), which is used as a target drone (see Fig. C.1). It weights around 90 kg and has a wingspan of 2.5 m. It is a delta wing aircraft with a pusher engine. The thrust is delivered by a Wankel engine equipped with a 2 bladed propeller. The Banshee is flying autonomously following a path of reference values including height, heading and airspeed, which are sent from a ground station that also receives and records telemetry.

By using the estimated aircraft model it is possible to substitute failing sensor values with corresponding estimates to enhance the safety and reliability of the UAV in case of contingency. If GPS signals experience drop-outs in air, safe recovery of the aircraft is very difficult. By using position estimates from a filter like the one suggested in this work, safe recovery might be possible. Since the estimates is based purely on the already available measurements, the added

Figure C.1: Banshee drone build by Meggitt Defense Systems.

safety comes without the cost of supplementary sensors on the UAV.
The paper is organised as follows. After detailing the system set-up, dynamic modelling is presented in a generic form. The version of a spherical simplex unscented filter algorithm that is useful for the models and low-rate data at hand is then presented and tuning is demonstrated. Results using flight data demonstrate performances in cases of normal and not-normal aircraft behaviour.

C.2 System Set-up

The Unmanned Aircraft System (UAS) considered in this paper sends sensor and actuator data from the aircraft to the ground station via a radio link. This telemetry data include measurements from the aircrafts inertial measurement unit (IMU), GPS receiver and commanded control surface deflections. With the limited channel capacity, the sample time between each data package is 0.0875 s, hence only a snap shot can be provided of the aircraft's fast dynamic motions. With channels required, a sampling time of 0.76 s results for each single sensor. With process time constants in the sub-second range, sampling makes it impossible to use a usual navigation algorithm for state estimation.
A further challenge is that an accurate aircraft model is not available. A model could be obtained by doing wind-tunnel experiments or by simulation in computational fluid dynamics software, however, this would restrict the method to a specific aircraft, which is not desirable. The only advantageous consequence of the data transmitting process is that the received sensor data have nearly independent increments.
The telemetry data comprise measurements of the orientation and angular rates from IMU and on-board processing, speed over ground, position and height from GPS data, and altitude derived from measurement of pressure. In addition, commands to control surfaces (aileron and elevator) are included in telemetry packages. Control surface demand origins from the on-board avionics control system.
The data processed as input for a dynamic model are the engine's rotational speed, the demand signals to elevator and aileron deflections. A challenge arising here is that these input signals have the same slowly sampled and noisy behaviour as the measurement data. Small corrections to the control deflections of aileron and elevator cannot be captured by the sampling. Applying zero order hold to the input signals would fall short in this context.

C.3 Filter algorithm

Sigma-point filters with at least second order accuracy can result in better performance than the extended Kalman-filter for many non-linear filter problems [126], but the computational load of the traditional sigma point filters that use $2n+1$ sigma-points (n is number of states) can become a real challenge for many

practical online applications. Since new variants of filters with reduced number of sigma-points have been developed, especially the ones stated by Julier and Uhlmann [76], the computational load could be reduced to come equal or below the load of the extended Kalman filter.

In each prediction step the process function (C.1) has to be evaluated for each single sigma-point. Therefore reducing the number of sigma-points directly reduces the computational load of the filter algorithm. It was shown by Julier [75] that doing so must not lead to a significant decrease of accuracy. In contrast to the traditional unscented approach a simplex based set of sigma-points is placed around the actual state estimation as non symmetric distribution, which is illustrated in Fig. C.2. Theses points match the mean and covariance of the state distribution with still at least second order [75]. We identified the spherical simplex approach as one of the most applicable advancements. Recent investigations [137, 139, 86] show it's practical relevance. [112] shows that the spherical simplex UKF (compared to UKF and EKF) has the best performance with respect to computational complexity and accuracy. Another beneficial property of sigma point filters is the reduced effort in implementing the dynamic model equations: since only a "black-box" model is required, there is no need to calculate derivatives of the model equations i. e. Jacobian or Hessian matrix. In addition, numerical stability of the filter algorithm can be guaranteed by efficient square-root implementation.

The square-root variant of the unscented Kalman filter with $n + 2$ spherical simplex sigma-points was decided for this research. This implementation meets all the above mentioned advantages over the extended Kalman filter.

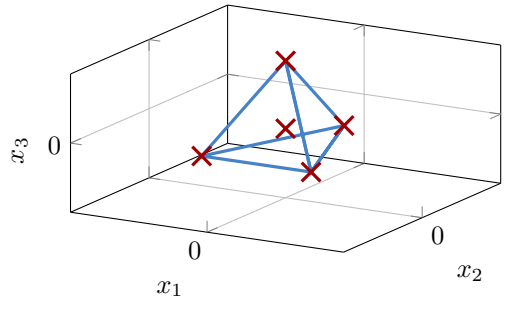

Figure C.2: Spherical simplex sigma-point selection scheme in case of three states.

C.4 Aircraft Generic Model

The generic behaviour of a low-speed aircraft is described by the following non-linear state space formulation

$$\dot{\vec{x}} = \begin{bmatrix} \dot{\vec{v}}_b \\ \dot{\vec{\omega}}_b \\ \dot{\vec{\Phi}}_e \\ \dot{\vec{P}}_e \end{bmatrix} = \begin{bmatrix} \frac{1}{m}\vec{F}_b + \vec{v}_b \times \vec{\omega}_b \\ \boldsymbol{J}^{-1}\left(\vec{M}_b - \vec{\omega}_b \times \boldsymbol{J}\vec{w}_b\right) \\ \boldsymbol{R}_b^e \vec{\omega}_b \\ \boldsymbol{C}_b^e \vec{v}_b \end{bmatrix}, \tag{C.1}$$

where $\vec{v}$ is velocity, $\vec{\omega}$ is angular rate and $\dot{()}$ denotes it's time derivative. The origin of body axes b is at the centre of gravity, with positive x_b-axis pointing forward through the nose of the vehicle, positive y_b-axis out the right wing, and positive z_b-axis through the underside. The orientation of the vehicle is expressed in Euler's angles $\vec{\Phi}$. The matrices $\boldsymbol{R}_b^e$ and $\boldsymbol{C}_b^e$ transform the body fixed angular rate and velocity to an Earth fixed frame, see [80]. By integration, an earth fixed north-east-down position $\vec{P}_e$ and an earth fixed orientation $\boldsymbol{\Phi}_e$ is obtained, denoted by subscript e. The mass m and inertia $\boldsymbol{J}$ are known from simple laboratory tests. The force $\vec{F}$ and moment $\vec{M}$ are then modelled to capture essential dynamics.

C.4.1 Modelling forces and moments

The model has to have sufficient complexity to be able to predict values between the measurements, but since the parameters have to be estimated from the same measurements, as few parameters as possible should be included to meet the requirements of the identifiability ([129]). Further, an appropriate model structure has to be chosen such that the parameters are sensitive to the inputs during the flight patterns used, to achieve identifiability. Since we do not need accurate simulation of the aircraft but rather just predict a few seconds ahead in time, the parameters are allowed to vary over different flight patterns. Hence, the model has to be valid only around the current operating point.

C.4.2 Sum of forces

To meet the considerations stated above, only the most influential forces and moments acting on the aircraft are modelled:

$$\vec{F}_b = \vec{F}_{b,T} + \vec{F}_{b,A} + \vec{F}_{b,\mathrm{G}} \tag{C.2}$$

$$\vec{M}_b = \vec{M}_{b,A}. \tag{C.3}$$

Here, thrust from the propeller is $\vec{F}_T$. The gravity from Earth is $\vec{F}_\mathrm{G}$, the aerodynamic force $\vec{F}_A$ and moment $\vec{M}_A$. The latter have components giving lift, drag and side force as well as roll, pitch and yaw moments.

C.4.3 Thrust from propeller

Since the pusher propeller is mounted aligned with the fuselage, the generated thrust is assumed to act on the centre of gravity of the aircraft.
In the current operating point, the thrust is assumed to be proportional to the angular rate of the propeller

$$\vec{F}_{b,T} = \begin{bmatrix} K_{T\delta}\delta_T & 0 & 0 \end{bmatrix}^T \tag{C.4}$$

$$\vec{M}_{b,T} = \vec{0} \tag{C.5}$$

where δ is control input to the propeller and $K_{T\delta}$ is identified by the filter.

C.4.4 Force of gravity

The force of gravity is given by

$$\vec{F}_{b,G} = \mathbf{C}_e^b \cdot \vec{F}_{e,G} \quad \text{with} \quad \vec{F}_{e,G} = \begin{bmatrix} 0 \\ 0 \\ mg \end{bmatrix} \tag{C.6}$$

where g is the gravitational acceleration that points towards the center of the earth. Thus, it is aligned with the z-component in earth axes. In body axes, the force of gravity can be found by means of a product of the transformation matrix $\mathbf{C}_e^b$, see [80].

C.4.5 Aerodynamic force

The aerodynamic force caused by the wings and the fuselage is split into three components defined by the axes of the wind fixed frame, denoted by subscript w. The origin of wind axes is at the vehicle's centre of gravity, with positive x_w-axis forward and aligned with the air-relative velocity vector, positive y_w-axis out the right side of the vehicle, and positive z_w-axis through the underside in the x_b-z_b-plane in body axes. To insert the aerodynamic force in (C.2) it has to be transformed to the body fixed frame by

$$\vec{F}_{b,A} = \mathbf{C}_w^b \cdot \vec{F}_{w,A}. \tag{C.7}$$

where

$$\mathbf{C}_w^b = \begin{bmatrix} \cos\alpha \cdot \cos\beta & -\cos\alpha \cdot \sin\beta & -\sin\alpha \\ \sin\beta & \cos\beta & 0 \\ \sin\alpha \cdot \cos\beta & -\sin\alpha \cdot \sin\beta & \cos\alpha \end{bmatrix} \tag{C.8}$$

and

$$\alpha = \arctan\left(\frac{v_{z,b,f}}{v_{x,b,f}}\right) \tag{C.9}$$

$$\beta = \arcsin\left(\frac{v_{y,b,f}}{|v_{b,f}|}\right). \tag{C.10}$$

Taking into account the absolute wind speed, given in the Earth fixed frame as $\vec{v}_{e,wind}$, it interacts with the movement of the vehicle in the following way

$$\vec{v}_{b,f} = \vec{v}_b - \mathbf{C}_e^b \, \vec{v}_{e,wind}. \tag{C.11}$$

Since the wind speed is not known, it is estimated by the filter.
The aerodynamic model equations are then expressed in vector form as

$$\vec{F}_{w,Aero} = \begin{bmatrix} -C_D \\ C_S \\ -C_L \end{bmatrix} \cdot \frac{1}{2} \rho A \cdot |\vec{v}_{b,f}|^2 \tag{C.12}$$

$$\vec{M}_{w,Aero} = \begin{bmatrix} bC_R \\ \bar{c}C_P \\ bC_Y \end{bmatrix} \cdot \frac{1}{2} \rho A \cdot |\vec{v}_{b,f}|^2 \tag{C.13}$$

where ρ is the air density, A is the wing surface area, $\vec{v}_{b,f}$ is the air-relative velocity, b is the wing span, and $\bar{c}$ is the mean aerodynamic chord of the wing. The aerodynamic moments are normalised with respect to the parameters of the vehicle.
The aerodynamic forces and moments result from the relative motion of the air and the vehicle. They can be expressed in terms of the non-dimensional drag coefficient C_D, side force coefficient C_S, lift coefficient C_L, roll moment coefficient C_R, pitch moment coefficient C_P, and yaw moment coefficient C_Y.
To design a model structure, these aerodynamic coefficients have to be characterised as functions of non-dimensional quantities that depend on the states of the vehicle.
By employing model reduction the following coefficients are suggested.

$$C_D = K_{D0} + K_{D\alpha}\alpha + K_{Dv} |\vec{v}_b| \tag{C.14}$$

$$C_S = K_{S0} + K_{S\beta}\beta \tag{C.15}$$

$$C_L = K_{L0} + K_{L\alpha}\alpha + K_{Lv} |\vec{v}_b| \tag{C.16}$$

$$C_R = K_{R0} + K_{L\delta_{ail}}\delta_{ail} + K_{R\omega}\omega_{x,b} + K_{R\beta}\beta \tag{C.17}$$

$$C_P = K_{P0} + K_{P\delta_{elev}}\delta_{elev} + K_{P\omega}\omega_{y,b} + K_{P\alpha}\alpha \tag{C.18}$$

$$C_Y = K_{Y0} + K_{Y\beta}\beta + K_{Y\omega}\omega_{x,b}\alpha \tag{C.19}$$

where α is the angle of attack, δ a control input and all K are parameters that will be estimated by the filter.
As mentioned in introduction, applying zero order hold to the sampled input signals lead to a residual that has to be compensated mostly by the parameters $K_{(\cdot)\delta}$ as well as $K_{(\cdot)0}$. Therefore, a higher variation than usual need be allowed on these parameters. This is further elaborated in sec. C.4.6.

Further simplifications

Since the parameters $K_{(\cdot)}$ are not fixed but rather identified online by the filter, they could be allowed to change over different flight patterns and may be used

to apply corrections to the estimation of the state. Assuming that we don't want the parameters to converge to fixed values, some parameters of the above stated model may be ejected or set to fixed values.

C.4.6 Parameter estimation

The investigated drone does not show much change in the flight pattern over the complete mission since the input to the aircraft is limited because it is strictly controlled by a conservatively adjusted autopilot. Hence an identification approach with constant forgetting is applied.
Adaptive methods may improve the identification only in case of strongly changing flight conditions, e.g. steady state flight for a long time and then a rapid manoeuvre.
The above stated model parameters $K_{(\cdot)}$ are modelled as random walk, driven by noise $\vec{\nu}$, which is adjusted by the filter to make the prediction fit the measurements. Therefore, the state vector and also the covariance matrix of the filter are augmented by one additional state $\dot{K}_{(\cdot)} = \nu_{(\cdot)}$ for each parameter. Concatenation leads to

$$\begin{bmatrix} \dot{\vec{x}} \\ \dot{\vec{K}} \end{bmatrix} = \begin{bmatrix} \vec{f}\left(\vec{x}, \vec{u}, \vec{K}\right) \\ 0 \end{bmatrix} + \begin{bmatrix} 0 \\ \vec{\nu} \end{bmatrix} \tag{C.20}$$

so seen from the filter's point of view, there is no difference between the parameters and the states. Furthermore, this formulation corresponds to the filter-problem, the square-root-spherical-simplex-unscented-filter can deal with.
While the forces and moments acting on the aircraft are modelled as stochastic processes, the process covariances of velocity, angular rate, orientation and position are set to zero which results in absolutely consistent kinematics of the state estimation. The filtering process then shows a behaviour that can be interpreted as shown in Fig. C.3.

Evaluation of covariance of process noise

The covariance of process noise $\begin{bmatrix} 0 & \vec{\nu} \end{bmatrix}^T$ in (C.20) is usually denoted as $\boldsymbol{Q}$ in Kalman-Filter equation. By adjusting up to 19 elements of $\boldsymbol{Q}$ corresponding to the parameters in (C.14)...(C.19) the filter is tuned to enhance its performance. Therefore the algorithm is executed with initial postulation of covariance matrix $\boldsymbol{Q}$ utilizing some prior knowledge about the behaviour of the UAV. With offline processing different sets of measurements this way, information is gathered i.e. the individual range of each single parameter and the typical parameters rate of drift while changing flight pattern. Based on this knowledge, the aerodynamic parameters are initialised and the random walk is parametrised to model the drift of the aerodynamic parameters. Doing so already leads to suitable filter performance. Further tuning is done by again offline processing and adjustment of the process covariance by some experience as well as try an error.

C.4.7 Measurement model

The measurements used in the filter is comprised of the following signals:

$$\vec{y} = \begin{bmatrix} \dot{\vec{v}}_b^T & \vec{\omega}_b^T & \vec{P}_e^T & \vec{\Phi}_e^T & \sqrt{v_{x,e}^2 + v_{y,e}^2} \end{bmatrix}^T. \tag{C.21}$$

These corresponds to what is available from the telemetry data sent from the UAV.

C.5 Results

The state and parameter estimation was applied to flight data from the Banshee drone. All of the aerodynamic force and moment coefficients were identified online in joint estimation with the states.

C.5.1 Interpretation of Results

Comparing the estimated motion with the measured motion shows that the filter algorithm works as expected. This is illustrated for yaw rate in Fig. C.4.
Comparing our results with [36] and [94] that are using extended Kalman filter and unscented filter we do not have the ability to achieve their extremely perfect identification performance. This may be due to high noise, low sample rate and corrupted input signals in our case of application.

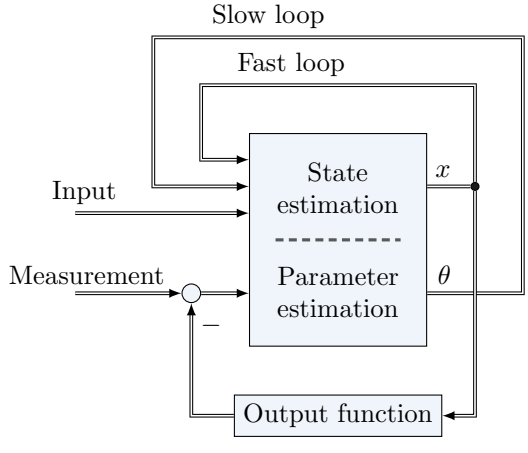

Figure C.3: Illustration of the most influential dependencies of the estimation approach. The parameters θ are cautiously adjusted while the states x can change rapidly.

For roll angle estimation (Fig. C.5) there is a small overshoot compared to the measurement. This occurs from the incorrect input that has to be compensated for by varying the model parameters, especially moment parameters due to roll, aileron deflection and roll damping.
Fig. C.6 shows that estimation of roll damping parameter is affected by excitation of the roll rate which can be seen by comparing with roll angel in Fig. C.5. When there is high excitation, the roll damping parameter is adjusted by the filter. When there is low excitation the parameter keeps around its value while its covariance i.e. the uncertainty of the identification increases. One solution to prevent the filter algorithm from behaving like this might be to use another approach than constant forgetting for parameter estimation with the goal: identification only in case of excitation.
The oscillation of standard deviation in the range of 100 s to 150 s is caused by an increased noise level of the gyro measuring the roll rate (Fig. C.7). This has a direct impact on the covariance of the roll damping parameter. The actual approach does not adapt to varying sensor noise.

C.5.2 Tuning the filter algorithm

The forgetting of the parameter identification, i. e. the parameter section of the covariances of process model need to be set with accuracy of about one order of magnitude to achieve good filter performance. This is experienced as an acceptable tuning effort.
To determine the appropriate model structure an off-line run of the filter was done initially. Here only one aerodynamic force and moment where estimated. That means the estimation of three components of force and the moment, in 6 degrees of freedom. Up to this step, no knowledge about the behaviour of the vehicle was taken into account, but doing so in next step improved the performance. Applying correlation analysis to the estimated parameters, model structure can be determined [80]. The aim is to arrive at a model structure, complex enough to perform the necessary prediction ahead in time, while still having parameters that are sensitive to the identification mechanism.

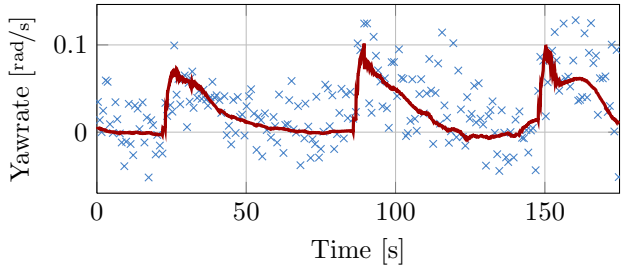

Figure C.4: Measurement and estimation of yaw rate.

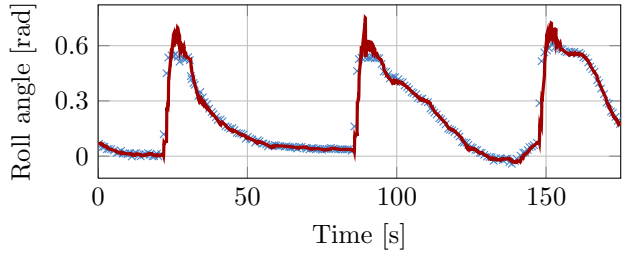

Figure C.5: Measurement and estimation of roll angle. The fit error is due to fairly unknown aileron input.

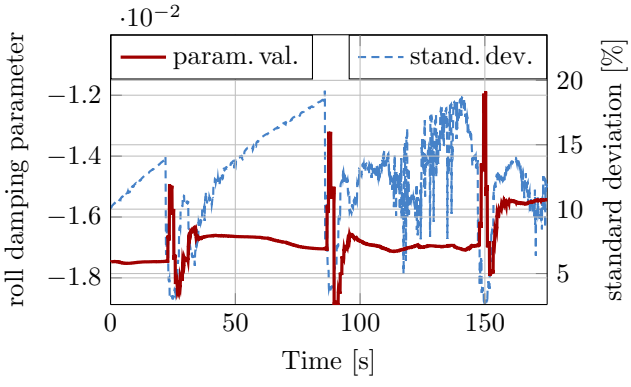

Figure C.6: Estimation of roll damping parameter. Standard deviation increases without roll excitation.

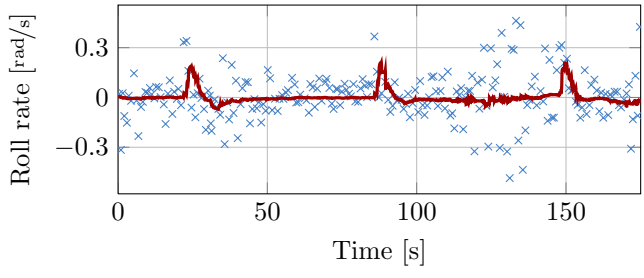

Figure C.7: Measurement and estimation of roll rate.

C.5.3 Identification results using simulated model

A simulated model of the UAV was also used to generate input data for the filter algorithms to verify convergence against a known model. Input sequences

to the model were the flight data control surface demands and propeller shaft speed. The result shows that some parameters converge to the expected values (Fig. C.8) while others are biased. The result depends on the number of identified parameters as well as on the actual input signal. In addition, there is a variation in the parameters since they are also used to correct the state estimation while the process covariance of state estimation is set to zero.

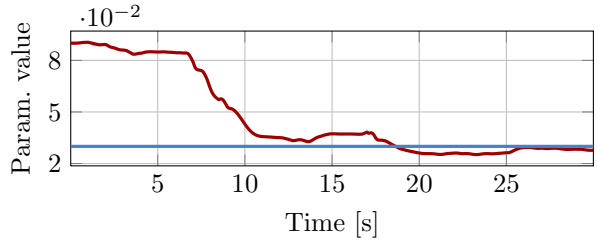

Figure C.8: Simulation of estimation of a parameter describing yaw moment generated by roll rate

C.5.4 GPS-fault case study

One obvious application of the aircraft state estimation is to use estimated values when real sensors fail. An example of this is the case of GPS dropout. Fig. C.9 shows a comparison between the real and the estimated flight path development in case of a GPS sensor dropout. This situation could easily lead to loss of the aircraft since the build-in way-point control system depends solely on GPS. The fail-to-safe reaction in this situation is to stop the engine and release the parachute so the drone will be brought safely down. However releasing the parachute when the drone is out of sight can in some situations be dangerous and the recovery will be quite difficult. If the landing position is within visible distance to the recovery team, the aircraft can be brought down safely. The results shown in Fig. C.9 would get the drone returning to the landing site with an estimated position error is about 600 m. This would suffice in clear sky conditions, but with reduced visibility, change in the return pattern would be needed to reduce the time of return and hence reduce the build-up of position error.

C.6 Conclusion

This paper analysed simplified model structures that were generic, with model parameters having a physical meaning for use in the low-rate sampled parameter identification and state estimation problem for the UAV. A Model was obtained that could carry information about the actual structure of the real process de-

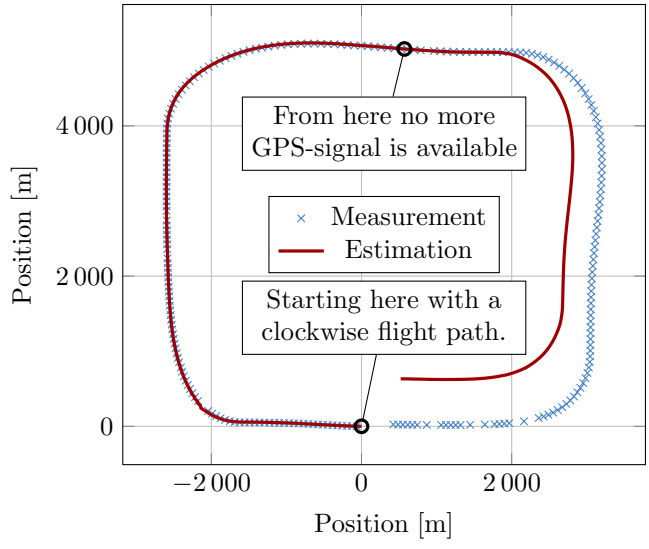

Figure C.9: Estimation of aircraft position in case of GPS sensor fault. From the shown position, no GPS-position and no GPS-speed is processed by the filter which leads to an increasing error in position estimation.

spite the low sampling rate. Developing a spherical simplex unscented filter and tuning it for this problem demonstrated its ability to cope with the difficult estimation problem at hand. Simulations showed which model structures were useful given the actual flight patterns. It was shown how estimation could be used for position prediction in case of a GPS measurement fault. Model based system diagnosis could be an obvious extension of the results.

Paper D

In-flight Fault Diagnosis for Autonomous Aircraft via Low-rate Telemetry Channel[1]

Søren Hansen and Mogens Blanke

Abstract

An in-flight diagnosis system that is able to detect faults on an unmanned aircraft using real-time telemetry data could provide operator assistance to warn about imminent risks due to faults. However, limited bandwidth of the air-ground radio-link makes diagnosis difficult. Loss of information about rapid dynamic changes and high parameter uncertainty are the main difficulties. This paper explores time-domain relations in received telemetry signals and uses knowledge of aircraft dynamics and the mechanics behind physical faults to obtain a set of grey-box models for diagnosis. Relating actuator fin deflections with angular rates of the aircraft, low order models are derived and parameters are estimated using system identification techniques. Change detection methods are applied to the prediction error of angular rate estimates and properties of the test statistics are determined. Techniques to overcome correlations in data and cope with non-Gaussian distributions are employed and threshold selection is obtained for the particular distributions of test statistics. Verification using real data showed that the diagnosis method is efficient and could have avoided incidents where faults led to loss of aircraft.

[1]In proceedings of 8th IFAC Symposium on Fault Detection, Supervision and Safety for Technical Processes, SAFEPROCESS2012.

D.1 Introduction

When operating small unmanned aerial vehicles (UAVs) robustness and fault-tolerance is important to ensure safe and trouble free flying. However the cheap materials and few redundancies used for UAVs are in contrast to this. Loss or partly loss of a control surface action is one problem that can happen easily but because of redundancies in the control actions the aircraft is some times able to continue flying within a reduced flight envelope. If it is possible to diagnose the fault and give a warning to the UAV operator he may be able to fly the aircraft home and the hazardous situation of a crash is avoided. It is therefore important to be able to diagnose these failures and alert the operator before the aircraft is lost.

Fault diagnosis and fault-tolerant control for aircrafts has been explored by several authors and has been subject to many different approaches [44]. A structural analysis approach to diagnosis was considered in [50] where additive faults were diagnosed on sensors and actuators. Diagnosis of degraded control surfaces were studied in [15], [13], [11] and [102] where active methods were used to isolate specific faults. Observer based fault diagnosis was investigated in e.g. [69] and nonlinear models that describe the aircraft can also be used in fault diagnosis, which was demonstrated on small helicopters in [51]. Model-free methods were also proposed for instance by [84], where use of the Mahalanobis distance has been utilised to diagnose deviations from normal behaviour in autonomous vehicles. The topic of fault diagnosis for aircrafts are not only of academic interest but is also important to the industry ([57]).

Diagnosis of loss or partial loss of a control surface is the subject in this paper. It is investigated how a relationship between inputs and measurements can be estimated and subsequently used for diagnosis of the faults, without detailed mathematical models. The relationship is based only on the telemetry data send from the aircraft to the ground station via a radio-link. The limited throughput of this link makes the use of detailed mathematical models hard which is why simple relations is used. A model relating the angular rates measured by the aircraft inertial navigation system (INS) to the deflections of control surfaces is adapted using recursive methods running online while the aircraft is flying. Changes to the adapted model indicates a change in the behaviour of the UAV and is considered a sign of a fault. The model changes is found by statistical change detection algorithms such as Cumulative Sums (CUSUM) and Generalised Likelihood Ratio Test (GLRT) approaches.

The paper is divided into seven sections. After the introduction a short description of the aircraft in use is given. After this a grey-box model for fault diagnosis is proposed. This leads to a chapter about signal processing and change detection of the residuals extracted from the model. After this results of using the diagnosis system on real life data is presented. Both data from faulty and non-faulty flights are shown. After this the perspective for the operator is discussed and a conclusion is given.

Figure D.1: Banshee drone ready for launch.

D.2 System Description

The UAV considered in this paper is a Banshee target drone build by the British company Meggitt Defense System. The system is primarily used for target practice, but also surveillance and reconnaissance is possible. It can be equipped with various payloads for triggering and measuring the performance of the weapon system in use. The Banshee drone is used by the military in over 30 countries [92].

The UAV is a delta wing aircraft equipped with a small rear mounted engine. The thrust is delivered by a 2 bladed wooden propeller. It is launched from a catapult system and lands by parachute. It is therefore not equipped with any sort of landing gear. The aircraft has an autopilot system and is operated from ground by an operator which commands the aircraft to fly between a number of waypoints.

D.2.1 Sensors and Actuators

The Banshee drone has two control surfaces on each wing. The outermost is working as an aileron controlling the roll of the aircraft, and the innermost, closest to the fuselage, is the elevator action. Signals to these are denoted δ_a and δ_e respectively. Each control surface is operated by a servo motor which is connected to the surface via a linkage system. Each pair of control surfaces are controlled as one so it is not possible to move the surfaces individually. There is also a servo operating the throttle of the engine which is denoted δ_T.
The Banshee is equipped with a barometric sensor which measures the flying height and a pitot tube to measure the airspeed. The onboard INS estimates the

attitude of the aircraft, based on measurements from INS sensors around the three body axes of the aircraft. Among those gyros measuring the roll- pitch- and yaw-rate (p, q and r) . Apart from these a standard GPS is onboard to get the position of the aircraft and correct the attitude estimate. All this telemetry data is send to ground from the aircraft using a radio link.

D.3 Model of Control Surface Faults

A descriptive model of an aircrafts behaviour is given by the standard 6 degree of freedom equations which outlines the kinematics and the dynamics working on the aircraft. In eg. [122] these equations are outlined for reference. The dynamics which is the most interesting part with regard to diagnosis of actuator faults, consists of Newtons equations that relates motion with forces and moments. These are what makes the aircraft move around in the desired way. The engine and propeller delivers the thrust and a moment acting on the aircraft. The force is assumed aligned with the body x-axis and the moment acts around this axis. Aerodynamic forces and moments are created by the aircraft's wings, body and control surfaces and are usually modelled by a set of non-dimensional coefficients relating each force and moment to a complex dependency on aircraft attitude and control surface deflection. To get a complete model wind-tunnel experiments or fluid dynamic simulations of the aircrafts wings and body must be carried out. Obtaining such a model is time consuming and it will not be fully utilised in this application, because of the limited dynamics visible on the telemetry data from the aircraft.

D.3.1 Model for Low-bandwidth Data

A simple relationship between control action and reaction of the aircraft is needed as an alternative. The immediate action seen on the aircraft when a control surface is deflected is on its angular rates. Therefore a correlation between these variables must exist. Fig. D.2 shows a typical plot of the correlation between aircraft roll rate and the aileron deflection. A straight line fit is also plotted in Fig. D.2. The aircraft is flying levelled wings most of the time so a large proportion of the data lie in the centre. Correlation is experienced only when the aircraft is turning. The correlation coefficient is 0.7 for the linear relation. This is sufficient for fault diagnosis.

D.3.2 Simplified Model for Diagnosis

As shown above an approximate linear relationship exist between the aileron input and roll rate. A similar relationship exists between the elevator and the aircrafts pitch rate. The yaw rate is affected each time the aircraft turns and therefore an integrating effect between that and the aileron input is proposed.

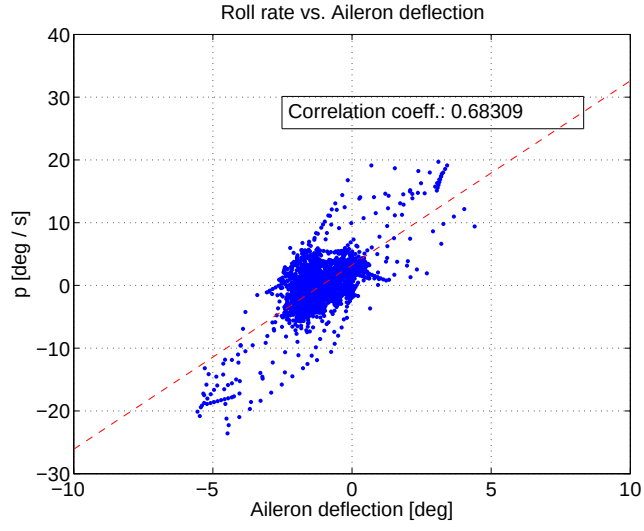

Figure D.2: Correlation between roll rate and aileron deflection.

This ends up with the following three relations for roll, pitch and yaw calculated at sample k.

$$p[k] = a_{pa}\delta_a[k] + b_{pa} \tag{D.1}$$
$$q[k] = a_{qe}\delta_e[k] + b_{qe} \tag{D.2}$$
$$r[k] = a_{ra}\delta_a[k] + b_{ra}r[k-1] + c_{ra} \tag{D.3}$$

where b_{pa}, b_{qe} and c_{ra} are bias terms and a_{pa}, a_{qe} and a_{ra} are gain factors. Equation D.3 includes the integrating effect between the aileron and yaw rate in the b_{ra} term.
Equations (D.1) to (D.3) can be described on the form

$$y[k] = \boldsymbol{\varphi}[k]^{\mathrm{T}}\boldsymbol{\Theta}[k] + e[k] \tag{D.4}$$

with $e[k]$ being the unmodelled behaviour. For (D.1) the parameters would be:

$$y[k] = p[k] \tag{D.5}$$
$$\boldsymbol{\varphi}[k] = \begin{bmatrix} \delta_a[k] \\ 1 \end{bmatrix} \tag{D.6}$$
$$\boldsymbol{\Theta}[k] = \begin{bmatrix} a_{pa} \\ b_{pa} \end{bmatrix} \tag{D.7}$$

From the general expression given by (D.4) the residuals can be formed as

$$\varepsilon[k] = y[k] - \boldsymbol{\varphi}[k]^{\mathrm{T}}\boldsymbol{\Theta}[k] \tag{D.8}$$

	p	q	r	δ_a	δ_e
R_{pa}	1	0	0	1	0
R_{qe}	0	1	0	0	1
R_{ra}	0	0	1	1	0

Table D.1: Fault dependencies of residuals. A 1 means that the residual is affected by the signal in question.

Lifting surface defects will give rise to rapid change in the input/output signals and hence in the prediction error (D.8) and subsequently appear as a parameter adaptation to the faulty case.
Three residuals are formed: R_{pa} from (D.1), R_{qe} from (D.2) and R_{ra} from (D.3). This gives rise to a binary dependency between residuals and actuator faults as shown in Table D.1.

D.3.3 Time domain estimate

A recursive least squares (RLS) algorithm is used to estimate the parameters of the relationships given by (D.1) to (D.3). Both the gain and the offset value is estimated such that a general relationship at sample k would be as (D.4).
The RLS algorithm used is listed below, for the general expression.

$$\varepsilon[k] = y[k] - \boldsymbol{\varphi}[k]^{\mathrm{T}}\hat{\boldsymbol{\Theta}}[k-1] \tag{D.9}$$

$$P[k] = \left(\lambda_f P[k-1]^{-1} + \boldsymbol{\varphi}[k]\boldsymbol{\varphi}[k]^{\mathrm{T}}\right)^{-1} \tag{D.10}$$

$$\hat{\boldsymbol{\Theta}}[k] = \hat{\boldsymbol{\Theta}}[k-1] + P[k]\boldsymbol{\varphi}[k]\boldsymbol{\varepsilon}[k] \tag{D.11}$$

Where λ_f is an exponential forgetting factor and $P[k]$ is the estimator covariance. $P[k]$ is initialised to a diagonal matrix with the variances of 0.1. This is the value the covariance settles at when running the algorithm over a time period.
Fault detection is then achieved by detecting abrupt changes to the residuals of the estimated parameters (D.9).

D.4 Model change detection

In order to detect changes in the parameters a test statistic is created. When this value exceeds a threshold γ an alarm is raised indicating that one of the relations in (D.1)-(D.3) is violated. Several test statistics are available [77], but in this paper the CUSUM and the GLRT is applied. The principle of combined model estimation and diagnosis is described in [61].

D.4.1 Residual whitening

By analysing the residuals power spectrum density and autocorrelation functions it is found that the a heavy correlation is present on the signals. This is illustrated for R_{pa} in the left plots of Fig. D.3. This correlation will degrade

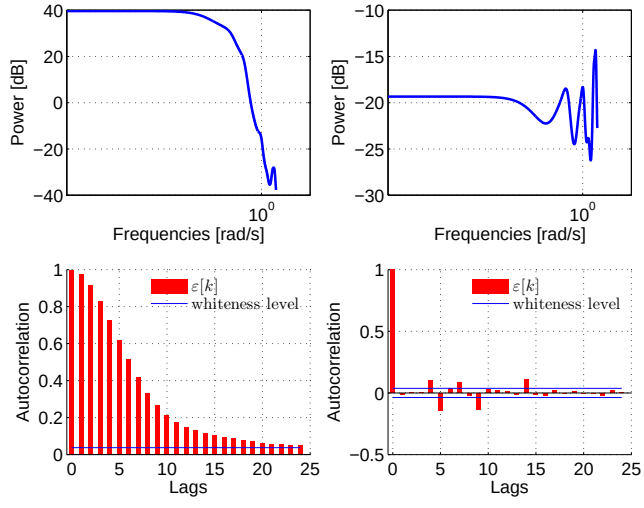

Figure D.3: Power spectrum density and autocorrelation of residual (equation D.1) before and after whitening.

the performance of the change detector and is therefore unwanted. Therefore the signals are run through a whitening filter before further processing. A finite impulse response (FIR) representation of a linear estimator can be used to estimate the deterministic part of the signal

$$\hat{\varepsilon}[k] = \sum_{j=1}^{J} a_j \varepsilon[k-j] \tag{D.12}$$

By subtracting the estimate $\hat{\varepsilon}[k]$ from the actual signal only the stochastic part will be left.

$$\tilde{\varepsilon}[k] = \varepsilon[k] - \hat{\varepsilon}[k] \tag{D.13}$$

In practice, a size of $J = 5$ in (D.12) was found sufficient and the coefficients a_j were found by optimisation over a representative data-set of each residual. This was done once. In the right plots of Fig. D.3 the autocorrelation is shown after whitening. Although the signal is not perfectly white this is found to be satisfactory for the change detection.

D.4.2 Distribution

Histograms of the noise on the residuals are shown in Fig. D.4. It is seen that

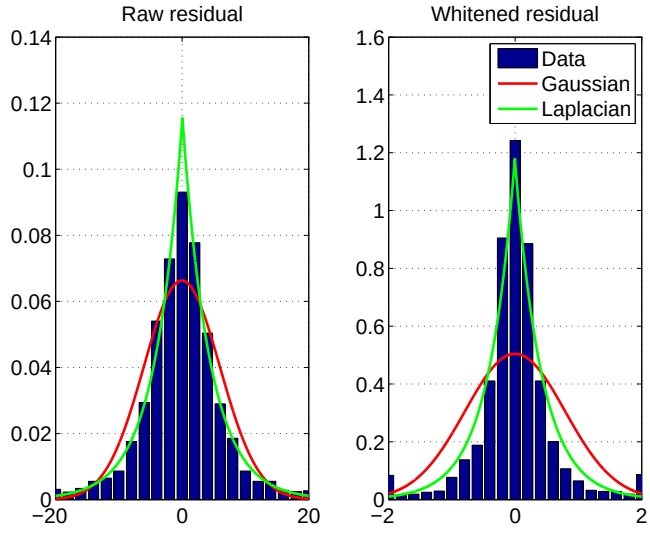

Figure D.4: Example of a histogram of r_{pa} (D.1) before and after whitening. Histograms of the other residuals have similar shapes.

the noise on the residuals does not follow the Gaussian distribution, especially after the whitening process. A Laplacian distribution given by

$$p(x; a, b) = \frac{1}{2b} \exp\left(-\frac{|x-a|}{b}\right) \tag{D.14}$$

gives a much better fit. This is verified by a Kolmogorov-Smirnov test done on a sample of consecutive residual data. Data are tested against a distribution where a and b in (D.14) are substituted by their maximum likelihood estimates (MLEs). The test shows that with a p-value of 0.064 the data come from the same distribution. A similar test is done for the MLE Gaussian distribution but with a p-value of only 4.5×10^{-4}, data cold not be Gaussian. Both tests were done on the data after the whitening process.

D.4.3 CUSUM detection

Two methods of detecting faults are compared in this paper. One is the popular CUSUM, theoretically valid to detect a change of known magnitude [8]. The algorithm is meant to distinguish between two hypotheses, $P_0(\boldsymbol{x}; \boldsymbol{\Theta})$ that denotes the probability of hypothesis $\mathcal{H}_0$ given input $\boldsymbol{x}$ and parameters $\boldsymbol{\Theta}$, and

$P_1(\boldsymbol{x};\boldsymbol{\Theta})$. The CUSUM at timestamp k is given by:

$$S[k] = \sum_{j=1}^{k} \ln \frac{P_1(\boldsymbol{x};\boldsymbol{\Theta})}{P_0(\boldsymbol{x};\boldsymbol{\Theta})} \tag{D.15}$$

This sum of the log-likelihood ratios given known distributions and observations $\boldsymbol{x(k)}$ exhibits negative drift when $\mathcal{H}_0$ is most likely and a positive drift when the alternative is the more likely of the two. Using the density function for the Laplacian distribution (D.14) this detector is easy to set up. When a fault occurs, a change in a is expected from 0 to $a_1 \neq 0$. For a CUSUM test, the value of a_1 is found empirically.

D.4.4 GLR test

Detection of a change of unknown magnitude is handled by a generalised likelihood ratio test (GLR). It is shown for instance in [77] that a test statistics for the generalised likelihood ratio test for detecting an unknown DC-level in white Gaussian noise is given by:

$$T_G(\boldsymbol{x}) = (N-1)\frac{\bar{x}^2}{\hat{\sigma}_w^2} \tag{D.16}$$

Where $\bar{x}$ is the sample mean and N the window length. The maximum likelihood estimate (MLE) of the variance $\hat{\sigma}_w^2$ is the variance estimate of data,

$$\hat{\sigma}_w^2 = \frac{1}{N-1}\sum_{n=1}^{N}(x[n]-\bar{x})^2 \tag{D.17}$$

A GLR test using the Laplacian distribution is given by

$$T_L(\boldsymbol{x}) = \left(\frac{\hat{b}_0}{\hat{b}_1}\right)^N \tag{D.18}$$

with the MLE's given by

$$\hat{b}_0 = \frac{1}{N}\sum_{n=1}^{N}|x[n]| \tag{D.19}$$

$$\hat{b}_1 = \frac{1}{N}\sum_{n=1}^{N}|x[n]-\text{median}(\boldsymbol{x})| \tag{D.20}$$

To get an expression that is more appropriate for numerical calculations, the natural logarithm of (D.18) is preferred as test statistics.

D.4.5 Detector thresholds

Finding a threshold for the GLRT is in theory done from the product of distributions of each calculation of the test statistics, T_L, by the GLRT. When the test statistic is correlated, calculation of the theoretical threshold becomes difficult, except in a Gaussian case. With uncertainty about the correlation of the test statistics and the distribution of residuals, a practical approach is to estimate the distribution of the test statistics under the no-fault hypothesis $\mathcal{H}_0$ and determine the threshold from the right-tail probability of the distribution of T_L for the GLRT. The thresholds are found by estimating the right-tail probability of the test statistics for the two detectors. The two test signals follow a Weibull

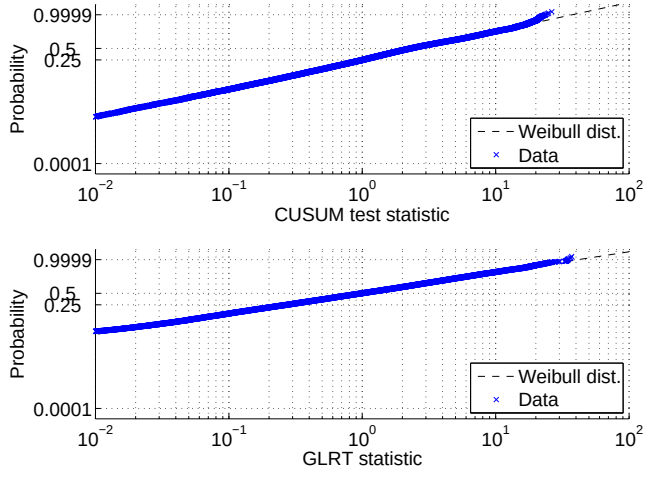

Figure D.5: Weibull distribution approximation of the CUSUM and GLRT statistics in the no fault case.

distribution as seen in Fig. D.5. The Weibull distribution (CDF) is given by $P(x) = 1 - exp(\frac{x}{v_{0g}})^{\beta_{0g}}$, with parameters v_{0g} and β_{0g}. The mathematical techniques to obtain the parameters are well known see, e.g. [7]. The threshold to obtain a desired false alarm probability P_{FA} is obtained as $\gamma = v_{0g}(-\ln P_{FA})^{\frac{1}{\beta_{0g}}}$. Using a threshold value of 100 gives a theoretical value of around 30 days between each false alarm. However, this value might be somewhat uncertain as especially the right tail of the CUSUM data differ from the theoretical distribution, as seen from Fig. D.5.

D.5 Results

In Fig. D.6 estimation of parameters is shown for residual D.2 for a typical fault free flight with the Banshee drone. A large transient is seen in the initial-

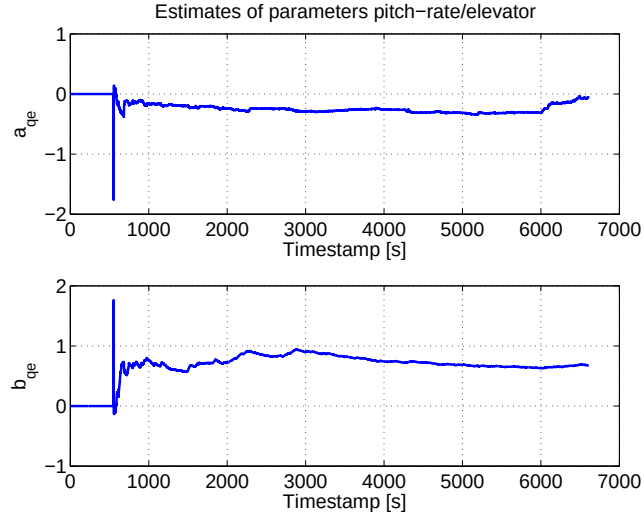

Figure D.6: Estimate of parameters from equation D.2.

isation phase but the parameters quickly settles at a stable value within 100 seconds. Because of this behaviour the fault diagnosis is not started until after the parameters estimation is initialised and has found a stable level. To achieve a faster startup, the parameters can be initialised with values from previous flights instead of zero. This gives almost no fluctuation in the startup phase.
Histograms and time series of the whitened residual formed by D.1 for two cases are shown in Fig. D.7. In the faulty flight an incident where one of the control arm of an aileron breaks off just before landing. The incidence happens approximately 4482 seconds into the flight.
It is hard to see the incidence on the raw residual due to the noise, but it is clearly visible that a change in the residual has occurred when looking at Fig. D.9 where the CUSUM and GLR test statistics are shown. These can be compared to Fig. D.8 which is test statistics for the fault free flight.
With the threshold of 100 estimated in section D.4.5 both methods will detect this particular fault at around 30 seconds after the fault occurs. With the characteristics of this particular fault there is no real difference in using one detection algorithm over the other.

D.6 Condensed Information to the Operator

The main point of the diagnosis described above is to give the operator of the UAV some useful information about the present condition of the aircraft. In order for him to act correctly if an alarm is raised some further information is

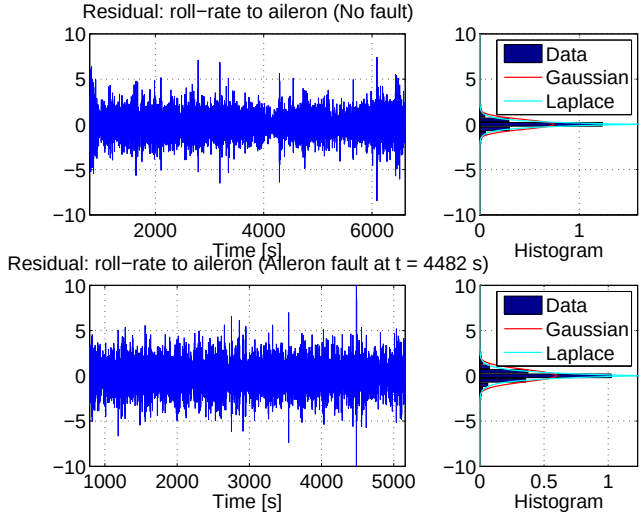

Figure D.7: Time and histogram development of residual from estimate of D.1. The two figures in the top shows the fault free case, and the bottom plots for a fault happening after 4482 seconds of flight.

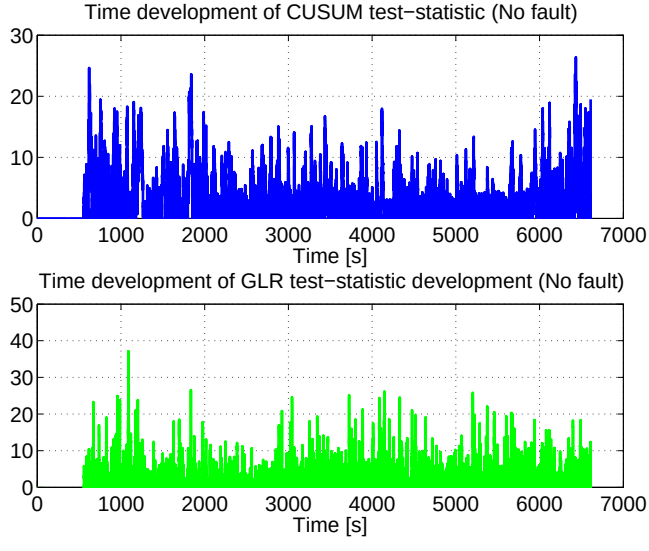

Figure D.8: CUSUM and GLRT development in the fault free case.

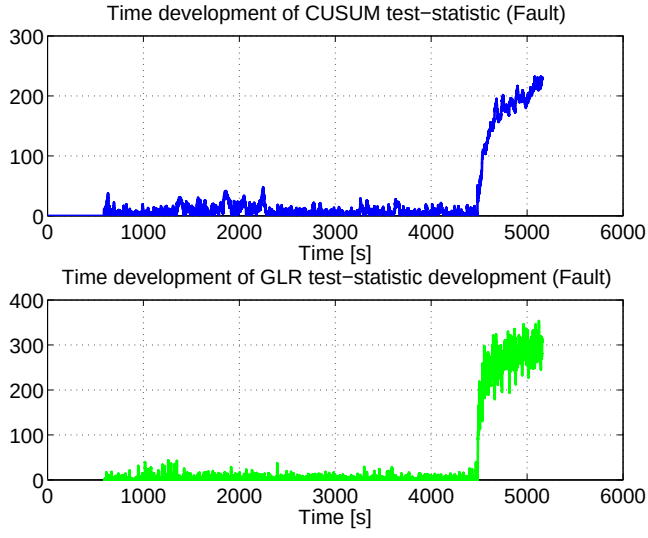

Figure D.9: CUSUM and GLR development for a dataset where a loss of control surface linkage during approach to landing.

derived based on the physics and construction of the drone. With the controls available on the Banshee drone 4 separate problems or a combination of these can occur. Based on past experience it is found that faults most often occur as a consequence of either the linkage from the servo motors to the the control surfaces or the actual control surface mounting breaking. Both faults leads to a non-functioning or partly non-functioning flap. Assuming that only one fault appears at a time, the following two issues can occur on this aeroplane,

- Left or Right elevator fault
- Left or Right aileron fault

Positions of the servo motors controlling each surface are not measured, so other means must be used to distinguish between each of the above faults. The relation D.1 is important in relation to this, since the balancing of forces from each control surface is along the aircraft's roll axis. When flying wings levelled and straight ahead with no faults present, the ailerons will have a small negative deflection to compensate for the moment created by propeller rotation propeller as illustrated in Fig. D.10. If we assume only one of the listed faults happens at a time, this balance will be shifted. If for example the left aileron fails the force F_L disappears in Fig. D.10. This means F_R must be twice the size it was when in the fault free case. If a left turn is commanded even further deflection must be done by the remaining working surface. It would therefore seem natural to

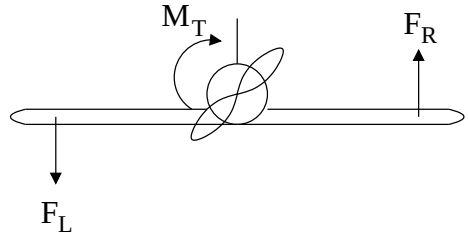

Figure D.10: Sketch aircraft with control surface on each wing reacting against the engine moment.

command right turn manoeuvres. However when doing a right turn the control surfaces must be able to stop the rolling motion which again means deflecting to the right. The roll angle overshoot will therefore in this case becomes much larger than in the fault free case and therefore control of the aircraft can be lost if to large roll angles are used. This means the working flight envelope of the aircraft is reduced.

D.7 Conclusion

This paper investigated change detection methods applied on limited bandwidth telemetry data for an autonomous aircraft. Models of sufficient simplicity were derived and parameter estimation was combined with detection of change of the prediction error between measurements and the prediction made by a model using the parameters being adapted to. Results with real-life data assessed the need for whitening filters, and showed the robustness of CUSUM and GLRT change detection methods. The combination of statistical change detection with the parameter adaptive models showed to be successful and it was possible to advise the operator about limitations in safe flight envelope for scenarios with real failures.

Paper E

Diagnosis of Airspeed Measurement Faults for Unmanned Aerial Vehicles[1]

Søren Hansen and Mogens Blanke

Abstract

Airspeed sensor faults are common causes for unmanned aerial vehicle incidents. Pitot tube clogging or icing are common causes. Timely diagnosis of such faults or artifacts could potentially prevent crashes. This paper employs parameter adaptive estimators to provide analytical redundancies and a dedicated diagnosis scheme is designed. Robustness is investigated on sets of flight data to estimate distributions of test statistics. The result is robust diagnosis with adequate balance between false alarm rate and sensitivity.

E.1 Introduction

A reliable measurement of airspeed is vital to many simple Unmanned Aerial Vehicles (UAV), since the envelope of stable operation becomes narrow for simple autopilots if speed information is in error. Simple UAV autopilots rarely make use of redundant speed measurements both to avoid the added complexity and due to limitations on weight. Ability to diagnose speed sensor faults without adding additional sensors or actuators to the aircraft would hence be very attractive.
Estimating speed by exploiting other sensors onboard could be possible through state estimation techniques. An aircraft can be described by a set of nonlinear

[1]Submitted to IEEE Transactions on Aerospace and Electronic Systems.

equations with a rich set of parameters, but as it is not feasible, to obtain complete parameter sets for small UAVs, for reasons of cost, estimation of states could be based on models where some parameters are roughly known while others require identification. Several parameters depended on states of the aircraft and vary as the operational conditions change, so combined parameter and state estimation would appear useful. When the structure of nonlinearity is known in a nonlinear dynamical system, and stochastic disturbances are not significant, adaptive observers for nonlinear systems may serve the dual purpose of parameter and state estimation. When stochastic issues become significant and local linearization around a state vector is feasible, Extended Kalman filtering (EKF) techniques are preferred. The literature on both approaches is significant. Such estimation requires certain properties of the nonlinear system. Observability is essential, and this is treated for nonlinear observers in [124]. When the system equations are not simple and calculation of Lie derivatives of the system equations are required, this can be cumbersome. A relaxed approach is to ensure asymptotic convergence to zero of the estimation error. For an adaptive observer, global asymptotic stability can be analyzed employing Lyapunov stability results, as done in [34]. Properties of the extended Kalman filter as a combined state and parameter estimator was treated in other classical results, [85] for linear systems and [141] for a class of nonlinear systems. Once alternative estimates of aircraft speed have been obtained, fault diagnosis could be achieved through residual generation and change detection methods could be adopted to obtain robust diagnosis.

Fault detection and isolation (FDI) has been demonstrated for nonlinear systems with a structure similar to that of aircraft propulsion in for instance [46], who used a sliding mode observer, and in [22], where an adaptive observer was employed. Fault detection, isolation and recovery (FDIR) for aircraft and aerospace systems was studied in [47], that included nonlinear control for recovery, in [136] where partial loss of control surfaces was treated and overviews of theoretical diagnostic techniques for general aircraft faults were treated in [128], [143] and [91]. Goupil [59] showed how FDIR techniques are in use in the Airbus 380.

Approaches to FDI for unmanned aircrafts were the subject of [43], who treated actuator fault diagnosis and [44] who developed multiple model adaptive estimation for sensor and actuator faults. Extended Kalman filtering techniques were combined with diagnosis to obtain fault-tolerant control in [14] who also demonstrated detection of faults and degraded performance of actuators using both simulated and real flight data. The airspeed sensor problem was not dealt with in this literature. A general structural analysis was conducted by [50] for a non-linear aircraft model, and structural detectability and isolability properties were determined. Classical diagnostic techniques was shown, but on simulated data. Specific faults and failure modes have also attracted considerable attention, performance monitoring and detection of oscillatory behavior was treated in [2]. Research on the airspeed sensor problem using multiple sensors have been treated in [117] and [131] who analyzed performance of linear time-invariant fault

detection methods applied on parallel airspeed sensors, but more general results on airspeed sensor fault diagnosis have been sparse. Larger manned aircraft use heating of airspeed sensors to prevent icing but this is not always enough to avoid problems. The final report on the Air France AF447 accident [29] states that the pilots misinterpretation of faulty airspeed measurements was the leading cause of the incident. This has caused a lot of visibility in the flight control system community towards air speed sensor faults and alternatives to the use of classical voting principles as sole means of fault diagnosis.

The present research started well in advance of the AF447 accident because air speed sensor signal faults and artifacts have long been an issue on small unmanned aircraft. The paper focus on the airspeed sensor FDI problem using non-linear analytical redundancies. Early results [65] showed that fault detection for clogging of a pitot tube was feasible but used a simplified setup where wind was assumed known and propulsion dynamics was known a priori. This paper presents a complete solution to the airspeed sensor detection problem where wind speed and propulsion dynamics are unknown. An extended Kalman filter technique is adopted to the problem at hand to estimate the wind velocity vector while flying and propulsion system parameters and airspeed are estimated by a dedicated nonlinear observer. The test statistics obtained by generalized likelihood change detection is scrutinized using multiple flight experiments to obtain parameters for the distribution of the test statistics, both in normal and faulty conditions. It is shown how the parameters of estimated test statistics can be used to determine thresholds for detection that guarantee very low probability of false alarms while ensuring adequate detection capability. A special methodology is developed to avoid false diagnosis for return to normal, which is a problem for an aircraft that experience uncontrolled nonlinear behavior at the boundary of stability or in rapid maneuvers. It is discussed how the diagnostic scheme could be implemented as part of on-board avionics but also, as an added benefit for wider use, be implemented as part of a mission supervisor on a ground station based on telemetry from the aircraft. If a fault is detected an alarm could be raised to let the operator of the aircraft take appropriate action to bring it down safely.

The paper is structured as follows. Following a brief problem statement and presentation of selected parts of equations of motion and propulsion dynamics, a set of residuals relations are derived. To cope with parameter uncertainty and variability, a non-linear high-gain observer is used to estimate the force balance on the aircraft to get the expected speed from thrust relations of the propeller. Wind speed is estimated by an EKF such that ground speed measurements from an onboard GPS receiver can turned into an airspeed estimate. Robust residual generators are implemented and validated using recorded flight data.

E.2 Banshee UAV system

Research on fault diagnosis is often based primarily on simulation studies, but the randomness caused by practical conditions for unmanned aircrafts, including change of payload, pre-flight trimming and control surface adjustments, cause flight conditions to vary more than commonly captured in simulations. The results in this paper are based on data records from a large number of UAV flights under, most under what are considered normal conditions, some are cases of real faults that led to incidents with loss of aircraft.

This section gives a short introduction to the UAV from which data originate. The aircraft is a Banshee drone from Meggitt Defence Systems (UK), widely used for target practise in several countries [92].

The Banshee UAV is a delta wing aircraft propelled by a rear mounted engine. The thrust is delivered by a 2 bladed propeller. It is launched from a catapult system (see Fig. E.1) and lands by parachute. It is not equipped with a landing gear.

Figure E.1: A Banshee UAV is made ready for launch. *Foto: Danish Forces Joint UAV Team*

The aircraft has an avionics with an autopilot system that is operated via telemetry from ground. A path to follow is defined by a number of waypoints and speed to be followed between waypoints. It is technically possible to fly the drone manually and throttle command to control speed is feasible, but when out of sight, remote command for attitude control is difficult if not impossible.

E.2.1 Banshee Sensors and Actuators

In the configuration used for the tests in this paper, the Banshee UAV was equipped with actuators and sensors, listed in Table E.1, together with the associated signals.

Table E.1: List of commands and measured output

Symbol	Unit	Explanation
h_p	m	Altitude measured by pressure
v_{pitot}	m/s	Airspeed measured by pitot tube
λ_{lat}, λ_{lon}	deg	Latitude and longitude measured by GPS
v_{gps}, ψ_{gps}	m/s, deg	Speed and course over ground from GPS
p_i,q_i,r_i	deg/s	Roll rate, pitch rate, and yaw rate measured by IMU
a_x,a_y,a_z	m/s^2	Body axis accelerations measured by IMU
n	s^{-1}	Engine revolutions
δ_T	%	Throttle
δ_a	deg	Aileron deflection
δ_e	deg	Elevator deflection

The autopilot on this drone has a non-redundant architecture and depends solely on individual sensor input to function correctly. Only one sensor is present for each physical variable and possible sensor artifacts or faults ripple directly to the avionics. Faults on actuators limit the envelope within which stable flight is possible. Calculating the flight envelope through a linear matrix inequality problem formulation was pursued in [10] and [14]. With closed loop speed control along a track and attitude controller parameters being scaled by airspeed, erroneous airspeed input will limit the flight envelope, in particular when conducting sharp turns or other maneuvers. Remedial actions on this UAV in its standard configuration are possible only via telemetry from ground. If an airspeed sensor issue is detected, the autopilot can be switched to a mode without closed loop speed control; a less agile attitude control can be selected to obtain better robust stability; the ultimate fail-safe reaction is to stop the engine and release the parachute. Activation of remedial action via ground station command requires that the diagnostic result is available and presented to the operator timely enough to intervene. Time to detect, fault isolation probability and false alarm probability are essential quality parameters that will be design drivers in the sequel.

E.3 Thrust delivered by the propeller

The Banshee is propelled by a rear mounted combustion engine with a 2 bladed wood propeller. The thrust developed by this engine F_T is given by k_T, a non-

dimensional thrust coefficient, made dimensional by

$$F_T = k_T \varrho n^2 d_p^4, \tag{E.1}$$

where propeller diameter is d_p, shaft speed n, and ϱ the air density. Wind tunnel tests (see [83]) of propellers of the type used reveals that the thrust coefficient is approximately linear with the advancement ratio $J = \frac{v}{nd_p}$, where v is inflow velocity to the propeller. The thrust coefficient and NACA data are plotted in Fig. E.2. In nominal flight J is in the range 0.9 to 1.1.

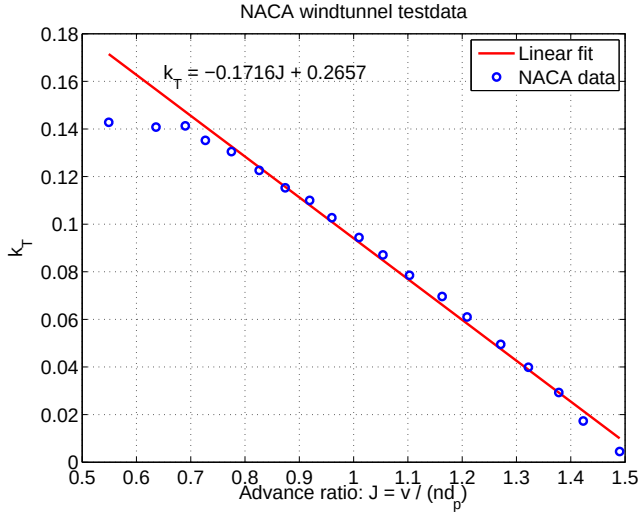

Figure E.2: NACA wind tunnel test of two bladed propeller. Non-dimensional thrust k_T versus advancement ratio J.

Propellers are usually characterized by their diameter d_p and pitch P_p. These values can be combined to a non-dimensional pitch defined by $P' = \frac{P_p}{d_p}$. The following scaling for the thrust coefficient was proposed by [99]

$$k_T(J) \simeq k_{T,\text{ref}}(J - (P' - P'_{\text{ref}})), \tag{E.2}$$

where $k_{T,\text{ref}}$ and P'_{ref} are the thrust coefficient and non-dimensional pitch of the reference signal, respectively. The reference signals originates from different propellers tested in [83]. The 26×32 propeller used on the Banshee has P' equal to that of one of the tested propellers and the characteristics of this propeller are used.

Calculating dimensional lift and drag on a propeller, it was shown in [20] that thrust is related to advance speed v and propeller angular speed n by the bi-

linear expression

$$F_T = T_{nn}n^2 + T_{nv}nv, \tag{E.3}$$

which was shown equivalent to a linear approximation to non-dimensional thrust

$$k_T = k_{T0} + k_{T1}J, \tag{E.4}$$

where dimensional and non-dimensional parameters are related as $T_{nn} = k_{T0}\varrho d_p^4$ and $T_{nv} = k_{T1}\varrho d_p^3$.

E.4 Possibilities for diagnosis

When three measurements of a compatible quantity V_k are available, the classical *Voting Scheme* technique for fault isolation calculates the three differences $V_i - V_j$, $(i,j) \in [1,2,3], i \neq j$. The measurements available on the aircraft provide, at a first glance, three obvious redundancies, the airspeed measurement v_{pitot}, velocity measured by GPS and compensated for wind $v_{gps2air}$, and the expected velocity v_{thrust} obtained at a known shaft speed of the engine. This gives rise to the parity relations shown in Table E.2, which were also used in [65]. A

Table E.2: Measurements and Voting Scheme residuals.

Residual	v_{pitot}	$v_{gps2air}$	v_{thrust}
R_1	1	1	0
R_2	1	0	1
R_3	0	1	1

"1" in Table E.2 means the residual is affected by the measurement, and since all three columns have different column signatures, faults on each of the three measurements could appear as easily isolable. The catch in this argument is that $v_{gps2air}$ and v_{thrust} are not independent of v_{pitot}: $v_{gps2air}$ need an estimate of wind velocity, which requires the airspeed through v_{pitot}; v_{thrust} is dependent on propulsion parameters, trim and loading conditions, and parameter adaptation also needs v_{pitot}. These apparent difficulties are analyzed and overcome in the sequel of the paper, and it is shown how a combination of estimation, adaptation, statistical change detection and dedicated hypothesis testing together can solve the robust fault isolation problem.

E.5 Residual R_1 from ground speed and estimated wind

An estimate of the wind velocity vector is needed to create residual R_1 comparing airspeed readings: One from the pitot tube system, the other being the sum of GPS measured ground speed plus estimated wind vector. In [33] such

an estimate was developed with the purpose of calibrating the airspeed sensor of a small UAV. Since this estimation algorithm is simple and is shown to work well for an aircraft with the same instrumentation as the Banshee, it is adopted here albeit with a different end purpose, namely fault detection.
The aircrafts velocity relative to air $\boldsymbol{v}_{rel}$ is related to the ground speed vector $\boldsymbol{v}_g$ according to the following vector sum: $\boldsymbol{v}_g = \boldsymbol{v}_{rel} + \boldsymbol{v}_w$. The wind velocity vector is defined such that it points in the direction the wind blow. The size of the airspeed can then be formulated using the standard cosine rule for triangles

$$v_{rel}^2 = v_w^2 + v_g^2 - 2v_g v_w \cos(\psi_w - \psi_g), \tag{E.5}$$

where the wind direction is ψ_w and the heading of the aircraft is denoted ψ_g. The relationship is illustrated in Figure E.3.

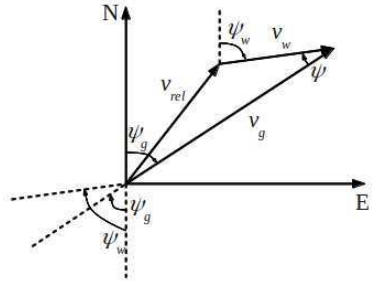

Figure E.3: Relationship between ground speed, airspeed and wind speed.

The pitot tube basically measures the dynamic pressure of the wind flow based on pressure readings from a tube pointing in the aircrafts forward direction and static vent on the fuselage. Therefore, the pitot tube reading is a measure of the forward speed u in the body frame (Appendix E.11). To take differences between the measurement from the pitot tube and the aircraft's real speed due to attack angle, α, and sideslip, β, into account, a factor between the two values also needs to be estimated,

$$v_{pitot} = \cos(\alpha)\cos(\beta)v_{rel} \simeq a v_{rel}. \tag{E.6}$$

An EKF was used in [33] to estimate the wind vector and a scaling factor. The dynamic pressure was available as a measurement on the aircraft and was therefore used in the measurement equation. For the Banshee the airspeed is given as a velocity and (E.5) is used directly as measurement equation.
The state vector of the EKF is given by $\boldsymbol{x} = [v_w, \psi_w, a]^\mathrm{T}$ and states are modelled as random-walk processes. This gives the state transition

$$\boldsymbol{x}_k = \boldsymbol{I}\boldsymbol{x}_{k-1} + \boldsymbol{\nu}_k, \tag{E.7}$$

with $\boldsymbol{\nu}_k \sim \mathcal{N}(0, \boldsymbol{Q}_k)$. The pitot tube measurement can be estimated from the states by the following observation equation based on (E.5)

$$\hat{h}(\boldsymbol{x}) = a\sqrt{v_w^2 + v_g^2 - 2v_g v_w \cos(\psi_w - \psi_g)}. \tag{E.8}$$

Since the ground speed and heading is estimated by the onboard GPS receiver this observation equation can be reformulated as

$$\hat{h}(\boldsymbol{x}) = a\sqrt{v_w^2 + v_{gps}^2 - 2v_{gps} v_w \cos(\psi_w - \psi_{gps})}. \tag{E.9}$$

This leads to the following Jacobian

$$\boldsymbol{H} = \begin{bmatrix} \dfrac{a\left(2v_w - 2v_{gps}\cos(\psi_w - \psi_{gps})\right)}{2\sqrt{v_w^2 + v_{gps}^2 - 2v_{gps}v_w\cos(\psi_w - \psi_{gps})}} \\ \dfrac{a\left(2v_w v_{gps}\sin(\psi_w - \psi_{gps})\right)}{2\sqrt{v_w^2 + v_{gps}^2 - 2v_{gps}v_w\cos(\psi_w - \psi_{gps})}} \\ \sqrt{v_w^2 + v_{gps}^2 - 2v_{gps}v_w\cos(\psi_w - \psi_{gps})} \end{bmatrix}^{\mathsf{T}}. \tag{E.10}$$

The standard EKF algorithm (see eg. [28]) is utilized using the above equations. This gives the following time update step

$$\hat{\boldsymbol{x}}_{k|k-1} = \hat{\boldsymbol{x}}_{k-1|k-1} \tag{E.11}$$

$$\boldsymbol{P}_{k|k-1} = \boldsymbol{P}_{k-1|k-1} + \boldsymbol{Q}_k, \tag{E.12}$$

and the measurement update is

$$\tilde{\boldsymbol{y}}_k = \boldsymbol{z}_k - \hat{h}(\boldsymbol{x}_{\boldsymbol{k|k-1}}) \tag{E.13}$$

$$\boldsymbol{K}_k = \boldsymbol{P}_{k|k-1}\boldsymbol{H}_k{}^{\mathsf{T}}\left(\boldsymbol{H}_k\boldsymbol{P}_{k|k-1}\boldsymbol{H}_k{}^{\mathsf{T}} + \boldsymbol{R}_{k-1}\right)^{-1} \tag{E.14}$$

$$\hat{\boldsymbol{x}}_{k|k} = \hat{\boldsymbol{x}}_{k|k-1} + \boldsymbol{K}_k\tilde{\boldsymbol{y}}_k \tag{E.15}$$

$$\boldsymbol{P}_{k|k} = \left(\boldsymbol{I} - \boldsymbol{K}_k\boldsymbol{H}_k\right)\boldsymbol{P}_{k|k-1}. \tag{E.16}$$

The covariances $\boldsymbol{Q}_k$ and $\boldsymbol{R}_k$ are found from analysis of segments of data during level flight. Alternatively they could be estimated in the filter following methods suggested for linear systems in Ljung's innovations filter [85] and extended to nonlinear systems in [141].

A typical development of the states for a flight is shown in Fig. E.4. The wind was measured on ground to be 6.8 m/s at 80°, however, since the aircraft was flying at heights up to 1500 m the ground measured velocity was not representative. The innovation of the filter is the difference between the measured air speed component in the x direction and the x-component estimated from ground speed plus the contribution from wind. This innovation, Eq. (E.13), is used as residual R_1 from Table E.2. With actual variables inserted

$$R_1 = v_{pitot} - \hat{a}\sqrt{\hat{v}_w^2 + v_{gps}^2 - 2v_{gps}\hat{v}_w\cos(\hat{\psi}_w - \psi_{gps})}. \tag{E.17}$$

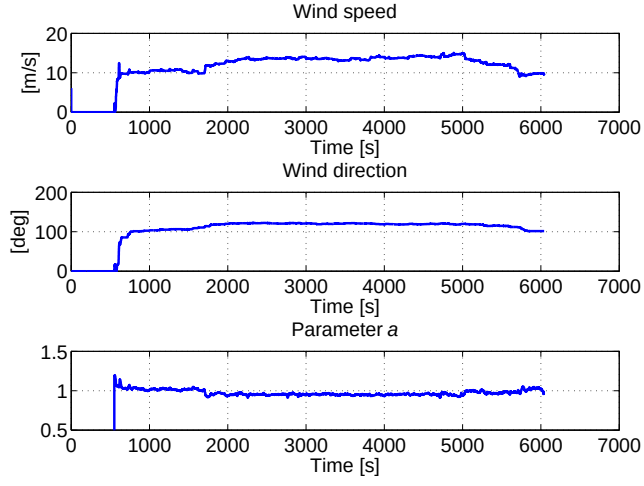

Figure E.4: Estimates of wind parameters during a flight at altitude up to 1500 m.

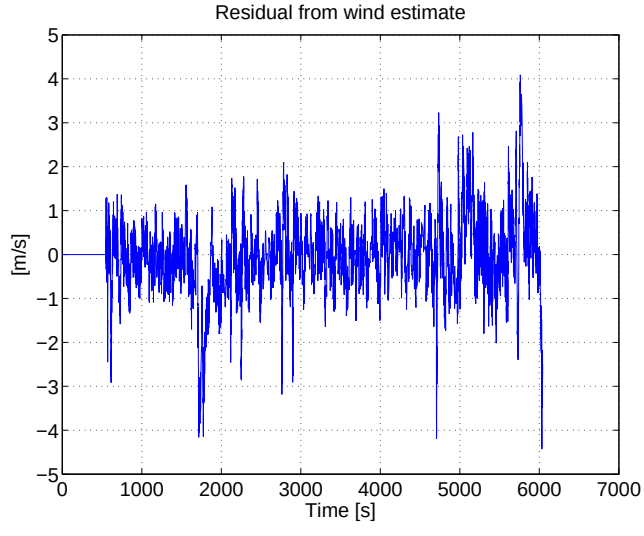

Figure E.5: Time development of the innovation of the EKF for same flight as in Fig. E.4.

The time-history of R_1 is plotted in Fig. E.5 for the same flight as was illustrated in Fig E.4.

E.6 Residual R_2 from adaptive observer based on propeller speed

The second residual R_2 in Table E.2 is based on thrust delivered by the engine and an associated estimate of airspeed. This estimate is available through exploiting the dynamics, in component form

$$\begin{aligned} m\dot{u} &= m(rv - qw) + F_{Ax} - mg\sin(\theta) + F_T, && \text{(E.18)} \\ m\dot{v} &= m(pw - ru) + F_{Ay} + mg\cos(\theta)\sin(\phi), && \text{(E.19)} \\ m\dot{w} &= m(qu - pv) + F_{Az} + mg\cos(\theta)\cos(\phi). && \text{(E.20)} \end{aligned}$$

The aircraft's motion is described by its linear and angular velocities, $\boldsymbol{v}_b = [u, v, w]^{\mathsf{T}}$ and $\boldsymbol{\omega} = [p, q, r]^{\mathsf{T}}$, in the body frame, the euler angles ϕ, θ, ψ. The aerodynamic forces are F_{Ax}, F_{Ay}, F_{Az} and F_T is the thrust forces derived in section E.3.
The velocities are related to the relative airspeed, v_{rel}, as

$$\begin{aligned} u &= v_{rel}\cos(\alpha)\cos(\beta), && \text{(E.21)} \\ v &= v_{rel}\sin(\beta), && \text{(E.22)} \\ w &= v_{rel}\sin(\alpha)\cos(\beta), && \text{(E.23)} \\ v_{rel} &= \sqrt{u^2 + v^2 + w^2}. && \text{(E.24)} \end{aligned}$$

As the aircrafts fly with wings levelled most of time the magnitudes of v and w generally are small so when calibrated, the pitot tube provides a reading of the forward airspeed, hence

$$u = v_{pitot}, \tag{E.25}$$

and the velocity can be approximately described using only the u term in (E.18). Since the aerodynamic force F_{Ax} is unknown, this term has to be estimated by the observer. This is done by adding an adaptation scheme to the observer. It is customary to describe forces in terms of non-dimensional parameters, for reasons of scaling, and it provides some numerical advantage to use this representation in the adaptive observer. The aerodynamic force in the x direction is,

$$F_{Ax} = \bar{q}SC_x = \tfrac{1}{2}\varrho v_{rel}^2 SC_x, \tag{E.26}$$

with $\bar{q}$ being the dynamic pressure and S the surface area of the aircraft. C_x is composed by lift C_L and drag C_D as (from [122])

$$C_x = C_L\sin(\alpha) - C_D\cos(\alpha). \tag{E.27}$$

Based on this the following model for F_{Ax} is suggested. It contains two unknown parameters $\boldsymbol{\Theta} = [\Theta_{uu}, \Theta_{uu\alpha}]^{\mathsf{T}}$ to be estimated.

$$F_{Ax} = \tfrac{1}{2}\varrho S u^2\left(\Theta_{uu} + \Theta_{uu\alpha}\alpha\right) \tag{E.28}$$

This model depends on α which is not desirable because most low cost UAV's does not have a direct measurement of this value. Instead a model only containing the velocity dependent part is suggested. and if α is not available, the following one-parameter approximation is used

$$F_{Ax} = \tfrac{1}{2}\varrho S u^2 \Theta_{uu}. \tag{E.29}$$

Both force models (E.28) and (E.29) was tested on real data to see which one gives the best estimates for the purpose of fault diagnosis. The Banshee does not have a vane measuring α but an estimate is available from the autopilot. Using this estimate in getting F_{Ax} from (E.28) does not give any additional performance compared to (E.29). This could be because the α estimate is inaccurate or the tested flight patterns does not exceed the α dependence enough. Therefore the fault diagnosis is done using (E.29) for F_{Ax}. Results from using the two estimates are given in section E.6.1.
The derivation is continued for the two parameter model (E.28), but the results are valid also for the one-parameter model by setting $\Theta_{uu\alpha} = 0$ in the following. The model for F_{Ax} can be written as

$$F_{Ax} = m\left(F_1(u,t)\Theta_{uu} + F_2(u,t)\Theta_{uu\alpha}\right), \tag{E.30}$$

where the $F_1(u,t)$ and $F_2(u,t)$ are defined as

$$F_1(u,t) = \frac{\varrho S u^2}{2m} \quad , \quad F_2(u,t) = \frac{\varrho S u^2 \alpha}{2m}, \tag{E.31}$$

and m is pre-multiplied on the right hand side of (E.30) for later convenience.
From the system equations (E.18), the following nonlinear, adaptive observer is a natural choice for estimation of u. Let $\hat{u}$ denote the estimate of u and let L be the gain the observer uses to update the estimate of linear acceleration from the output innovation $u - \hat{u}$. The measurement of u is obtained from the pitot tube measured air speed v_{pitot} according to (E.25). Hence

$$\dot{\hat{u}} = -g\sin(\theta) + \frac{T_{nn}n^2 + T_{nu}n\hat{u}}{m} + F_1(\hat{u},t)\hat{\Theta}_{uu} + F_2(\hat{u},t)\hat{\Theta}_{uu\alpha} + L(v_{pitot} - \hat{u}). \tag{E.32}$$

The pitch angle θ is estimate by the onboard inertial measurement unit.
The unknown parameters are estimated using a standard adaptive observer updating approach, (see e.g [34])

$$\begin{bmatrix} \dot{\hat{\Theta}}_{uu} \\ \dot{\hat{\Theta}}_{uu\alpha} \end{bmatrix} = \begin{bmatrix} F_1(\hat{u},t) \\ F_2(\hat{u},t) \end{bmatrix} (v_{pitot} - \hat{u}). \tag{E.33}$$

The estimation is initialized with values found during previous fault-free flights. This ensures a fast transient period.

The extended state and parameter vector $\boldsymbol{x}$ of the observer is then

$$\dot{\hat{\boldsymbol{x}}} = \begin{bmatrix} \dot{\hat{u}} \\ \dot{\hat{\Theta}}_{uu} \\ \dot{\hat{\Theta}}_{uu\alpha} \end{bmatrix} = \begin{bmatrix} \dot{\hat{u}} \\ F_1(\hat{u},t)(v_{pitot} - \hat{u}) \\ F_2(\hat{u},t)(v_{pitot} - \hat{u}) \end{bmatrix}, \tag{E.34}$$

and with parameters Θ_{uu} and $\Theta_{uu\alpha}$ assumed unknown constants, the error dynamics is

$$\boldsymbol{f}(\tilde{\boldsymbol{x}}) = \dot{\tilde{\boldsymbol{x}}} = \dot{\boldsymbol{x}} - \dot{\hat{\boldsymbol{x}}} = \begin{bmatrix} \dot{\tilde{u}} \\ \dot{\tilde{\Theta}}_{uu} \\ \dot{\tilde{\Theta}}_{uu\alpha} \end{bmatrix} = \begin{bmatrix} \dot{\tilde{u}} \\ -F_1(\hat{u},t)\tilde{u} \\ -F_2(\hat{u},t)\tilde{u} \end{bmatrix}. \tag{E.35}$$

For the diagnosis the error $\tilde{u}$ of the observer expresses exactly what residual R_2 from Table E.2 contains, a comparison between airspeed measured by the pitot tube u and an estimate $\hat{u}$ based on the thrust force delivered by the engine.
The observer gain L must be chosen high enough to ensure that the observer is uniformly asymptotically stable. A stability proof is provided in Appendix E.12. In order for the observer to have good performance with respect to the fault diagnosis it is important to choose a gain value that allows sufficient deviation of the error value. Too high a gain could give an observer that could track measurements, thereby creating fairly weak detectability of a sensor fault, but also making estimated parameters change so much that the parameter change itself should trigger an alarm. When deciding whether to detect a change from the observer's innovation, or from the estimated parameters, it is worth noting that the innovation is driving the parameter updating, and a change (fault) in the generating process or sensor is therefore first visible in the innovation. It is hence a natural choice to use the innovation for change detection when rapid detection is of prime concern.
Using model parameter adaptation together with residual generation based on the filter innovation raises questions about how and when the estimator itself need be updated to changed conditions. Some techniques to combine change detection with change in adaptation gains was treated in [61], who demonstrated the combined technique on detection of multiple changes, but the problem is an area of continued research [73]. Aiming at fast online diagnosis, this paper will halt adaptation when the output (test statistics) from a change detector exceeds specified values, which are lower than the chosen alarm threshold, and a special hypothesis test will be developed to prevent false resetting of alarms.

E.6.1 Observer performance

The performance of the adaptive observer was tested using recorded data from 18 flights with the Banshee UAV. Fig. E.6 shows the estimated speed of the vehicle compared with measured airspeed in the upper part of the plot and the

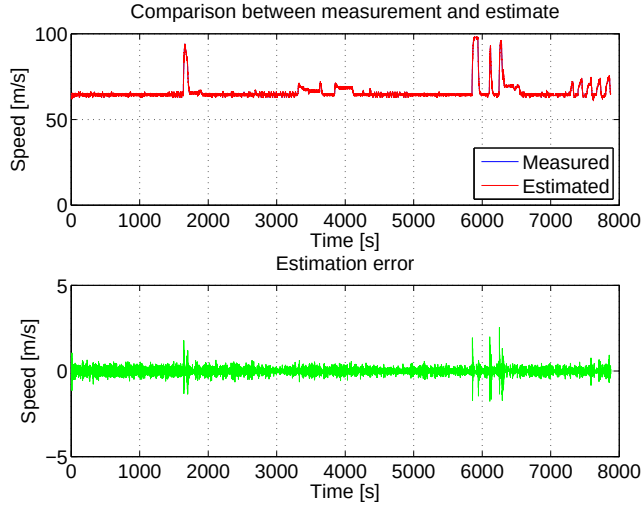

Figure E.6: Observer performance and choice of model.

observer's innovation in the lower plot. It is apparent that the observer is stable and the standard deviation of the error, for the given flight, is 0.23 m/s, which is satisfactory compared to the 0.5 m/s present on the airspeed measurement when we do not wish too high filtering (low bandwidth) in the adaptive observer as this would delay fault detection.

The unknown parameters $\boldsymbol{\Theta}$ behave, over time, as seen on Fig. E.7. Fig. E.7 also shows that $\hat{\Theta}_{uu\alpha}$ drifts in value. This has no effect on the residual since its value is very small compared to $\hat{\Theta}_{uu}$ and the reasons could include some change in trim as fuel is consumed during the flight. Another reason for the drift could be that the angle of attack, α, does not vary much and sufficient excitation is not present to identify $\hat{\Theta}_{uu\alpha}$ without drift. The one-parameter formulation (E.29) avoids this issue, it is simpler and it's innovation has very similar properties. The two parameter observers standard deviation error is 0.22 m/s compared to 0.23 m/s for the one parameter setup. The parameter estimate using the one-parameter adaptation scheme is shown in the middle plot of Fig. E.7. The observer in the one-parameter version

$$\dot{\hat{\boldsymbol{x}}} = \begin{bmatrix} \dot{\hat{u}} \\ \dot{\hat{\Theta}}_{uu} \end{bmatrix} = \begin{bmatrix} -g\sin(\theta) + \dfrac{T_{nn}n^2 + T_{nu}n\hat{u}}{m} + F_1(\hat{u},t)\hat{\Theta}_{uu} + L(v_{pitot} - \hat{u}) \\ F_1(\hat{u},t)(v_{pitot} - \hat{u}) \end{bmatrix}, \tag{E.36}$$

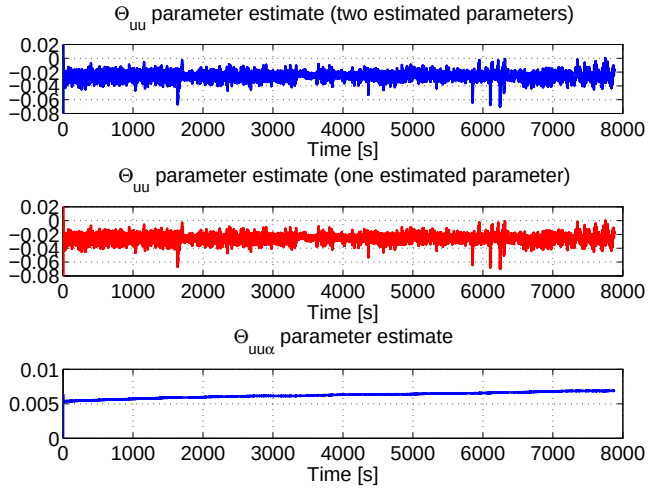

Figure E.7: Parameter development during estimation. The blue plots are the two parameter observer which has $\sigma_{\tilde{u}} = 0.22$ m/s and the red curve represents the one parameter setup which has $\sigma_{\tilde{u}} = 0.23$ m/s.

and residual R_2, which equals the observer innovation, $\tilde{u} = u - \hat{u}$, reads

$$R_2 = v_{pitot} + \left(\int g \sin(\theta) - \frac{T_{nn} n^2 + T_{nu} n \hat{u}}{m} - F_1(\hat{u}, t) \hat{\Theta}_{uu} dt \right) - L(v_{pitot} - \hat{u}). \tag{E.37}$$

E.7 Residual R_3 from comparison of velocity estimates

Following the voting scheme described in Table E.2 the third residual is the difference between the two estimates of airspeed. Since both $v_{gps2air}$ and v_{thrust} relies on the airspeed measurement in their estimation procedures, it is impossible achieve independence of v_{pitot}. However, since the purpose of R_3 is to ensure isolability of the airspeed measurement fault, its value is only required when R_1 and/or R_2 indicate an alarm. With

$$\begin{aligned} R_3 &= v_{gps2air} - v_{thrust} \\ &= \hat{a} \sqrt{\hat{v}_w^2 + v_{gps}^2 - 2 v_{gps} \hat{v}_w \cos(\hat{\psi}_w - \psi_{gps})} + g \sin(\theta) \\ &- \frac{T_{nn} n^2 + T_{nu} n \hat{u}}{m} - F_1(\hat{u}, t) \hat{\Theta}_{uu} - L(v_{pitot} - \hat{u}). \end{aligned} \tag{E.38}$$

and setting adaptation on hold when a fault is detected, R_3 can be used for isolation. If an airspeed fault is detected, v_{pitot} can not re-enter in calculations

that estimate $v_{gps2air}$ and v_{thrust}. These estimates will therefore after a while become increasingly uncertain, which in turns affects R_3. However, as long as R_3's value is reliable up to and shortly after detection, it serves the purpose.

E.8 Change Detection

As in [65] fault detection is achieved by detecting changes to the residual signals (E.17) and (E.37). Generalized Likelihood Ratio Tests (GLRT) are used to distinguish between to possible hypothesis about the residual signals.

$$\begin{aligned} \mathcal{H}_0 : x[n] &= w[n] \\ \mathcal{H}_1 : x[n] &= A + w[n]. \end{aligned} \tag{E.39}$$

The $\mathcal{H}_0$ hypothesis is that only the expected noise is present on the signal and the alternative $\mathcal{H}_1$ hypothesis states that the signal has been offset from 0 by a value of A. If this is the case there must be a significant difference between the measurement and the model and hence a fault is present. In Fig. E.8 the

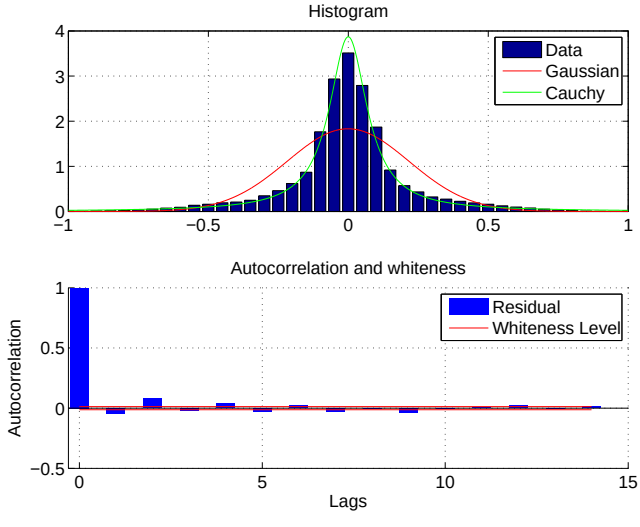

Figure E.8: Residual from wind estimating EKF characteristics.

histogram and autocorrelation of the residual from the wind estimator is shown. The residual has been pre-whitened and is uncorrelated with past samples as seen in the figure. The histogram shows that as in [65] the noise on the residual follows a Cauchy distribution with a general form of

$$p(x; x_o, \beta) = \frac{1}{\pi} \frac{\beta}{(x - x_o)^2 + \beta^2}. \tag{E.40}$$

The GLRT is based on the likelihood ratio between the probability of the two hypotheses given a window of data

$$L_G(\boldsymbol{x}) = \frac{p\left(\boldsymbol{x}; \hat{\boldsymbol{\Theta}}_1\right)}{p\left(\boldsymbol{x}; \hat{\boldsymbol{\Theta}}_0\right)} > \gamma. \tag{E.41}$$

Here $\hat{\boldsymbol{\Theta}}_1$ is the Maximum Likelihood Estimate (MLE) of the parameters given $\mathcal{H}_1$ and $\hat{\boldsymbol{\Theta}}_0$ for the null-hypothesis. If the ratio is larger than a certain threshold γ the hypothesis $\mathcal{H}_1$ is decided. The two parameters of (E.40) are the half-width half-maximum scaling, β, and the offset x_o, respectively. Using this equation the GLRT test statistics become

$$L_G(\boldsymbol{x}) = \frac{\prod_{i=1}^{N} p\left(x_i; \hat{x}_o, \hat{\beta}\right)}{\prod_{i=1}^{N} p\left(x_i; 0, \hat{\beta}\right)} > \gamma. \tag{E.42}$$

The MLEs of $\hat{\beta}$ and $\hat{x}_o$ are found by fitting the data to equation E.40. The window size N is chosen empirically. In [65] the threshold for the detector was found by assuming the performance could be calculated using a χ^2 distribution for the detectors, according to the classical theory [132], [77]. Dong et. al [42] introduced a robust scheme for online fault detection of additive faults on an aircraft when identification errors exist in the model on which FDI is based. Other data driven approaches utilize observations on real data to characterize the distributions of test statistics that are found to differ significantly from the theoretical χ^2 in real applications, see [52] and [48]. This paper follows the latter approach and instead of assuming a χ^2 determined threshold, the distribution of the test statistics, ie the L_G signal, is determined for a large sample of data known to have no observed faults. This makes it possible to provide a reliable estimate of the P_{FA} (probability of false alarms) under $\mathcal{H}_0$. The idea to design tests based on P_{FA} under $\mathcal{H}_0$ was investigated in [140] for a CUSUM test and in [62] for CUSUM and GLRT with χ^2 test statistics.
Fig. E.9 shows the GLRT test statistics for a part of a flight without presence of faults. The data are found to be best fitted using a Weibull distribution

$$P(x; b_w, k_w) = 1 - \exp\left(-\left(\frac{x}{b_w}\right)^{k_w}\right). \tag{E.43}$$

Estimating the scale parameter b_w and shape parameter k_w is straight forward using an MLE or moment estimator method. The threshold γ that will give a desired low false alarm probability is obtained from the estimate of the distribution. The MLE estimates of the parameters for 18 flights are shown in Fig. E.10.
Some flights have a more noisy residual and therefore also a more noisy GLRT response. This is probably because this flight is done at higher altitude and on a

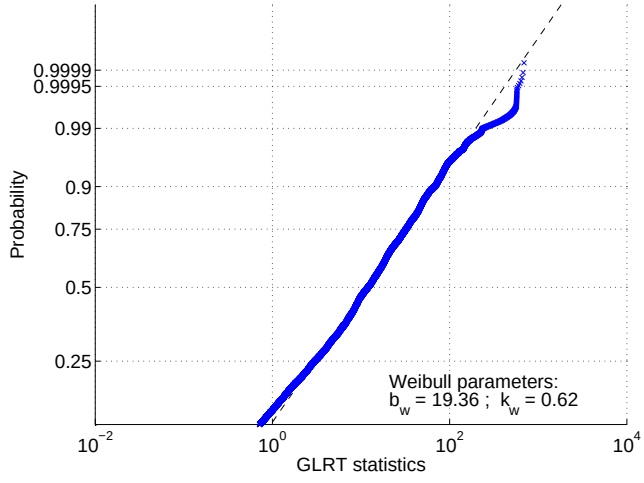

Figure E.9: Probability plots of the GLRT output for the fault free part of a flight.

day with more wind gusts, which doesn't fit well with the constant wind model used in the EKF. The fitted Weibull distribution is used to set the detector threshold. This is done by looking at the right tail distribution $Q(x; b_w, k_w) = 1 - P(x; b_w, k_w)$ to find the probability of exceeding a chosen threshold.
Due to differences the athmospheric conditions as well as differences between aircraft and flight-pattern there is a variation on the distribution parameters. In Fig. E.10 MLEs for the Weibull parameters for 18 different test flights show that the shape parameter k_w is fairly constant among these flights. The scale parameter b_w however, varies with the conditions met during the individual flights. By scaling test statistic data with the estimates of b_w, it is hence possible to get a quite homogeneous set of test statistics data from which a suitable threshold can be found. The right tail probability $Q(x; b_w, k_w) = 1-P(x; b_w, k_w)$ gives the probability of exceeding a chosen threshold. The 0.9999 level in the probability plots give $P_{FA} = 0.0001$.

$$P_{FA} = Q(\gamma; b_w, k_w) \Rightarrow \gamma = b_w \left(-\ln\left(P_{FA}\right)\right)^{\frac{1}{k_w}} . \tag{E.44}$$

With sampling time $T_S \simeq 0.1s$, choosing $\gamma_1 = 3000$ will give a false alarm probability of 0.003% per hour of flight for the data from Fig E.10 ($b_w = 19$ and $k_w = 0.6$). This might even be a conservative choice since data does not follow the Weibull distribution in the high end of the probability plot in Fig. E.9.
The threshold to be selected for a chosen false alarm rate is clearly higher in conditions with high levels of wind turbulence. An alternative to a fixed threshold could be development of an adaptive threshold. This has been done

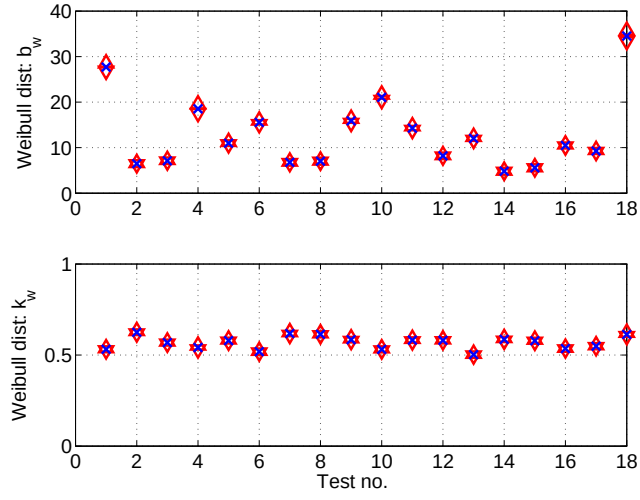

Figure E.10: Maximum likelihood estimates of Weibull parameters for different flights together with 99% confidence boundaries (red arrows).

for CUSUM-like tests and for χ^2 type test statistics in [127]. Similar results are not available for a GLRT and Weibull distributed test statistics.

The residual from (E.35) is treated in a similar way to find parameters for a suitable GLRT detector and a threshold of $\gamma_2 = 100$ is found to give an acceptably low false alarm rate, below 0.003/h for the worst case level of disturbances. If a less conservative calculation was made based on the mean of the Weibull parameters a threshold of $\gamma_i/2$ would give a false alarm rate of around 0.0004/h. The conservative choice of threshold is used because of the large variation between the noise of the different flights makes it too risky to provide with the lower bound.

Since both residual R_1 and R_2 are based on estimators that uses v_{pitot} in their error values, it is important to stop estimation when a fault on v_{pitot} is detected. Each of the estimators are stopped when its corresponding GLRT output reaches a certain fraction of the alarm threshold, a value of $\gamma_i/2$ was used here. Choosing a lower boundary for this than the alarm threshold has two important advantages. First R_3, which is based on the difference of the two estimates, is independent of v_{pitot} some samples before an alarm is triggered such that isolation is possible. Second, the chance of adapting to a faulty state is lower because adaption is stopped sooner after the fault.

E.8.1 Detection Probability

Detection probability P_D is much more difficult to assess than the false alarm probability P_{FA} due to the sparsity of data where faults are present, the $\mathcal{H}_1$ cases. A single recorded case of a pitot sensor fault is available but the duration of the fault is fairly short, since the event caused the UAV to get into uncontrolled conditions that led to a crash. There is no *ground truth* available of when to declare the start of a $\mathcal{H}_1$ condition, so the statistical assessment of P_D that follows is fairly uncertain.

E.8.2 Test statistics for the $\mathcal{H}_1$ case

A portion of data for the faulty case is analyzed in this section. The data belongs to the part where the GLRT detectors chooses hypothesis $\mathcal{H}_1$. Even though the amount of data is small they could give an indication of detection probability given the thresholds chosen from the $\mathcal{H}_0$ data. The data is taken from the point where the fault is first deemed present on the data to three seconds before the first zero crossing of the residual. This slice of data covers the flight where the operator still would able to safe the aircraft and is therefore the most interesting for detection. Fig. E.11 shows a probability plot of the data in this $\mathcal{H}_1$ case for

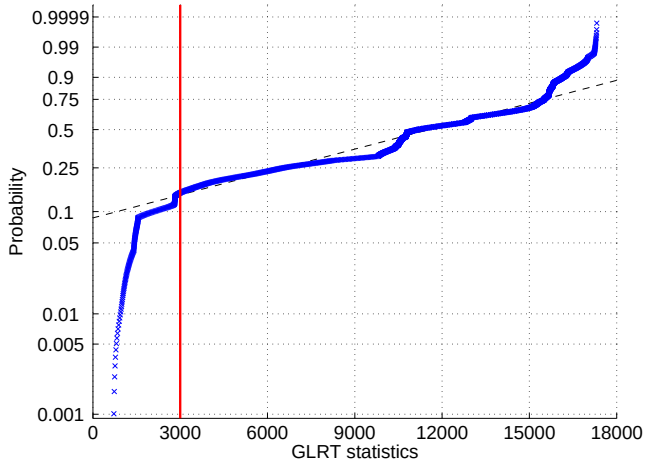

Figure E.11: Plot of the GLRT output in the $\mathcal{H}_1$ case for R_1. The red line indicates the threshold γ_1.

R_1. A Gumbel distribution is fitted to the data and shown in the plot. With the chosen threshold, and the chosen data segment, P_D is 85%. This is very satisfactory considering the noise level on the different measurements.
Another essential aspect is which effect the fault might on the flight envelope and derived from this on the operability and the survivability of the aircraft.

Coverage, the probability of being able to detect and recover from a fault, was treated in [134], and fault masking in [133]. Methods to verify and test for robust performance under different conditions of faults was the subject of [108].
The impact of the airspeed sensor fault is related to the level (magnitude) of faults that could be hidden below a threshold for the GLR tests. If the avionics and aircraft together have robust performance within this level, diagnostic performance could be considered satisfactory.

E.8.3 Detector performance

The detection algorithm is verified by adding a number of artificial faults to real data from flights with similar properties as shown in Fig. E.10. In this way, the actual noise of the system is preserved. The simulated fault is added to the airspeed measurement $v^*_{pitot} = v_{pitot} + f$ and the faulty value v^*_{pitot} is passed on to the detection system. The following fault scenarios were tested. A stepwise fault

$$f = \begin{cases} f = 0 & t < T_f \\ f = A_s & t \geq T_f \end{cases}, \tag{E.45}$$

and ramp fault

$$f = \begin{cases} f = 0 & t < T_f \\ f = s_r t & t \in \left[T_f; T_f + \frac{A_r}{s_r}\right] \\ f = A_r & t > T_f + \frac{A_r}{s_r} \end{cases} \tag{E.46}$$

Faults below a certain magnitude will not be detected as these are considered within the limits of the normal noise and disturbances on the system. The lower limits of what is achievable to detect is reported in Table E.3. Residual R_1 has

Table E.3: Lower limits for detection for R_1 and R_2.

Residual	A_s	A_r	s_r
R_1	6.5 m/s	7.5 m/s	0.50
R_2	4.8 m/s	5.0 m/s	0.35

worse performance than R_2 because a relatively high threshold is needed on this residual to take wind gust into account. To raise the certainty of a fault before an alarm is triggered, both residuals should indicate a $\mathcal{H}_1$ condition before this is actually reported to the operator. The values determined for R_1 are hence those that determine the actual performance of the diagnosis system with fixed threshold. It is seen that a deviation in speed measurement of about 13% need be tolerable by the control system. This appears to be reasonable for practical design.
The minimal time available to detect a fault is also important, however in the setup where the diagnosis system serves as an aid to the UAV operator the reaction time of this operator plays a major role. Practical experiences with

airspeed faults for the Banshee drone indicate that the measurement error on the pitot tube builds up gradually over time as the fault progresses. This means that it takes some time before the fault reaches a level that is critical to the flight of the aircraft, but also that the detection time is longer. A sudden change in value will become critical sooner, but is also easier to detect. Practical experiences have shown that the time elapsed from the fault begins until control of the aircraft is lost is around 200 s. This observation is based on the loss of several drones, presumably caused by airspeed sensor faults, but only one incident was scrutinized in the detail reported here.

E.8.4 Real-time implementation

In order to run the diagnosis online, while flying, the system must be running fast enough to keep up with the telemetry datastream coming from the aircraft at 10 Hz-12 Hz. Since the system is intended to be running on ground and not onboard the aircraft standard PC hardware can be used. The EKF used for wind estimation is a straight forward implementation since the direct expressions for the derivatives are available. The non-linear observer representation must be discretized in order to run on the computer. This is done using a 4th order Runge Kutta method to approximate the differential equations. The heaviest process is generating test statistics used for the GLRT. Finding the MLE for the Cauchy distribution for a window of data is done by optimization. By using the MLE's from the previous data window as initialization parameters for the next data window this can be done at a satisfactory rate. Running the steps of the algorithm at the specified rate is therfore not an issue.
If the system should run onboard the aircraft it might be necessary to decrease systems load since limited processing power is available here. Also the data is available at a higher rate and thereby increasing the load of the algorithm. However since this is not the intended use of this diagnosis system this is not pursued any further.

E.8.5 Detection of real fault

Data from a real incident where the pitot tube gets clogged is used to test the behavior of the detection system. Velocities measured by the pitot tube (airspeed) and the GPS (ground speed) are shown in Fig. E.12. The figure shows that the two measurements follow each other relatively well until around 2140 s into the flight. There is some variation due to the wind and since the aircraft is flying in a square trajectory the effect of this is changing. The aircraft is controlled using airspeed which is why the pitot tube measurement is stable while the GPS velocity fluctuates. Around $t = 2140$ s into the flight a high increase in GPS velocity compared to airspeed is seen. This is where the pitot tube measurement fails. Because the autopilot controls the aircraft as it was flying at its nominal speed a maneuver done around $t = 2333$ s exceeds the flight

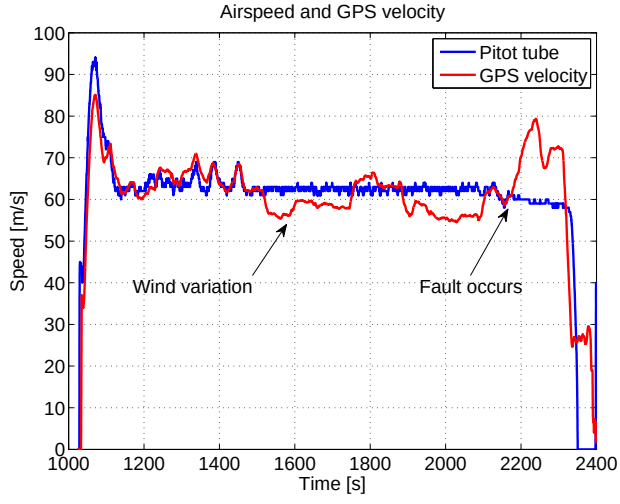

Figure E.12: Airspeed and GPS velocity for a flight where pitot tube clogging occurs.

envelope and control of the aircraft is lost. The operator could have intervened and the aircraft saved had he been made aware that the pitot tube measurement was faulty.

The air data from the aforementioned flight was fed to the diagnosis system. The time development of three residuals described in Table. E.2 is shown in Fig. E.13 with an indication of the faults starting point. As expected a large response is seen on R_1 and R_2 which both triggers an alarm. A small variation is also observed in R_3. This is a consequence of the two airspeed estimators starting running open loop as the airspeed measurement is assessed being faulty. This means that after a while the estimates will diverge.

In Fig. E.14 and E.15 the resulting GLRT output is shown. Fig. E.14 is residual R_1 originating by the wind estimating EKF. Note that the actual flight starts at $t = 1100$ s and the diagnosis is initialized a while after this to allow for estimated parameters to settle. With the chosen threshold detection is done at $t = 2204$ s, which is about 64 s from the first signs of the fault is seen. More importantly this is around 130 s before control over the aircraft is lost and therefore well within the operators reaction time.

In Fig. E.15 the GLRT output and decision signal for R_2, the residual from the observer is shown. As seen the detection happens at $t = 2202$ s and is therefore in the same range as R_1 and well within reasonable time for the operator to react.

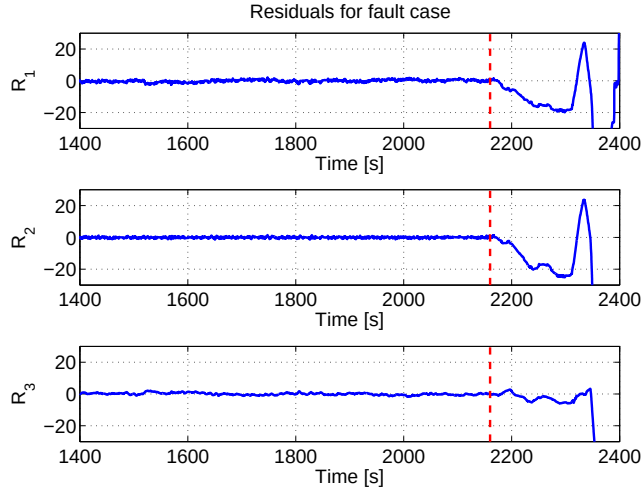

Figure E.13: All three residuals development for the faulty flight data. The vertical dashed line indicate the beginning of the fault.

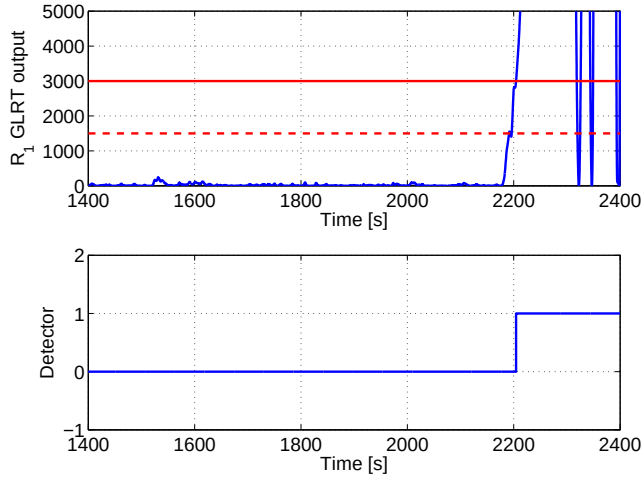

Figure E.14: GLRT output and decision signal from R_1. The alarm is raised at $t = 2204$ s. The solid horizontal line is the threshold for alarms and the dashed line is the threshold for stopping estimation.

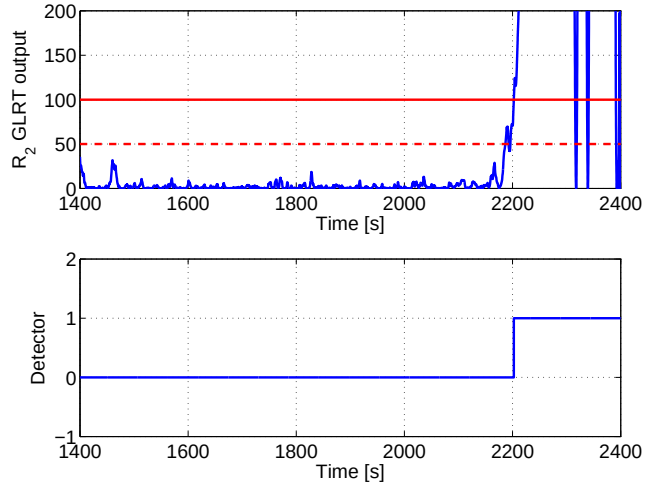

Figure E.15: GLRT output and decision signal from R_2. The alarm is raised at $t = 2202$ s. The solid horizontal line is the threshold for alarms and the dashed line is the threshold for stopping estimation.

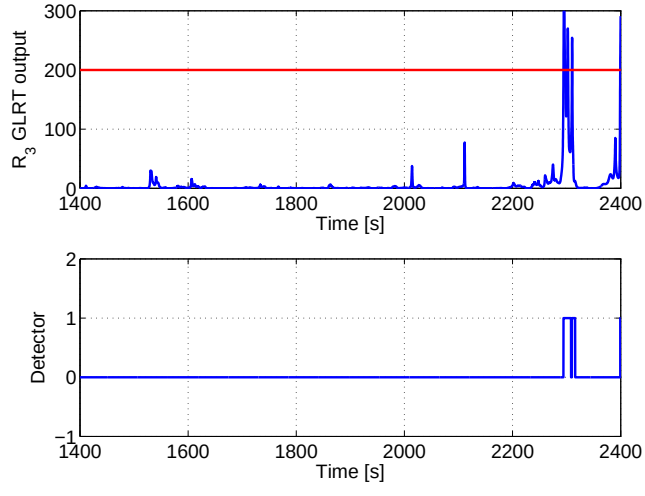

Figure E.16: GLRT output and decision signal from R_3.

E.9 Hypothesis Testing for Reset to Normal

Resetting to normal could be essential for airspeed sensor faults if caused by icing. Testing for return to normal, the $\mathcal{H}_0$ condition is confirmed in a clas-

sical setting when performing a CUSUM sequential test where a hypothesis $\mathcal{H}_0 : \ R_i = \mu_0 + w(k); \quad \mu_0 \leq \mu_{test}$ where μ_{test} is a limit for declaring condition as normal. For GLRT, a test can be made that the test statistics remains below a specified threshold. These standard approaches for confirmation of reset to normal fall short when the aircraft makes maneuvers, when reaching the limits of flight envelope, where faulty readings of speed shortly coincide with the estimates. This is seen in the time-history plots as instants after the fault occurred where residuals cross zero at a certain rate to change sign and the GLRT detector(s) cross the detection threshold.

E.9.1 Residual zero-crossing

This phenomenon is caused by the residual value crossing zero and changing sign. For a short period of time $\mathcal{H}_0$ will be considered true if only the residual is considered. To cope with this issue, the derivative of the residual is also taken into account. The zero crossing is characterized by a high value of the residuals derivative which is different from what would happen if the residual went back to a zero value. The derivative of the residual can be estimated by the slope a straight line approximation over a small window. Doing this moderates the noise influence.
Using least squares regression the derivative estimate over a window of size N is given by

$$\widehat{\dot{R}_1} = \frac{N \sum_{n \in N} t(n) R_1(n) - \sum_{n \in N} t(n) \sum_{n \in N} R_1(n)}{N \sum_{n \in N} t(n)^2 - \sum_{n \in N} t(n) \sum_{n \in N} t(n)}. \tag{E.47}$$

The same expression is used to create $\widehat{\dot{R}_2}$. Combining the derivative with its matching residual in vector form $\boldsymbol{R_1} = \begin{bmatrix} R_1 & \widehat{\dot{R}_1} \end{bmatrix}^{\mathsf{T}}$ gives the desired properties.
The trajectories of R_1 and $\widehat{\dot{R}_1}$ are shown in Fig. E.17 for a time-slice before and after the fault occurs. An ellipsis in the center shows the part of the phase plane to which the signal should be within to be considered fault free.
The vector based detection is only used when the alarm is already raised to make to signal strongly detectable and not sensitive towards residual zero crossings. The vector based setup could be used in detecting faults but the derivative part is very sensitive to noise so the risk of false alarms would be greater. Since the scalar based setup is more robust this is used instead.
In most of the practical cases where a fault is discovered in the airspeed measurement system, the aircraft would be brought down in a controlled manner as quickly as possible. In these cases there is no value of being able to detect whether the system returns to a fault free state or not and therefore a suitable hysteresis curve around the residual would be enough to reject the zero crossings. However, in some cases the fault is due to icing of the pitot tube and

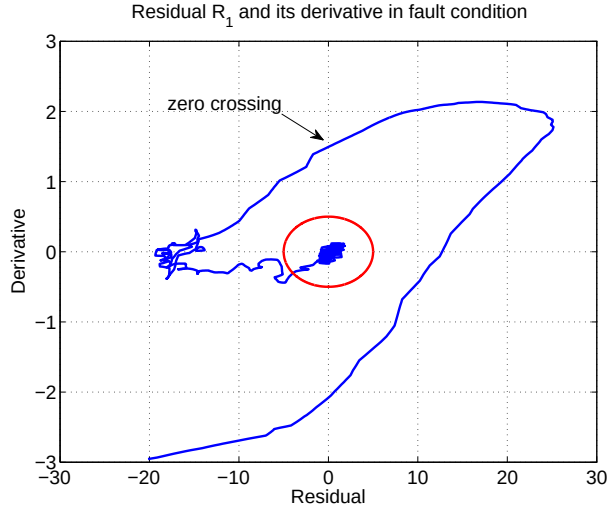

Figure E.17: Residual R_1 versus $\widehat{\dot{R}_1}$. The red ellipsis indicates the boundary of fault free behavior.

reducing the altitude to a warmer level might recover the fault. In this case it is essential to be certain that normal behavior of the airspeed measurement system is restored.
The formal test quantity R_4 is

$$\mathcal{H}_0: \quad R_4 = \left(\frac{R_1}{R_1^t}\right)^2 + \left(\frac{\widehat{\dot{R}_1}}{\dot{R}_1^t}\right)^2 \leq 1, \tag{E.48}$$

where R_1^t and $\dot{R}_1^t$ are the axes of the ellipse constraining the normal operation range in Fig. E.17. A formal change detection test is easily derived for R_4 to confirm return to normal. The condition from this test should be present simultaneously with the $\mathcal{H}_0$ from the GLRTs on R_1 to R_3 to confirm return to normal from an airspeed sensor fault.

E.10 Conclusion

Fault diagnosis of the airspeed measurement system for small fixed wing UAV's was considered in this paper. A diagnosis setup based on standard UAV sensor readings and a basic thrust model were suggested. The setup makes use of ground speed measured by an onboard GPS receiver. Wind speed and direction were estimated to provide one air speed estimate. A non-linear adaptive observer was

employed to estimate the engine's delivered thrust and in turn make a second airspeed estimate.
A hypothesis test based on GLRT was designed using past flight-data recordings, to find detection thresholds to give desired low probability of false alarms. Tuning, in this way, to the physical noise and disturbances on the aircraft, this ensured a very low false alarm rate. Detection probability was analyzed from flight data where a genuine fault occurred and the design based on false alarm probability would give a time history, while the fault persisted, where 85% of the data exceeded the chosen thresholds.
The method was verified both using simulated faults and the real data from an UAV lost due to an airspeed sensor fault. The simulation shows that, with the false alarm rate chosen, that speed sensor faults exceeding 6.5 m/s are guaranteed detectable, which was judged to be an acceptable level that can be handled within robustness limits for conventional autopilot controls. With false alarm rate below 0.003/h with normal wind disturbances, detection of the real life fault was achieved 130 s before radio contact was lost with the aircraft. This time window would leave ample time for the operator to react and bring the aircraft down safely.

E.11 Reference frames

E.11.1 Earth fixed earth centred frame (ECEF)

A right-hand frame with origin at the Earth center. The x-axis is extended through the intersection between the prime-median and Equator and the z-axis points towards the north pole. GPS measurements are given in this system.

Vehicle carried earth frame

Standard North, East, Down system following the air vehicle around on the surface on the earth reference ellipsoid.

Body frame

The axes are coinciding with the aircraft body regardless of attitude and has origin in the aircraft center of mass. The x-axis is forward through the aircraft's nose, the y-axis to the right, and the z-axis pointing out of the belly.

Wind frame

Is centered at the aircraft's center of mass, and has its x-axis along the relative direction of wind. The angle of attack α and the side slip angle β describe a rotation from wind frame to body frame.

E.12 Observer Stability Proof

The lower bound for the observer gain is derived in this section. To start with the gain functions used for the adaptive parameters Θ_{uu} and $\Theta_{uu\alpha}$ are assumed Lipschitz according to the following relations

$$\begin{aligned} \|F_1(u,t) - F_1(\bar{u},t)\| &\leq \gamma_1 \|u - \bar{u}\|, \quad \text{(E.49)} \\ \|F_2(u,t) - F_2(\bar{u},t)\| &\leq \gamma_2 \|u - \bar{u}\|. \quad \text{(E.50)} \end{aligned}$$

The assumptions in (E.49) and (E.50) is valid because the physical values of the aircraft are bounded in the following way

$$\begin{aligned} u &\in [0; u_{max}], \\ \alpha &\in [\alpha_{min}; \alpha_{max}], \\ n &\in [0; n_{max}]. \end{aligned}$$

Applying the expressions for $F_1(u,t)$ and $F_2(u,t)$ in (E.31) the following Lipschitz constants are found

$$\gamma_1 = \tfrac{\varrho S u_{max}}{m}, \quad \gamma_2 = \frac{\varrho S \alpha_{max} u_{max}}{m}. \quad \text{(E.51)}$$

For the observer to be asymptotic stable the error $\tilde{x} = x - \hat{x} = 0$. For this to be true a Lyapunov function $\mathcal{V}(\tilde{x})$ must satisfy theorem 4.8 in [79]. This states that the following must be satisfied.

Uniform asymptotic stability

Let $x = 0$ be an equilibrium point for $\dot{x} = f(x,t)$ and $D \subset \mathbb{R}^n$ be a domain containing $x = 0$. Let $\mathcal{V} : [0; \infty[\times D \to \mathbb{R}$ be a continuously differentiable function such that

$$W_1(x) \leq \mathcal{V}(x,t) \leq W_2(x) \quad \text{(E.52)}$$

and

$$\frac{\partial \mathcal{V}}{\partial t} + \frac{\partial \mathcal{V}}{\partial x} f(x,t) \leq 0, \quad \text{(E.53)}$$

$\forall t \geq 0$ and $\forall x \in D$ where $W_1(x)$ and $W_2(x)$ are continuous positive definite functions on D. Then, $x = 0$ is uniformly asymptotically stable.
The following function is chosen as a Lyapunov function candidate

$$\mathcal{V}(\tilde{\boldsymbol{x}}, t) = \tilde{\boldsymbol{x}}^{\mathrm{T}} \boldsymbol{P} \tilde{\boldsymbol{x}}, \quad \text{(E.54)}$$

where $\boldsymbol{P}$ is a diagonal matrix with trace $[a, b, c]$ where a, b and c are elements of size 1 with units to allow addition of the terms in the quadratic form Eq. E.54. These unit conversion factors are disregarded in the derivation below.

$$\mathcal{V}(\tilde{\boldsymbol{x}}, t) = \tilde{\boldsymbol{x}}^{\mathrm{T}} \tilde{\boldsymbol{x}} = \tilde{u}^2 + \tilde{\Theta}_{uu}^2 + \tilde{\Theta}_{uu\alpha}^2. \quad \text{(E.55)}$$

Choosing the positive definite functions

$$W_1(\tilde{\boldsymbol{x}}) = \tfrac{1}{2}\mathcal{V}(\tilde{\boldsymbol{x}}, t) \qquad \text{and} \qquad W_2(\tilde{\boldsymbol{x}}) = 2\mathcal{V}(\tilde{\boldsymbol{x}}, t),$$

satisfy (E.52). The time derivative of $\mathcal{V}(\tilde{\boldsymbol{x}})$ is zero because no explicit time dependence is present

$$\frac{\partial \mathcal{V}}{\partial t} = 0. \tag{E.56}$$

The state derivative of $\mathcal{V}(\tilde{\boldsymbol{x}})$ is

$$\begin{aligned} \frac{\partial \mathcal{V}}{\partial \tilde{\boldsymbol{x}}} \boldsymbol{f}(\tilde{\boldsymbol{x}}, t) &= \begin{bmatrix} 2\tilde{u} & 2\tilde{\Theta}_{uu} & 2\tilde{\Theta}_{uu\alpha} \end{bmatrix} \boldsymbol{f}(\tilde{\boldsymbol{x}}, t) \\ &= 2\tilde{u}\dot{\tilde{u}} + 2\tilde{\Theta}_{uu}\dot{\tilde{\Theta}}_{uu} + 2\tilde{\Theta}_{uu\alpha}\dot{\tilde{\Theta}}_{uu\alpha}. \end{aligned} \tag{E.57}$$

From this (E.53) becomes

$$2\tilde{u}\dot{\tilde{u}} + 2\tilde{\Theta}_{uu}\dot{\tilde{\Theta}}_{uu} + 2\tilde{\Theta}_{uu\alpha}\dot{\tilde{\Theta}}_{uu\alpha} \leq 0. \tag{E.58}$$

The expression for $\dot{\tilde{u}}$ given in (E.35) was

$$\dot{\tilde{u}} = \left(\frac{T_{nu}n}{m} - L\right)\tilde{u} + F_1(u,t)\Theta_{uu} - F_1(\hat{u},t)\hat{\Theta}_{uu} + F_2(u,t)\Theta_{uu\alpha} - F_2(\hat{u},t)\hat{\Theta}_{uu\alpha} \tag{E.59}$$

Inserting in (E.58)

$$\begin{aligned} 2\tilde{u}\Bigg(\left(\frac{T_{nu}n}{m} - L\right)\tilde{u} + F_1(u,t)\Theta_{uu} - F_1(\hat{u},t)\hat{\Theta}_{uu} \\ + F_2(u,t)\Theta_{uu\alpha} - F_2(\hat{u},t)\hat{\Theta}_{uu\alpha}\Bigg) + 2\tilde{\Theta}_{uu}\dot{\tilde{\Theta}}_{uu} + 2\tilde{\Theta}_{uu\alpha}\dot{\tilde{\Theta}}_{uu\alpha}. \end{aligned} \tag{E.60}$$

This gives

$$\begin{aligned} 2\tilde{u}\Bigg(\left(\frac{T_{nu}n}{m} - L\right)\tilde{u} + F_1(u,t)\Theta_{uu} - F_1(\hat{u},t)\Theta_{uu} + F_2(u,t)\Theta_{uu\alpha} - F_2(\hat{u},t)\Theta_{uu\alpha}\Bigg) \\ + 2\tilde{\Theta}_{uu}\dot{\tilde{\Theta}}_{uu} + 2\tilde{\Theta}_{uu\alpha}\dot{\tilde{\Theta}}_{uu\alpha} + 2\tilde{u}F_1(\hat{u},t)\tilde{\Theta}_{uu} + 2\tilde{u}F_2(\hat{u},t)\tilde{\Theta}_{uu\alpha} \\ \leq 2\tilde{u}\left(\left(\frac{T_{nu}n}{m} - L\right)\tilde{u} + \gamma_1\|\tilde{u}\|\max\left(\|\Theta_{uu}\|\right) + \gamma_2\|\tilde{u}\|\max\left(\|\Theta_{uu\alpha}\|\right)\right). \end{aligned} \tag{E.61}$$

As seen above having the adaptive gains as functions F_1 and F_2 as suggested in [34] simplifies the derivation significantly. The above equation should according to (E.53) be compared to

$$\begin{aligned} 2\tilde{u}\left(\left(\frac{T_{nu}n}{m} - L\right)\tilde{u} + \gamma_1\|\tilde{u}\|\max\left(\|\Theta_{uu}\|\right) + \gamma_2\|\tilde{u}\|\max\left(\|\Theta_{uu\alpha}\|\right)\right) \leq \\ 2\tilde{u}^2\left(\frac{T_{nu}n}{m} - L + \gamma_1\max\left(\|\Theta_{uu}\|\right) + \gamma_2\max\left(\|\Theta_{uu\alpha}\|\right)\right) \leq \\ \frac{T_{nu}n}{m} - L + \gamma_1\max\left(\|\Theta_{uu}\|\right) + \gamma_2\max\left(\|\Theta_{uu\alpha}\|\right) \leq 0. \end{aligned} \tag{E.62}$$

From this it is seen that the gain L should satisfy the following inequality in order for the observer to be uniform asymptotically stable

$$L \geq \frac{T_{nu} n_{max}}{m} + \gamma_1 \max\left(\|\Theta_{uu}\|\right) + \gamma_2 \max\left(\|\Theta_{uu\alpha}\|\right). \tag{E.63}$$

Inserting the maximum value for the worst case the gain ends up being

$$L \geq \frac{T_{nu} n_{max} + \varrho S u_{max} \left(\max\left(\|\Theta_{uu}\|\right) + \alpha \max\left(\|\Theta_{uu\alpha}\|\right)\right)}{m}. \tag{E.64}$$

The derivation above also holds for the case where $\Theta_{uu\alpha} = 0$.

Paper F

A Low-complexity Actuator Fault-tolerant Flight Controller for Unmanned Aircraft[1]

Pierre de Lamberterie, Søren Hansen, Tristan Perez and Mogens Blanke

Abstract

This paper presents a low-complexity actuator fault-tolerant flight controller for Unmanned Aircraft (UA). We propose a design for joint control allocation and motion control scheme whereby the actuator configuration is used to map actuator constraints into the space of the aircraft generalised forces. This allows one to constrain the output of the controller and consider an unconstrained allocation problem since the controller always outputs feasible commands. The controller is combined with a diagnosis system, which informs the controller about actuator faults so it can adjust the constraints and trigger the re-configuration of the allocation problem. The fault diagnosis includes fault detection and isolation. The detection is done by injecting a signal in the null space of the actuator configuration matrix. With such signal, the motion of the UA is undisturbed unless there is a fault. The detection is achieved using statistical analysis of residuals between the output of an estimated model and the aircraft as well as changes in the parameters of the estimated model. This redundancy allows a simplified tuning of the detection thresholds. The performance of the fault-tolerant controller is tested by simulating an UA experiencing a fault during the approach to landing.

[1]Submitted to IEEE Transactions on Aerospace and Electronic Systems.

F.1 Introduction

One of the primary desired attributes of unmanned aircraft (UA) is robust autonomy, namely, the ability of an autonomous system to either continue its operation in the presence of faults or safely shut down [105]. Robust autonomy encapsulates the reliability of the UA physical platform and components plus the ability of autonomous decision making—to varying degrees—in relation to guidance, navigation, and control. One of the enabling factors for attaining high-levels of robust autonomy is the use of Fault-Tolerant Flight Control Systems (FT-FCS); that is flight controllers that can detect and isolate faults and trigger a motion controller reconfiguration to accommodate the fault [19].

A review of different proposals for fault-tolerant-flight controls (FTFC) of piloted aircraft can be found in the study for a benchmark problem in [47] and references there in, where different methods are analysed: observer-based design, on-line parameter estimation, sliding mode with control allocation, adaptive model following control, predictive control with non-linear inversion. The nature of FTFC in UA is different from that of piloted aircraft because of constraints on payload, which often lead to limits in actuator and sensor physical redundancy and higher degrees of autonomy in decision making. A state of the art in fault tolerance of UA flight control has been reviewed in [44], and a proposal based on multiple model adaptive estimation techniques combined with a controller design via dynamic inversion was put forward. Another recent design for the Aerosonde UA was studied in [14]. The latter work also focuses on actuator fault handling. The diagnosis system is designed with a bank of unknown input decoupled functional observers in combination with an active diagnosis method. Once the fault is diagnosed, an FTC based on state feedback controllers aims at establishing the stability domain with respect to the flight envelope and actuator limits while setting the dynamics of the desired closed-loop system.

This paper considers a low-complexity flight controller for Unmanned Aerial Vehicles (UAVs) that handles actuator faults based on the controller proposed in [107]. This design consists of a joint motion controller and control allocation scheme whereby the actuator configuration is used to map actuator constraints into the space of the aircraft generalised forces. The allocation is a simplified version of the method proposed in [45]. The mapping of the constraints to the space of generalised momenta can result in a reduction of the maximum admissible momenta that can be generated. This shortcoming. however, is compensated by the fact that the proposed control solution presents low-computational complexity and robust closed-loop stability. The motion controller is then designed using a particular anti-windup configuration to handle the constraints; and therefore, only feasible commands are passed on to the control allocation function. This serves two purposes. First, the motion controller is informed about the current actuator configuration of the system and the constraints. Second, since the demands of the controller are always feasible, the allocation problem can be

posed as an unconstrained optimisation. The traditional practice for control allocation considers a constrained optimisation problem in the space of actuator commands, which requires on-line numerical optimisation—see [23, 66, 111, 44]. Furthermore, it requires *ad hoc* strategies to inform the motion controller about changes in the constraints. This is handled automatically in our proposed solution.

The proposed flight control system is combined with a diagnosis system that informs the controller about actuator faults so it can adjust the constraints and trigger the re-configuration of the allocation. A model-based diagnosis scheme using low-complexity aircraft models with parameter adaptation is used. The diagnosis scheme is based on [64], and it incorporates fault detection and isolation. The detection is done by injecting a signal in the null space of the actuator configuration matrix. With such signal, the motion of the UA is undisturbed unless there is a fault. The detection is achieved using statistical analysis of residuals between the output of an estimated model and the real aircraft as well as changes in the parameters of the estimated model. This redundancy allows a simplified tuning of the detection thresholds. Once a fault is detected a dedicated test signal is used to isolate the fault. The performance of the proposed controller is tested by simulating an UA experiencing a fault during the approach to landing.

The rest of the paper is organised as follows. Section F.2 summarises the notation and introduces the aircraft non-linear mathematical model used in the simulations. Section F.3 discusses the motion controller and control allocation designs. Section F.4 introduces the fault detection and diagnosis schemes. Section F.5 presents a simulation case study, and Section F.6 concludes the paper.

F.2 Notation and Aircraft model

The dynamics of an UAV is described using a flat-Earth model [122, 142]. The equations of motion are formulated in body-fixed coordinates at the centre of mass CM, and a kinematic model based on quaternions, with $\boldsymbol{\nu}$ being generalised velocities and $\mathbf{q}$ being the quaternion representation of aircraft attitude:

$$ {}^{n}\dot{\mathbf{p}}^{n}_{CM/O} = \mathbf{J}(\mathbf{q})\,\boldsymbol{\nu}, \tag{F.1} $$

$$ \dot{\mathbf{q}} = \mathbf{Q}(\boldsymbol{\nu})\,\mathbf{q}, \tag{F.2} $$

$$ \mathbf{M}\dot{\boldsymbol{\nu}} + \mathbf{C}(\boldsymbol{\nu})\boldsymbol{\nu} = \boldsymbol{\tau}_G(\mathbf{q}) + \boldsymbol{\tau}_P(X_T, Q_P) + \boldsymbol{\tau}_A(\boldsymbol{\nu}, \mathbf{v}^n_w, \boldsymbol{\delta}), \tag{F.3} $$

where $\boldsymbol{\tau}_G$ is generalised gravity force, $\boldsymbol{\tau}_P$ is propeller forces and moments and $\boldsymbol{\tau}_A$ generalised aerodynamic forces. The $\mathbf{M}$ and $\mathbf{C}$ are mass and Coriolis-Centripetal matrices, respectively. With m being mass of the aircraft, $\mathbf{I}^b_{CM}$ the inertia matrix in body coordinates, and $\mathbf{S}(\cdot)$ is the skew-symmetric operator representing the vector product, they are given by

$$ \mathbf{M} = \begin{bmatrix} m\mathbf{I}_{3\times 3} & \mathbf{0} \\ \mathbf{0} & \mathbf{I}^b_C \end{bmatrix}, \qquad \mathbf{C}(\boldsymbol{\nu}) = \begin{bmatrix} m\mathbf{S}(\boldsymbol{\nu}_2) & \mathbf{0} \\ \mathbf{0} & -\mathbf{S}(\boldsymbol{\nu}_2)\,\mathbf{I}^b_{CM} \end{bmatrix}. $$

The control input is the vector $\boldsymbol{\delta}$ of normalised actuator commands: δ_{ar} - right aileron, δ_{al} - left aileron, δ_{er} - right elevator, δ_{el} - left elevator and δ_r - rudder and δ_T - the engine's throttle position. For the ailerons, elevators and rudder a positive deflection produces a negative moment. The normalised deflections of the control surfaces take values within $[-1, 1]$ and thrust command δ_T within [0,1]. Table F.1 summarises the notation.

Table F.1: Summary of aircraft motion variables.

Variable	Name	Frame
$\boldsymbol{\nu} = [({}^n\dot{\mathbf{p}}^b_{CM/O})^\mathsf{T}, (\boldsymbol{\omega}^b_{b/n})^\mathsf{T}]^\mathsf{T}$	Generalised velocity	Body
$\mathbf{q} = [q_0, q_1, q_2, q_3]^\mathsf{T}$	Unit quaternions	-
N	North position of CM	Earth
E	East position of CM	Earth
D	Down position of CM	Earth
ϕ	Roll angle	-
θ	Pitch angle	-
ψ	Yaw angle	-
u	Longitudinal speed	Body
v	Lateral speed	Body
w	Normal (down) speed	Body
p	Roll rate	Body
q	Pitch rate	Body
r	Yaw rate	Body
$\mathbf{p}^n_{CM/O} = [N,\ E,\ D]^\mathsf{T}$	Position	Earth
${}^n\dot{\mathbf{p}}^b_{CM/O} = [u,\ v,\ w]^\mathsf{T}$	Linear-velocity	Body
$\boldsymbol{\Theta} = [\phi, \theta, \psi]^\mathsf{T}$	Euler-angle vector	-
$\boldsymbol{\omega}^b_{b/n} = [p, q, r]^\mathsf{T}$	Angular-velocity	Body
n	propeller rotational speed	Body
$\boldsymbol{\tau} = [(\mathbf{F}^b)^\mathsf{T}, (\mathbf{T}^b)^\mathsf{T}]^\mathsf{T}$	Generalised Force	
$\mathbf{F}^b = [X, Y, Z]^\mathsf{T}$	Forces	Body
$\mathbf{T}^b = [L, M, N]^\mathsf{T}$	Torques	Body
X	Longitudinal Force component	Body
Y	Lateral Force component	Body
Z	Normal Force component	Body
L	Roll torque component	Body
M	Pitch torque component	Body
N	Yaw torque component	Body
α	angle of attack	-
β	sideslip angle	-
$\mathbf{v}^n_w$	Wind velocity	Earth
$\boldsymbol{\delta}_a = [\delta_{ar}, \delta_{al}, \delta_{er}, \delta_{el}, \delta_r, \delta_T]$	actuator commands	-

The kinematic model is

$$\begin{aligned} {}^n\dot{\mathbf{p}}^n_{C/O} &= \mathbf{J}(\mathbf{q})\,\boldsymbol{\nu}, \\ \dot{\mathbf{q}} &= \mathbf{Q}(\boldsymbol{\nu})\,\mathbf{q} \end{aligned} \tag{F.4}$$

where

$$\mathbf{J}(\mathbf{q}) = \begin{bmatrix}\mathbf{C}_b^n(\mathbf{q}) & \mathbf{0}\end{bmatrix}$$

and $\mathbf{C}_b^n(\mathbf{q})$ is the standard orthogonal coordinate transformation matrix that converts vectors in the body frame $\{b\}$ to the navigation frame $\{n\}$: $\mathbf{a}^n = \mathbf{C}_b^n(\mathbf{q})\mathbf{a}^b$.
The quaternion transformation in (F.4) is given by

$$\begin{bmatrix}\dot{q}_0\\ \dot{q}_1\\ \dot{q}_2\\ \dot{q}_3\end{bmatrix} = \frac{1}{2}\begin{bmatrix}0 & -p & -q & -r\\ p & 0 & r & -q\\ q & -r & 0 & p\\ r & q & -p & 0\end{bmatrix}\begin{bmatrix}q_0\\ q_1\\ q_2\\ q_3\end{bmatrix}. \tag{F.5}$$

Further details of aircraft kinematics can be found in [122, 142].

The later analysis requires a notation and some comments on generalised forces $\boldsymbol{\tau}_G, \boldsymbol{\tau}_P$ and $\boldsymbol{\tau}_A$. The forces from gravity and propulsion are given by,

$$\boldsymbol{\tau}_G = \begin{bmatrix}-mg\sin\theta & mg\sin\phi\cos\theta & mg\cos\phi\cos\theta & 0 & 0 & 0\end{bmatrix}^T, \tag{F.6}$$

and

$$\boldsymbol{\tau}_P = \begin{bmatrix}X_T & 0 & 0 & Q_T & 0 & 0\end{bmatrix}^T. \tag{F.7}$$

The generalised aerodynamic forces are commonly described by a set of dimensionless coefficients relating the current state of the aircraft to the forces and torques working on it,

$$\boldsymbol{\tau}_A = \begin{bmatrix}\bar{q}S(C_X(\alpha,\beta)\cos\alpha\cos\beta - C_Y(\beta)\sin\beta\cos\alpha - C_Z(\alpha)\sin\alpha)\\ \bar{q}S(C_X(\alpha,\beta)\sin\beta + C_Y(\beta)\cos\beta)\\ \bar{q}S(C_X(\alpha,\beta)\sin\alpha\sin\beta - C_Y(\beta)\sin\alpha\sin\beta + C_Z(\alpha)\cos\alpha)\\ \bar{q}SbC_L(\delta_{ar},\delta_{al},\delta_{er},\delta_{el},p,r,\beta)\\ \bar{q}S\bar{c}C_M(\delta_{ar},\delta_{al},\delta_{er},\delta_{el},q,\alpha)\\ \bar{q}SbC_N(\delta_{ar},\delta_{al},\delta_{er},\delta_{el},\delta_r,r,\beta)\end{bmatrix}. \tag{F.8}$$

The aerodynamic torque coefficients can be approximated using the following expansion in aerodynamic derivatives[2],

$$\begin{aligned}
C_L &= C_{Lar}\delta_{ar} + C_{Lal}\delta_{al} + C_{Ler}\delta_{er} + C_{Lel}\delta_{el}\\
&+ C_{L\tilde{p}}\tilde{p} + C_{L\tilde{r}}\tilde{r} + C_{L\beta}\beta,\\
C_M &= C_{Mar}\delta_{ar} + C_{Mal}\delta_{al} + C_{Mer}\delta_{er} + C_{Mel}\delta_{el}\\
&+ C_{M\tilde{q}}\tilde{q} + C_{M\alpha}\alpha,\\
C_N &= C_{N\delta_r}\delta_r + C_{N\tilde{r}}\tilde{r} + C_{N\beta}\beta,
\end{aligned} \tag{F.9}$$

[2]This model corresponds to a particular aircraft [44], and different aircraft may require different terms.

where

$$\tilde{p} = \frac{bp}{2V_T}, \qquad \tilde{q} = \frac{\bar{c}q}{2V_T}, \qquad \tilde{r} = \frac{br}{2V_T}. \tag{F.10}$$

The constant parameters b and $\bar{c}$ are the wing span and mean cord respectively. The nonlinear equations of motion are commonly linearised to obtain a linear parameter-varying (LPV) model for controller design and performance analysis, with air speed V being the essential parameter that scales the dynamics [122] and other parameters Θ giving rise to model uncertainty. Such input-output description in the Laplace domain will have the form,

$$\omega^b_{b/n}(s) = \mathbf{H}_{\omega\delta}(s|V,\Theta)\delta_a(s) + \mathbf{H}_{\omega d}(s|V,\Theta)\mathbf{d}(s), \tag{F.11}$$

where δ_a is control input, $\mathbf{d}$ disturbance from wind turbulence etc, and s the complex frequency.

F.3 Flight Control System with Control Allocation

Figure F.1 shows the overall structure of the fault-tolerant flight control and guidance system. This includes guidance, motion control and fault-diagnosis.

F.3.1 Guidance

The guidance sub-system generates a smooth path through a set of way-points and uses this as reference for the UAV. Polynomial interpolation (cubic spline) is used and the path is projected to the horizontal and vertical plane of the earth frame. A target air-speed is set for the mission and the desired heading angle and altitude are determined by a line-of-sight algorithm that projects the current aircraft position onto the desired path. The lateral guidance determines the desired yaw angle based on a point at a fixed length L forward along the path. Similarly, the vertical guidance determines the desired altitude. This is illustrated in Figure F.2. The guidance law is an adaptation of that proposed in [67].

F.3.2 Motion Controller

Figure F.3 shows a block diagram describing the motion controller and control allocation with the associated input and output variables. The controller has three channels: vertical position, air-speed, and horizontal position. The vertical controller shown, in Figure F.4-a, takes as an input a commanded altitude h_c, which is provided by the guidance system. The altitude error is processed by the controller $C_h(\cdot)$, which is a proportional plus integral controller—the integral component provides the aircraft trim. The output of the altitude controller is the pitch angle command θ_c, which is then used by a pitch controller, which provides augmented stability and integral action. The pitch-loop controller is

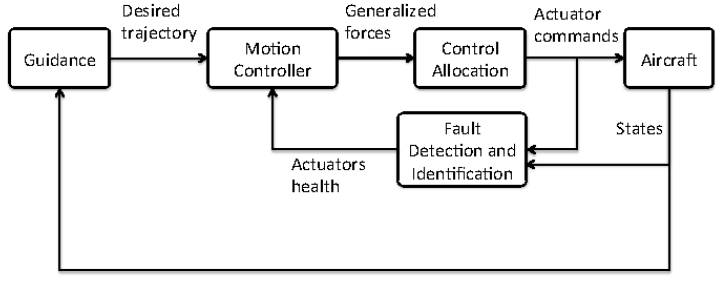

Figure F.1: Global architecture of the FT-FCS.

a proportional controller with gain K_θ, and the pitch-rate controller $C_q(\cdot)$ is a proportional plus integral controller implemented with anti-windup, as discussed in Section F.3.5. The output of the vertical controller is the desired pitch moment command M_c. The air-speed controller takes as an input a commanded air speed V_{Tc}, which is provided by the guidance system. This controller has a similar structure as the pitch controller, modulo substitution of θ by V_T and q by u. The output of this controller is the desired thrust command X_c.
The horizontal controller shown in Figure F.4-b takes as an input a desired heading angle commanded ψ_c, which is provided by the guidance system. For a level flight, $\theta \approx 0$, a perfect coordinate turn leads to a yaw rate and bank angle relation that can be approximated as follows [122] (p 190):

$$\dot{\psi} \approx \frac{g}{V_T}\phi. \tag{F.12}$$

The above relation motivates the horizontal controller shown in Figure F.4-b, the heading error is used to generate a banking angle command ϕ_c, which is then used by a roll controller, which provides augmented stability and integral action to the three nested loops. The horizontal controller has a proportional controller for the roll loop and proportional plus integral controller for roll rate loop. The latter controller is implemented with anti-wind up, as discussed in Section F.3.5. The error in roll rate can be used with a proportional controller to generate the desired command of yaw moment—this may be necessary for

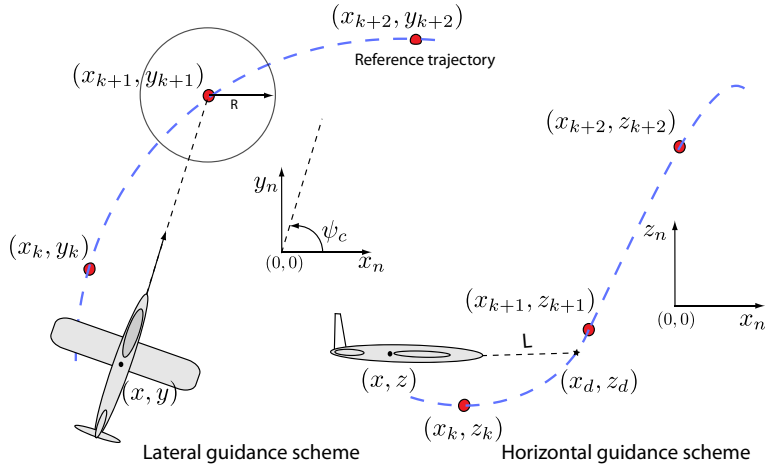

Figure F.2: Lateral and vertical guidance scheme.

initiating the turns for some aircraft. The output of the longitudinal controller are the desired roll and yaw moment commands M_c and N_c, which are then used by the control allocation.

F.3.3 Control Allocation

Speed Control - Unconstrained

The control allocation of the thrust can be decoupled from the remaining degrees of freedom. For an aircraft with a propeller of diameter D, the following thrust model can be used to relate the engine speed $n = n_{max}\delta_T$ (rps) to the thrust [115] (p381):

$$X_T = \rho n^2 D^4 C_T, \tag{F.13}$$

where C_T is the thrust coefficient. The motion of the propeller rotation induces a reaction torque in roll on the aircraft. The induced torque could be assessed by $Q_T = (2\pi)^{-1} \rho n^2 D^5 C_P$ where C_P is the propeller power coefficient, but this torque is considered a disturbance in roll torque and is handled by closed loop operation of the attitude control loops. Tables showing values for C_P ad C_T can be found in classical NACA test results [83]. Expression (F.13) can be inverted to obtain the desired engine speed n given the desired thrust X_{Tc} demanded by the motion controller. This provides the control allocation for thrust. Integral action in the speed controller rejects low-frequency disturbances and provides robustness to low-frequency model uncertainty.

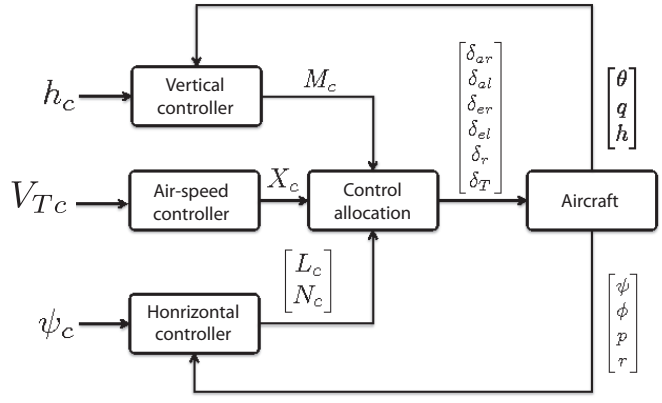

Figure F.3: Architecture of the autopilot control system including control allocation.

F.3.4 Attitude Control - Unconstrained

For control of attitude, three torques need be allocated through a vector of control surface commands

$$\boldsymbol{\delta} = \begin{bmatrix} \delta_{ar} & \delta_{al} & \delta_{er} & \delta_{el} & \delta_r \end{bmatrix}^T. \tag{F.14}$$

Then these variables are related to the torques via an actuator configuration matrix $\mathbf{B}$:

$$\mathbf{T}_c = \mathbf{B}\,\boldsymbol{\delta}, \tag{F.15}$$

where the torque vector is

$$\mathbf{T}_c = \begin{bmatrix} L_c & M_c & N_c \end{bmatrix}^T. \tag{F.16}$$

In order to generate a full torque vector, the matrix $\mathbf{B}$ in (F.15) need to have row rank 3, i.e. the three singular values of $\mathbf{B}$ must all be non-zero. Certain faults will have the effect that the full torque vector can not be generated. In this event, $\mathbf{B}$ has row rank equal to the number of torque vector elements that can be allocated and $\mathbf{B}$ is replaced by $\mathbf{B}_f$, the allocation matrix for the faulty system. This procedure is detailed below.

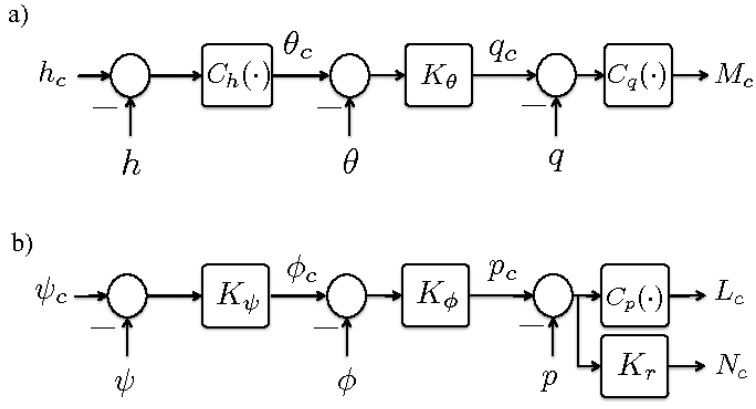

Figure F.4: Detail of the autopilot control channels.

Using the relations given in (F.9) the components related to the control surfaces are,

$$\mathbf{B} = \bar{q}S \begin{bmatrix} b\,C_{Lar} & b\,C_{Lal} & b\,C_{Ler} & b\,C_{Lel} & 0 \\ \bar{c}\,C_{Mar} & \bar{c}\,C_{Mal} & \bar{c}\,C_{Mer} & \bar{c}\,C_{Mel} & 0 \\ 0 & 0 & 0 & 0 & b\,C_{N\delta_r} \end{bmatrix}. \tag{F.17}$$

If one out of m control surfaces should become defect, say number i, the $\mathbf{B_f}$ matrix available for control allocation is

$$\mathbf{B_f} = [\mathbf{b_1}, \ldots \mathbf{b_{i-1}}, \mathbf{b_{i+1}}, \ldots \mathbf{b_m}], \tag{F.18}$$

where $\mathbf{b_j}$ is the j^{th} column of $\mathbf{B}$. After such reduction of the allocation matrix, the row rank is re-calculated and any zero row discarded. The $\mathbf{B}$ matrix used in the sequel is always the $\mathbf{B}_f$ matrix if an actuator fault has been isolated. The set of possible $\mathbf{B}_f$ matrices is small and is easily pre-computed for each of the possible faults.
Since $\boldsymbol{\delta}$ in general has more components than $\mathbf{T}_c$, a number of vectors $\boldsymbol{\delta}$ can satisfy (F.15) for a given value of $\mathbf{T}_c$. In order to limit the number of solutions, one can pose an optimisation problem, given by,

$$\begin{aligned} &\boldsymbol{\delta}^* = \arg\min_{\boldsymbol{\delta}}(\boldsymbol{\delta}^T \mathbf{W} \boldsymbol{\delta}) \\ &\text{subject to } \mathbf{T}_c = \mathbf{B}\boldsymbol{\delta}. \end{aligned} \tag{F.19}$$

The objective function $\boldsymbol{\delta}^T \mathbf{W} \boldsymbol{\delta}$ is representative of total control effort and also of the drag induced by the control surfaces. The matrix $\mathbf{W}$ is positive definite and weighs the relative use of the different actuators. Thus, the control allocation seeks the solution that implements the desired torque vector $\mathbf{T}_c$ whilst

minimising the control effort. The solution to the problem above is given by

$$\boldsymbol{\delta}^* = \mathbf{B}^\dagger \, \mathbf{T}_c, \tag{F.20}$$

where

$$\mathbf{B}^\dagger = \mathbf{W}^{-1}\mathbf{B}^T(\mathbf{B}\mathbf{W}^{-1}\mathbf{B}^T)^{-1}. \tag{F.21}$$

This result is verified by insertion into (F.14). The matrix $\mathbf{B}$ and its right inverse $\mathbf{B}^\dagger$ can be pre-computed. Therefore, the allocation function reverts to implementing (F.20), and there is no need to use numerical optimisation to solve (F.19). The use of control allocation offers the possibility of UAS fault accommodation in the case of actuator failure provided that the vehicle remains fully-actuated after the failure. Should this be the case, one can switch the actuator configuration matrix $\mathbf{B}$ and its pseudo-inverse $\mathbf{B}^\dagger$.

The optimisation problem (F.19) does not take into account the fact that the vector $\boldsymbol{\delta}$ must belong to a constraint set due to the maximum angles of the different surfaces can be deflected. The limits are not usually reached during standard manoeuvres of a healthy aircraft, but in the case of actuator failures and re-allocation of the remaining healthy actuators, saturation can occur. Adding a constraint for $\boldsymbol{\delta}$ into (F.19) requires on-line numerical optimisation, and the solution (F.20) is no longer the optimal solution. Constrained numerical optimisation brings out time-feasibility issues since the optimisation algorithm must always provide a feasible solution within the required sampling period [111]. An alternative to this approach is to constrain the desired torque vector $\mathbf{T}_c$ at the motion control level such that the constraints on $\boldsymbol{\delta}$ always are satisfied [106]. By doing so, the motion controller is also informed about reaching constraints, which prevents performance degradation due to the combination of actuator saturation and integral action. This control method is described in the next section.

F.3.5 Constrained Control

One key issue in systems that require integral action and present a potential for actuator saturation is that of integrator windup. If the actuators saturate, the standard integral controller will continue integrating the error signals even though the control action is not seen by the system. This often produces a degradation of performance in terms of undesirable oscillations and even instability. Control schemes that deal with this effect are called anti-windup schemes [18]. If a linear scalar controller $C(s)$ with input e and output u, $u(s) = C(s)e(s)$, is minimum phase and bi-proper (as in the case of PI and PID controllers), then anti-windup can be achieved simply by implementation shown in [56]. This implementation is illustrated in Figure F.5, where $L(\cdot)$ represents a saturation function, which can have memory and thus be a magnitude saturation, rate

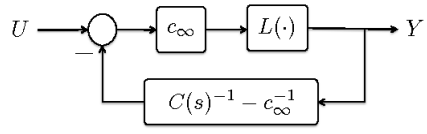

Figure F.5: Anti-windup implementation of a scalar minimum phase and bi-proper controller.

saturation, or a combination of both. The gain c_∞ is the high-frequency gain of the controller

$$c_\infty = \lim_{s\to\infty} C(s), \tag{F.22}$$

which is non-zero because the controller is bi-proper.
If the saturation is not active, the loop of Figure F.5, reduces the controller to:

$$C(s) = \left[1 + c_\infty \left(C(s)^{-1} - c_\infty^{-1}\right)\right]^{-1} c_\infty. \tag{F.23}$$

When the limitation becomes active, it prevents the control signal Y from exceeding its limits, and this constrained signal drives the states of the controller, which are all on the feedback path. It can be shown that the anti-windup implementation shown in Figure F.5 is equivalent to conditioning the input U such that the output of the controller stays at saturation once saturation is reached [56]. The main advantage of the scheme shown in Figure F.5 is that once the controller $C(s)$ is designed, the anti-windup is simply an implementation; it does not require the tuning of any additional gains or filters.

The anti-windup implementation shown in Figure F.5 can be extended to the multivariable case of velocity control loops of the aircraft longitudinal and lateral controllers. Due to the structure of the proposed controllers, the only components that require anti-windup are the roll and pitch—see Figure F.4. We can define the multivariable controller

$$\begin{bmatrix} L_c \\ M_c \end{bmatrix} = \mathbf{C}(s) \begin{bmatrix} p \\ q \end{bmatrix}$$

where

$$\boldsymbol{C}(s) = \begin{bmatrix} C_p(s) & 0 \\ 0 & C_q(s) \end{bmatrix}, \tag{F.24}$$

where $C_p(s)$ and $C_q(s)$ are the roll and pitch rate PI controllers that implement the velocity feedback loops—see Figure F.4. Each of these controllers are of the form

$$C_p(s) = K_p^p \frac{T_I^p s + 1}{T_I^p s}, \qquad C_q(s) = K_p^q \frac{T_I^q s + 1}{T_I^q s}. \tag{F.25}$$

Because of these particular forms $\mathbf{c}_\infty$ and $\mathbf{C}(s)^{-1}$ are well defined.
The main issue here is to find the appropriate multi-variable limiting function

$\mathbf{L}(\cdot)$ that reflects the saturation of the different actuators. This function is related to a constraint set that the actuators define in the space of the generalised control forces via the actuator configuration matrix. If this constraint set is used in the anti-windup implementation, then the control allocation can be considered within an unconstrained optimisation framework since the command $\mathbf{T}_d$ demanded by the controller will always be feasible. Therefore, this approach allows both informing the controller about saturation, and also simplifying the control allocation problem since it can be considered unconstrained.
In order to constrain $\mathbf{T}_c$ we need to construct a set $\mathcal{T}$ such that

$$\mathbf{T}_c \in \mathcal{T} \;\Leftrightarrow\; \boldsymbol{\delta} \in \mathcal{D}, \tag{F.26}$$

where the set $\mathcal{D}$ is defined by the constraints of the actuators.
One way of enforcing these constraints is by computing an unconstrained controller torque $\mathbf{T}_c^u$ and then down scale this so the corresponding actuator configuration stays on the boundary of the set, that is

$$\mathbf{T}_c = \begin{cases} \mathbf{T}_c^u & \text{if } \mathbf{B}^\dagger \mathbf{T}_c^u \in \mathcal{D} \\ \zeta \mathbf{T}_c^u & \text{if } \mathbf{B}^\dagger \mathbf{T}_c^u \notin \mathcal{D} \end{cases} \tag{F.27}$$

where $0 < \zeta < 1$ is determined such that

$$\mathbf{B}^\dagger \, \zeta \, \mathbf{T}_c^u \in \mathcal{D}.$$

By scaling the vector $\mathbf{T}_c^u$, we preserve its direction. This provides a better solution than simply saturating each individual component [56].
If $\mathcal{D}$ is a convex polytope, a geometric convex object with flat sides, then the computation of the scaling gain is straight forward [116]. Let

$$\mathcal{D} = \{\boldsymbol{\delta} : \mathbf{L} < \boldsymbol{\delta} < \mathbf{U}\}, \tag{F.28}$$

or alternatively,

$$\mathcal{D} = \{\boldsymbol{\delta} : \mathbf{F}\,\boldsymbol{\delta} \leq \mathbf{f}\}, \quad \mathbf{F} = \begin{bmatrix} \mathbf{I} \\ -\mathbf{I} \end{bmatrix}, \quad \mathbf{f} = \begin{bmatrix} \mathbf{U} \\ -\mathbf{L} \end{bmatrix}. \tag{F.29}$$

Using the set $\mathcal{D}$, the following algorithm determines the scaling factor [106]:

1. *Compute the unconstrained control, and evaluate* $\mathbf{f}^u = \mathbf{F}\mathbf{B}^\dagger \mathbf{T}_c^u$,
2. *Set* $\zeta = 1$,
3. *If* $f^u(i) > f(i)$ *and* $f(i)/f^u(i) < \zeta$. *Then, re-set* $\zeta = f(i)/f^u(i)$. *Do this for all components* i *of* $\mathbf{f}^u$.

Once the scaling factor is computed the control can be implemented as

$$\mathbf{T}_c = \zeta \, \mathbf{T}_c^u. \tag{F.30}$$

Hence, the above algorithm must be run on-line at each sampling period. Figures F.6 and F.7 illustrate the controller in action. In this example, we assume that the right aileron is faulty (stuck at zero position) and saturations occur in the remaining actuators. As we can see, the actuators saturate at some point in the manoeuvre. These saturations are enforced by the motion controller through the input vector scaling. In Figure F.7, the middle plots show that the actual rates do not match the desired ones which will induce a degradation of the performance. However, the desired torque is always achievable (bottom plots) since the output of the motion controller is scaled down to provide the control allocation function with a feasible demand.

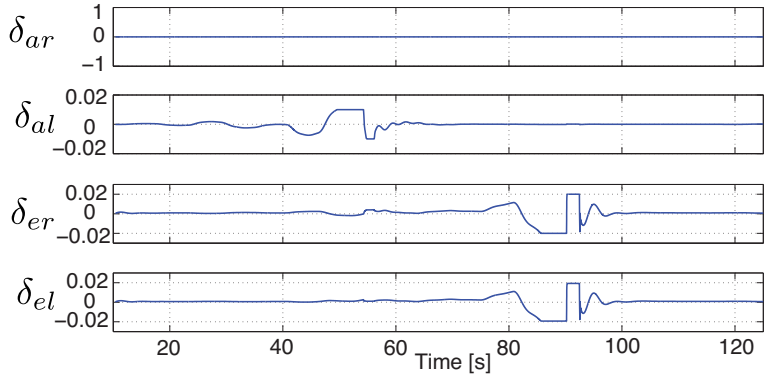

Figure F.6: Actuator activity for right aileron faulty plus saturation in the remaining surfaces.

The stability and robustness of these controllers are discussed in Appendix F.7.

F.4 Fault Diagnosis and Fault-tolerant Control

The fault detection is based on analysis of residual signals, which contain information about specific redundancies in the aircraft model and its instrumentation, and on estimation of essential parameters. The redundancies are used to detect whether components are faulty. Defects, whether they are temporal or permanent, will appear as a violation of the equations that describe normal behaviours of the UA. A complete set of analytic redundancy relations (ARR) for a system can be found by structural analysis, see [19] and references herein. Based on measured and other known variables, the ARR's can be used directly as generators for residual signals and also used as guideline for what potential residual generators exist for the system. A comprehensive structural analysis of a fixed wing aircraft was conducted by [50]. The analysis resulted in dependability matrices, which shows which faults have an impact on each of the AARs.

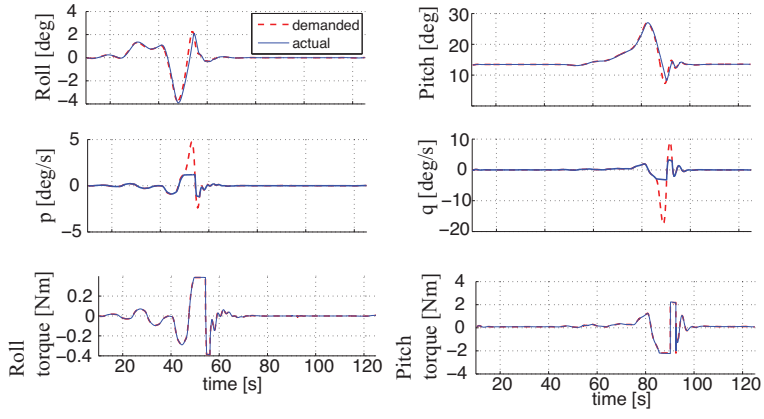

Figure F.7: Motion variables for the pitch and roll chanels.

If a particular fault has a unique signature in the set of ARR's, this fault is isolable. If the same set of ARR's respond to multiple faults, these faults are only group-wise isolable. The analysis in [50] showed that faults on all control surfaces were isolable in their particular set-up because ailerons and elevators were treated as two units, not as the four control surfaces that constitute the physical actuators. With the purpose of this paper, to isolate a single defect control surface and let fault-tolerant control techniques compensate for the loss of a single control surface, isolation need be obtained for the individual surfaces. Extension of the structural analysis in [50] shows that a fault in ailerons or elevators are only group-wise isolable, so faults in the individual control surfaces can not be distinguished by the residuals alone. If these faults should be isolated, active diagnosis is needed, where excitation signals are send to actuators [138] and, based on the system response, it is then possible to isolate which surface is faulty. Once a fault is isolated, remedial action is taken in the form of control surface re-allocation using the technique suggested in the previous section: in Equation (F.15). The fault detection system resets the parameter estimates and re-estimate them, in case a faulty actuator recovers from its fault.If more than one actuator fails, the aircraft may loose controllability. Hence, if a second fault is detected that causes loss of controllability, a signal informs the remote pilot or ground segment to trigger an emergency landing (*e.g.* by parachute).

F.4.1 Residuals for FDI

The ARR's found in [50] are based on the general nonlinear aircraft description and assumes measurements of α and β, which are not readily available on low cost UA's. The model includes force and torque constants for actuator deflec-

tions, which can be hard to obtain for UA's. Residuals based on a lower order model are used instead to achieve a less complex diagnosis setup with only basic instrumentation.
The AAR's obtained from structural analysis provides nonlinear residuals applicable for implementation. The general form of the residual vector is

$$\mathbf{r}(t) = \mathbf{g}_r(\mathbf{y}(t), \boldsymbol{\delta}_a, V, \boldsymbol{\Theta}) \tag{F.31}$$

where $\mathbf{g}_r$ is a function expressing the AARs, but for multiplicative faults, the parameter vector $\boldsymbol{\Theta}$ also comprises essential information, and the estimate $\hat{\boldsymbol{\Theta}}$ is also very useful for diagnosis [70]. With $\mathbf{g}_\Theta$ denoting a function to estimate the parameter gradient from input and measurements,

$$\dot{\hat{\boldsymbol{\Theta}}} = g_\Theta(\mathbf{y}(t), \boldsymbol{\delta}_a(t), V, \hat{\boldsymbol{\Theta}}). \tag{F.32}$$

where $\mathbf{g}_\Theta$ is a function to estimate the parameter gradient from input and measurements. Estimation of parameters is also needed in (F.31) when parameters are unknown.
For linear analysis, residuals are often generated from the LTI model (F.11). A residual $\mathbf{r}$ should be independent of control input and disturbances. A residual generator has the general LTI form,

$$\mathbf{r}(s) = \mathbf{V}_{ry}\mathbf{y}(s) + \mathbf{V}_{r\delta_a(t)}\delta_a(s) \tag{F.33}$$

where $\mathbf{y}$ are measurements and the matrices $\mathbf{V}_{ry}$ and $\mathbf{V}_{ru}$ are determined from the LTI dynamics through solving a left nullspace problem [19, 41] and references herein,

$$[\mathbf{V}_{ry}\mathbf{V}_{ru}] \begin{bmatrix} \mathbf{H}_{\omega\delta}(s|V,\theta) & \mathbf{H}_{\omega d}(s|V,\theta) \\ \mathbf{I} & \mathbf{0} \end{bmatrix} = \mathbf{0} \tag{F.34}$$

The LTI analysis confirms that isolability is not obtained for individual faults in elevators or ailerons. Individual faults are detectable but not isolable in the common diagnostic approach. Recognition of signatures in output or residuals also require that unknown parameters in $\boldsymbol{\Theta}$ are estimated.
The combination of parameter estimation (F.32) and the residual generator (F.31) or (F.33) form an adaptive scheme that is explored below.

F.4.2 Active fault diagnosis

Active diagnosis is based on applying a test signal on control inputs and observe the responses from input to output from (F.11) or input to residual from (F.33), [21], [98], [114], [53].
The fault diagnosis scheme then consists of two constructive steps: detection followed by isolation, the latter is active isolation when needed. First, the detection system analyses changes in on-line parameter estimates F.32 of low-order transfer function models. A large change in a residual or in parameters indicates

a fault but does not reveal which control surface may be faulty. In order to confirm the fault and isolate the faulty actuator, an auxiliary command signal is added to actuator commands, one at a time. Information collected from these tests allows the system to isolate the faulty actuator and make the appropriate decision about what control re-configuration is required. When a fault is isolated, the fault detection system resets the parameter estimates and re-estimate them, to determine if a faulty actuator should recover from its fault.

F.4.3 Parameter Estimation

The diagnosis system identifies the parameters of the transfer function from the actuator commands $\boldsymbol{\delta}_c$ to the motion rates $\mathbf{r}_{ate} = [p\ q]^\mathsf{T}$. These transfer functions are used to generate estimated rates $\hat{\mathbf{r}}_{ate} = [\hat{p}\ \hat{q}]^\mathsf{T}$, which are used to construct a residual vector $\mathbf{r} = \mathbf{r}_{ate} - \hat{\mathbf{r}}_{ate}$. In the faultless case, the residual vector is close to zero. A non-vanishing residual indicates the presence of a fault if gains and dynamics of the residual generator adequately match the UA behaviour.
A full aircraft model including all the dynamics and kinematics would not be practical for diagnosis. First, such models are difficult to obtain. Second, the amount of information gathered by the onboard sensors might not be enough to judge changes in a complex model. Therefore, high-order dynamics are neglected and first-order models are used. In the following, we use a small UA [44] and run simulations to illustrate the method.
Figure F.8 shows a response of a nonlinear UA model in pitch rate to a doublet in the command $\delta_q = \delta_{al} + \delta_{ar} + \delta_{el} + \delta_{er}$. From this response, we can see that a first-order approximation would capture the essential dynamics. Similar results are obtained for roll rate with the input $\delta_p = \delta_{al} - \delta_{ar} + \delta_{el} - \delta_{er}$. Transfer

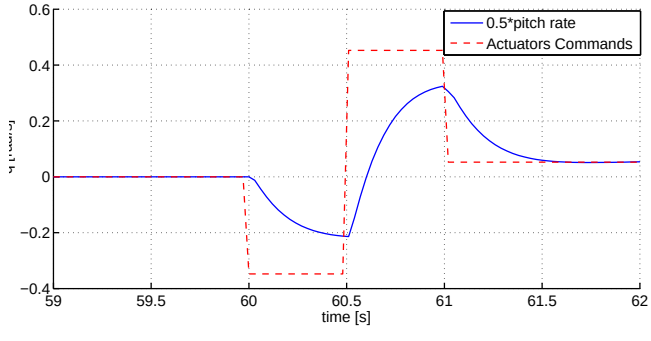

Figure F.8: Pitch rate response of a nonlinear UA model to a doublet in the actuators such that $\delta_q = \delta_{al} + \delta_{ar} + \delta_{el} + \delta_{er}$.

functions corresponding to the two channels (roll and pitch), are $\hat{H}_p(z)$ and

$\hat{H}_q(z)$ respectively, and are denoted by

$$\hat{H}_p(z) = \frac{b_p}{z - a_p} \qquad \text{and} \qquad \hat{H}_q(z) = \frac{b_q}{z - a_q} \tag{F.35}$$

The parameter estimation is easily done using a recursive least-squares algorithm. Parameters of a discrete-time first order system are estimated,

$$y_n = a\, y_{n-1} + b\, u_{n-1} + c, \tag{F.36}$$

where $\mathbf{\Lambda} = [a\ b\ c]^T$ is the vector of parameters and $\mathbf{\Gamma} = [y_{n-1}\ u_{n-1}\ 1]^T$ the regressors. The c parameter is added to catch any stationary offsets. The algorithm is summarised as

$$\varepsilon_n = y_n - \mathbf{\Gamma}_n^T \hat{\mathbf{\Lambda}}_n, \tag{F.37}$$

$$\boldsymbol{P}_n = \left(\boldsymbol{P}_{n-1}^{-1} + \mathbf{\Gamma}_n \mathbf{\Gamma}_n^T\right)^{-1}, \tag{F.38}$$

$$\hat{\mathbf{\Lambda}}_n = \hat{\mathbf{\Lambda}}_{n-1} + \boldsymbol{P}_n \mathbf{\Gamma}_n \varepsilon_n, \tag{F.39}$$

where ε is the error between the observed output and the estimate, $\boldsymbol{P_0}$ is the 3-by-3 identity matrix and $\hat{\mathbf{\Lambda}}$ the vector of the estimates.

This algorithm needs persistence of excitation. This is achievable during normal manoeuvres with a UA but in case of some fault is detected, rapid isolation and estimation of new parameters is essential. The latter requires a dedicated excitation. Performing dedicated manoeuvres after a fault is detected, but not isolated, is a standard procedure but may constitute a risk to the UA.

F.4.4 Nullspace Injection

Instead, we propose a method to excite periodically the actuators without affecting the motion of the aircraft and ensure a quick detection and estimation of parameters of the faulty UA. To do so, we add an excitation signal to the actuator commands in the null space of the actuator configuration matrix $\mathbf{B}$ (equation F.17) used for control allocation. Namely,

$$\mathbf{T}_c = \mathbf{B}\,(\boldsymbol{\delta} + \boldsymbol{\delta}_{null}). \tag{F.40}$$

By doing a singular value decomposition of $\mathbf{B}$, we can obtain an orthonormal basis $\mathbf{n}_1, \mathbf{n}_2$, for the null space of $\mathbf{B}$. Then we can generate a test signal as a linear combination of the vectors in this basis:

$$\boldsymbol{\delta}_{null} = a_1(t)\,\mathbf{n}_1 + a_2(t)\,\mathbf{n}_2, \tag{F.41}$$

where $a_i(t)$ are chosen to be sinusoidal signals of a test frequency ω_t. Because $\boldsymbol{\delta}_{null}$ is in the null space of $\mathbf{B}$, the commanded torques $\mathbf{T}_c$ in (F.40) depend only

on $\boldsymbol{\delta}$. If there is a fault, however, the motion of the aircraft will exhibit the test frequency ω_t.
Figures F.9 and F.10 show an example of how null space signal injection works. In this scenario, one-and-a-half periods of a sinusoidal null space test signal is injected into the actuator commands every 20s. Figures F.9 shows the desired and actual actuator deflections, and Figure F.10 shows the pitch and roll rates. At $t = 45s$ in the simulation, a fault is injected whereby the right aileron becomes stuck in the current position. As we can see from Figure F.10, once the fault occurs, the test frequency appears in the rate variables when the test signal is injected. Since the fault is on one of the ailerons, the roll rate is much more affected than the pitch rate. If periodic injection should be unwanted, the nullspace injection could take mplace when the disgnoasic algorithm has detected a deviation from normal behaviour.
Figure F.11 shows a block diagram of the diagnosis system. We use both residuals analysis and changes in the parameter estimates to detect the faults. This redundancy allows a simplified tuning of the detection thresholds and hence makes the tuning easier. Both methods are discussed in the following.

Fault Diagnosis through Residual Analysis

To diagnose faults in the ailerons and the elevators, we consider the following residuals (evaluated at each sample time t_i)

$$r_p(i) = p(i) - \hat{p}(i), \tag{F.42}$$
$$r_q(i) = q(i) - \hat{q}(i) \tag{F.43}$$

where the estimates are obtained from the affine state-space model (F.36) with the following inputs respectively:

$$u^p = \delta_p = \delta_{al} - \delta_{ar} + \delta_{el} - \delta_{er},$$
$$u^q = \delta_q = \delta_{al} + \delta_{ar} + \delta_{el} + \delta_{er}.$$

In the fault-free case, the residuals r_p and r_q are close to zero. The presence of a fault is observed when r_p and r_q are no longer close to zero but have an offset. We assume the measurements to be affected with White Gaussian Noise (WGN) of unknown variance. Hence, the detection problem is to detect an offset level in WGN with unknown amplitude and variance. Lets consider a null hypothesis $\mathcal{H}_0$ where the estimated model matches the real system. In that case, the residuals are WGN with zero mean and unknown variance. The alternative hypothesis $\mathcal{H}_1$ expresses the differences between the model and the real system. Under $\mathcal{H}_1$, the residuals are WGN with constant offset and unknown variance. In [77] this problem is solved using the generalised likelihood ratio test (GLRT);

$$\left.\begin{array}{ll} \mathcal{H}_0: & r_{p/q}(n) = \mathrm{WGN}(n), \\ \mathcal{H}_1: & r_{p/q}(n) = A + \mathrm{WGN}(n) \end{array}\right\} n = 0, 1, ..., N-1, \tag{F.44}$$

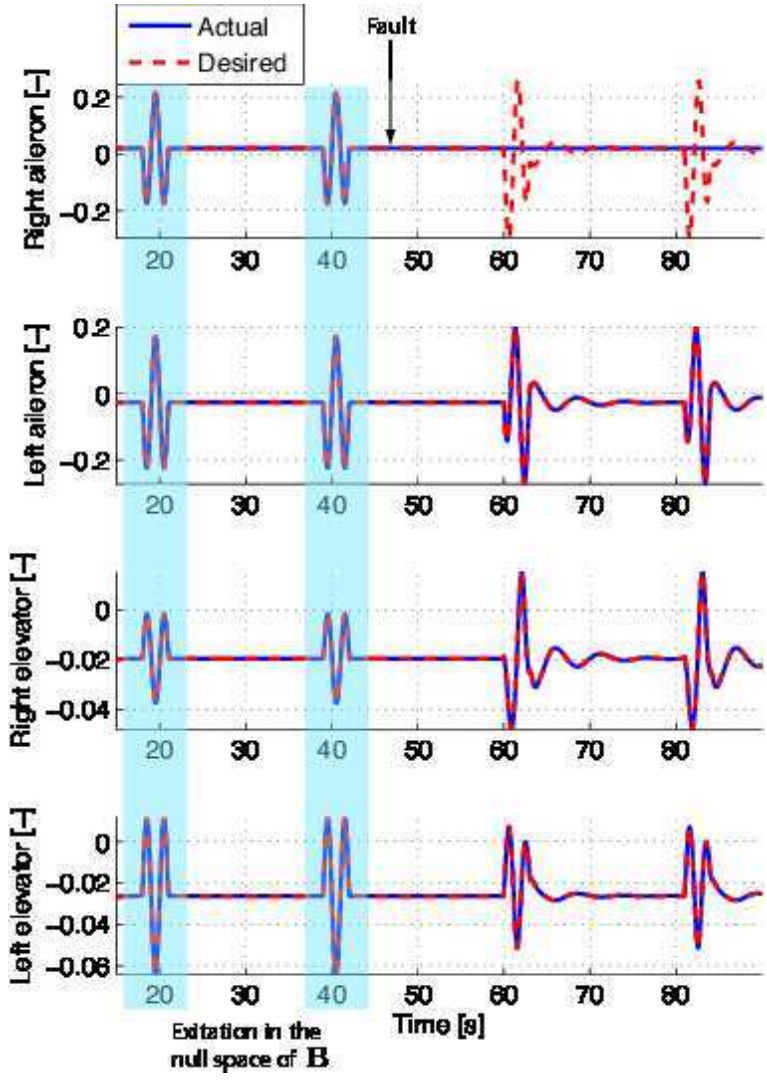

Figure F.9: Desired and actual actuator deflections.

where A is an unknown offset constant level and WGN(n) has an unknown variance σ^2. The test is considered for a sliding window of N samples. With the classical linear model $\mathbf{x} = \mathbf{H}A + \mathbf{w}$, where $\mathbf{H} = [\ 1 \quad 1 \quad \dots \quad 1\ ]^T$ and $\mathbf{w}$ is an $N \times 1$ noise vector with density function $\mathcal{N}(\mathbf{0}, \sigma^2\mathbf{I})$. For each residual ($\mathbf{r_p}$, $\mathbf{r_q}$),

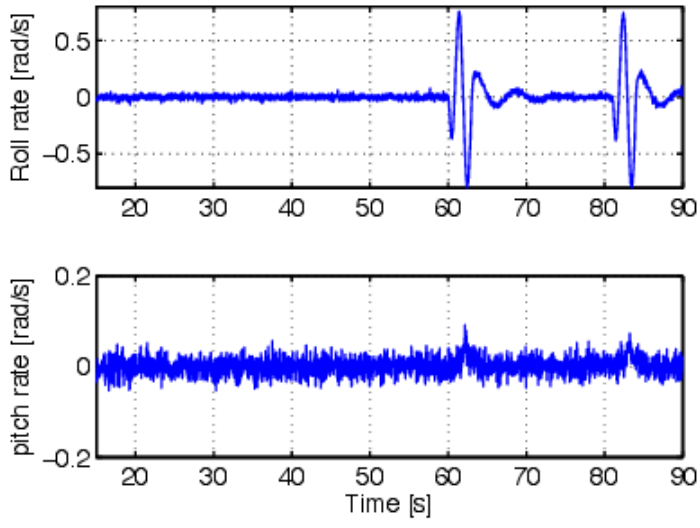

Figure F.10: Roll and pitch rates measurements.

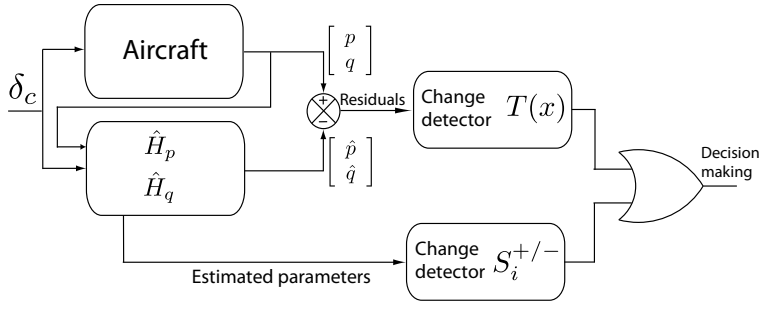

Figure F.11: Redundant fault detection.

the hypothesis test expressed as a parameter test is

$$\begin{aligned} \mathcal{H}_0 : &\quad A = 0, \sigma^2 > 0, \\ \mathcal{H}_1 : &\quad A \neq 0, \sigma^2 > 0. \end{aligned} \tag{F.45}$$

The GLRT can be simplified to

$$T(x) = (N-1)\frac{\bar{x}^2}{\hat{\sigma}_1^2} > \gamma, \tag{F.46}$$

where $\bar{x}$ is the mean value of the residuals over N samples, $\hat{\sigma}_1^2$ is the sample variance estimator, and γ is a tuning parameter used to trigger the fault detec-

tion alarm—see [77] (p346).

To illustrate the performance of the detection method, we consider the scenario depicted in Figures F.9 and F.10 where the right aileron becomes stuck at $t = 45s$. The top plot in Figure F.12 shows the evolution of the parameters estimates via RLS. The fault is clearly seen as parameter changes at $t = 60s$ when the test signal is injected. The middle plot shows the residuals of the roll channel. At each time i, $r_p(i) = p(i) - \hat{p}(i)$. The bottom plot shows the result of the test statistic (GLRT) and the threshold γ: when $T(x) > \gamma$, $\mathcal{H}_1$ is the most likely hypothesis.

Parameter change detection

To detect any changes in the estimated parameters, we can use the cumulative sum (CUSUM) statistic [9] and references herein. The two-sided CUSUM algorithm is given by

$$S_i^+ = \max(0, S_{i-1}^+ + Q_i - \kappa), \text{and} \quad \text{(F.47)}$$

$$S_i^- = \max(0, S_{i-1}^- - Q_i - \kappa). \quad \text{(F.48)}$$

where Q_i is the current parameter update and κ the parameter which quantifies its mean value up to the time i. We trigger the alarm if S_i^+ or S_i^- is greater than γ'—a tuning parameter. When a fault occurs, the parameter variation leads to a jump in S_i^+ or S_i^-. Figure F.13 shows the parameter estimates for the roll channel (following model (F.36)) and the cumulative sum for the parameter a. The variations in the estimate are detectable through their CUSUM as shown in the bottom plot. Similar results are obtained for parameter b. The variations in c are not important enough to be reflected in the CUSUM. When $S_i^{+/-}$ exceeds γ', the alarm is triggered. One can notice that the CUSUM returns to zero when the parameters are re-estimated after the fault detection and isolation so the system is ready to detect another fault.

F.4.5 Active Fault Isolation

Supplemental to the nullspace injection, further certainty that the faulty actuator has been correctly identified can be obtained with the traditional active diagnosis technique [114] where a high-frequency signal (δ_{ext}) is injected to the actuator commands in a sequence—one at a time in each actuator—to validate isolation of the defect. This is illustrated in Figure F.14. This validation would require some excitation during the flight, and take some time since several periods of the excitation signal is used, but with the already performed nullspace injection, it is likely that the correct remedial action has already been taken,

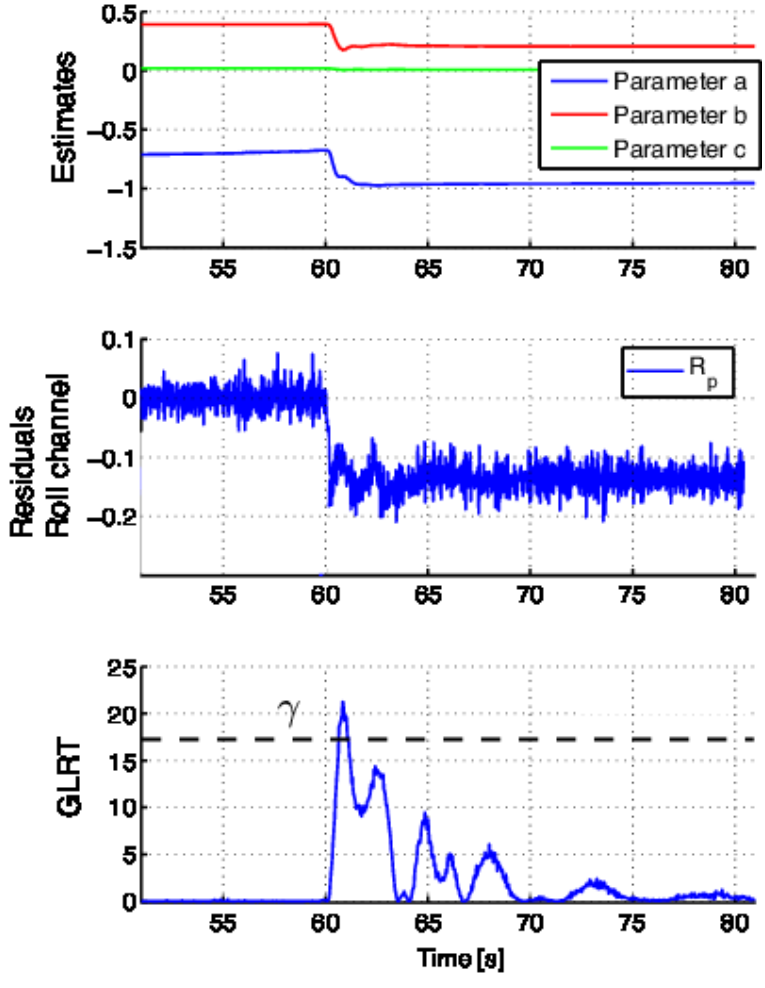

Figure F.12: Top plot: Parameter estimation using RLS. Middle plot: Residuals for the roll channel. Bottom plot: Generalised likelihood ratio test.

hence enhancing the likelihood that a fault is detected and a correct reconfiguration action is taken timely enough to ensure the safety of the UA by keeping it within its allowed flight envelope. The active nullspace injection hence enhances the *coverage* of this fault-tolerant control approach [134].

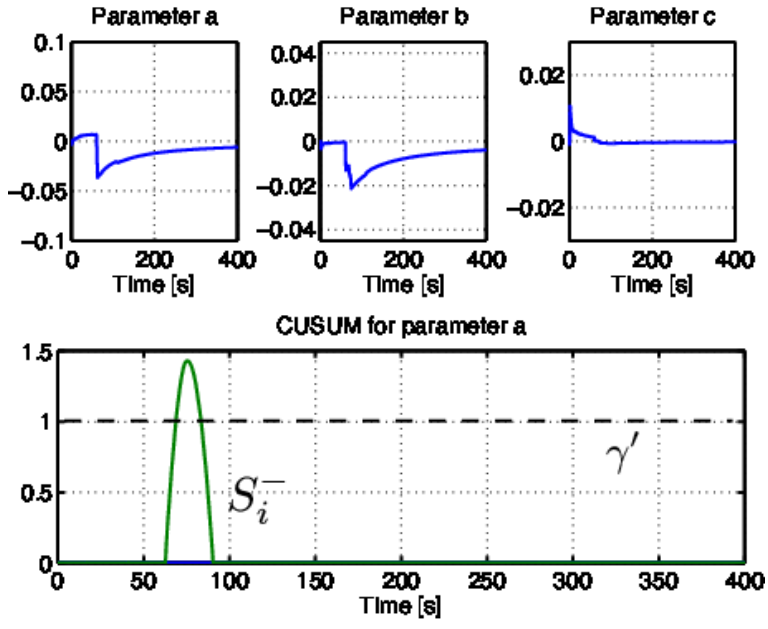

Figure F.13: Estimated parameters fitting model (F.36) and CUSUM for parameter a.

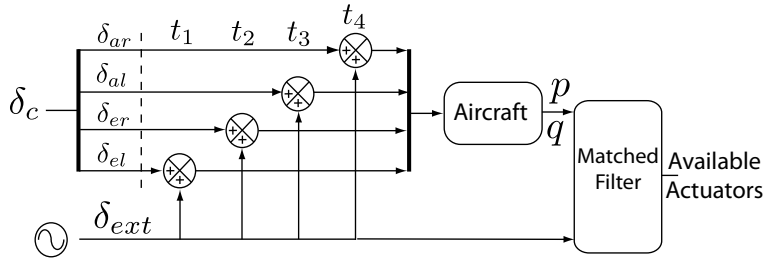

Figure F.14: Active diagnosis system.

Fault isolation scheme

In order to isolate the faulty actuator, we use a matched filter, which is a generalised replica-correlator [77] that detects the presence of a known signal s in Gaussian white noise. The detection of the signal s can be posed as a test of two hypothesis:

$$\left.\begin{array}{ll} \mathcal{H}_0: & x(n) = w(n) \\ \mathcal{H}_1: & x(n) = w(n) + s(n) \end{array}\right\} n = 0, 1, ..., N-1, \tag{F.49}$$

where N is the data (number of samples) used for the testing. The correlation of the data x and the known signal s (or its replica) is computed by the matched filter:

$$MF(x) = \sum_{n=0}^{N-1} x(n)s(n). \tag{F.50}$$

The output of the matched filter MF grows in value if the signal s is present in x. The threshold for triggering the frequency detection is based on a Log-likelihood ratio test which validates the hypothesis $\mathcal{H}_1$. A parameter γ'' is tuned such that an alarm is triggered if $MF(x) > \gamma''$. The tuning parameters for the roll and pitch channels are respectively γ''_p and γ''_q.
Figure F.15 shows the desired and actual actuator deflections for a sequence of detection and isolation. The signals highlighted at about 40s correspond to the detection signals which are in the null space of the actuator configuration matrix for the nominal or healthy actuator set. A fault occurs at 45s, and it is detected when the detection signal is injected at 60s. Once the fault is detected, the sequence of high-frequency bursts are injected sequentially in each actuator. Once the faulty actuator is isolated, the controller is reconfigured, and a new signal for testing is injected in the null space of the current actuator configuration. A testing signal is still sent to the faulty actuator in case it recovers from the fault. The excitation signal δ_{ext} used for isolation is of amplitude 0.1 and frequency $2.5Hz$. Figure F.16 shows the corresponding roll and pitch rates, and Figure F.17 shows the output of the matched filters with the associated thresholds γ'_p and γ'_q. For healthy actuators, $MF(x)$ increases when the frequency of δ_{ext} is found in the roll or pitch rate. Figure F.18 shows the rate observation window and the trigger (binary signal) due to the filter detection. This figure shows the lack of response of the right aileron, which is then identified as the fault actuator.

F.5 Case Study using a Specific Part of a Mission

As a case study, we consider an aircraft approaching for landing in a wind with speeds around 10kt. The UA is required to fly through the waypoints at constant airspeed, $V_T = 30\,ms^{-1}$ with a 10 knots wind in positive North direction. The wind turbulence model is taken from [78].

Figure F.19 shows the waypoints, the desired path, the actual trajectory for the nominal case and for two scenarios:

1. Fault not accommodated,
2. Fault accommodated by the proposed fault-tolerant flight control system.

Figure F.20 shows the actuator deflections for the nominal case. The achieved trajectory is shown Figure F.21. From these figures, we observe that the autopi-

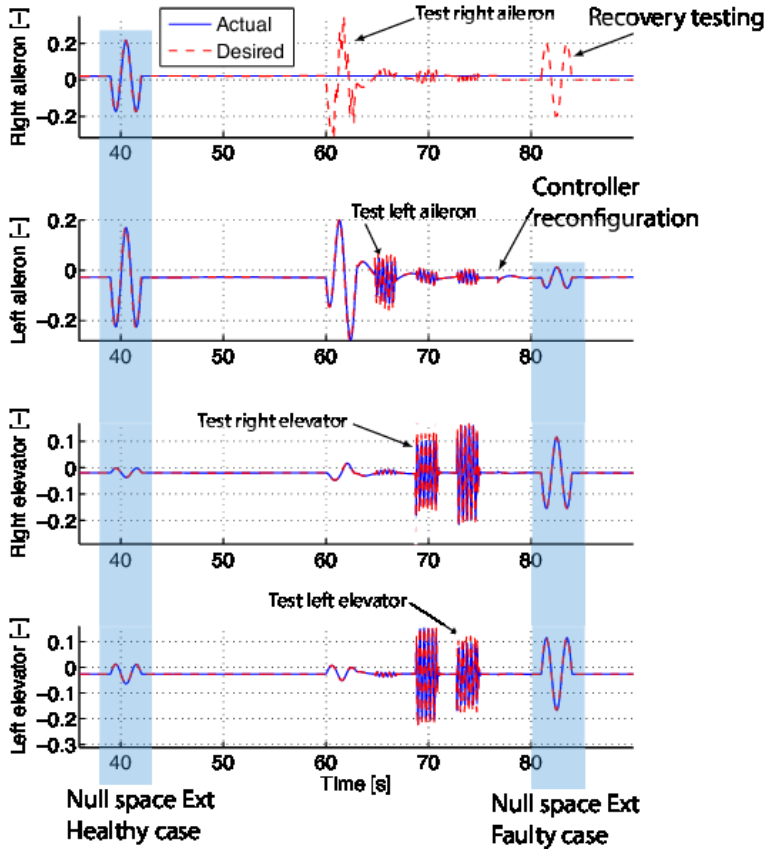

Figure F.15: Actual and desired actuator deflections.

lot performs well in the nominal case, and the actuators do not reach saturations. We then consider a case where we introduce a fault at time $t = 45s$; the right aileron is stuck at its current position. Figure F.22 shows the actuator deflections for the faulty case. After $t = 45s$, the right aileron does not follow the desired command and then the fault detection system detects the presence of a fault. It then performs the active diagnosis analysis which isolates the faulty actuators. In Figure F.22 we can see the active diagnosis excitation signal added to the command signal to isolate the fault. When the fault is isolated, the desired command of the right aileron is set to zero. The control allocation matrix in (F.17) has been reconfigured according to the fault detected. Figure F.22 also shows more demand in the left aileron and an asymmetric elevator activity used to produce roll moment. The autopilot performs well even in presence of faults. Finally, we repeated the simulation with the same fault occurring at the time

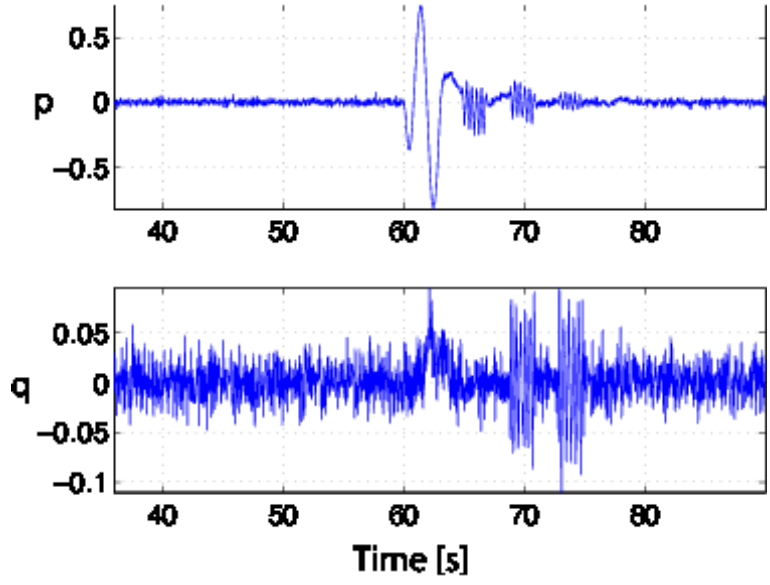

Figure F.16: Roll and pitch rate with measurement noises.

but without informing the controller and with the anti-windup not active. Figures F.23 and F.21-c show the results for this scenario, in which the aircraft control is lost.

F.6 Conclusion

This paper presented a framework for joint motion control and control allocation which does not require on-line optimisation. Furthermore, the approach was shown to ensure that the output of the motion controller always provides feasible commands to the control allocation. An algorithm was proposed to allocate control surfaces to obtain the required output of the controller taking into consideration the saturations and constraints of the actuators as well as possible failure of an actuator. Fault diagnosis was provided in two steps: detection and isolation. The detection used an adaptive residual generator followed by statistical analysis for change detection. Fault isolation was shown possible using active isolation techniques and a new approach was suggested, designing test signals to belong to the null space of actuator output hence making minimal disturbances of the flight. Adaptive detection and isolation was tuned and tested on real flight data where cases of actual control surface faults occurred. Robust stability was furthermore proven for the flight control system.
A comprehensive simulation study illustrated the performance of the FCS. The

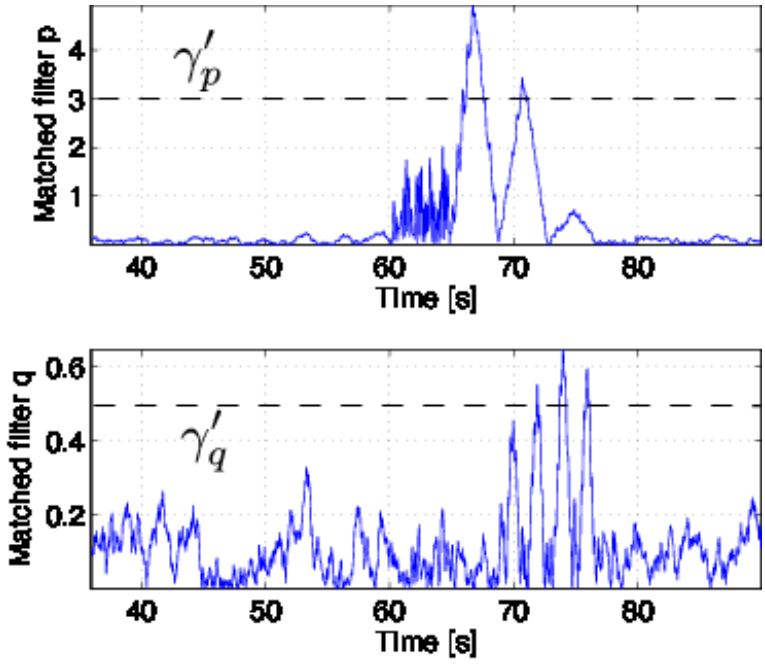

Figure F.17: Matched filters output in roll and pitch.

nominal case of closed loop guidance was compared with cases with realistic fault scenarios. When fault-tolerant control was not active, the aircraft was lost. With fault-tolerant control, the flight control system detected and isolated control surface faults within a reasonable time (about 10 seconds). Then, it reconfigured the control allocation without changing the motion control laws and the aircraft performed the mission. Even with the presence of a control surface fault the UA remained stable and still followed the desired trajectory with acceptable degradation of performances.

F.7 Paper Appendix

F.7.1 Stability and robustness

This appendix shows stability of the proposed autopilot in the presence of actuator saturation. The controller for pitch, has a proportional controller K_θ and a PI controller for the rate loop of the form given in (F.25). The controller for

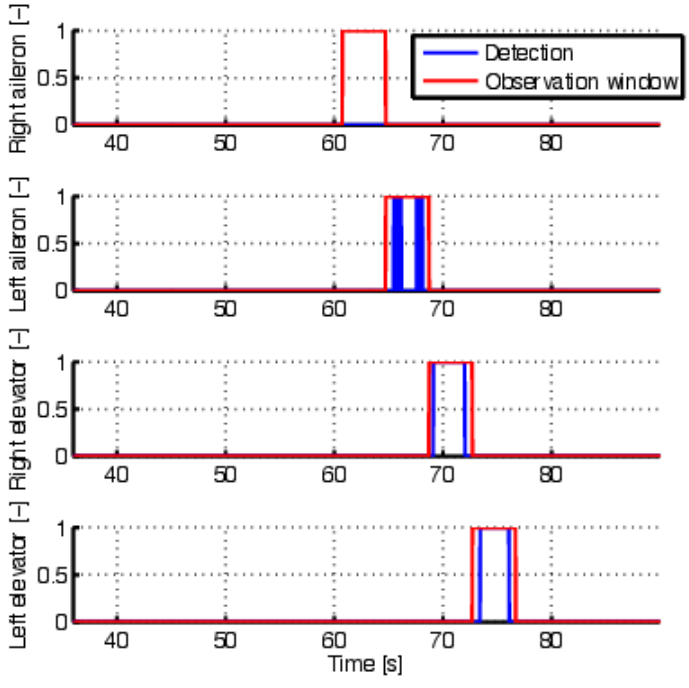

Figure F.18: Observation window and detection trigger.

altitude is a PI with parameters K_h and T_h.

$$G_q(s) = \frac{q(s)}{M_q(s)} = \frac{\hat{K}_q}{\hat{T}_q\, s + 1}. \tag{F.51}$$

This model follows from the physics of the problem whereby the damping in pitch is approximated by a constant gain. In the following, we consider the altitude controller channel but a similar study leads to the same results for the lateral controller. We also provide warranties in terms of robustness for the controller with respect to the model uncertainties by careful choice of its parameters.

problem description

Consider the feedback interconnection in Figure F.24. The unforced system is, in state space form,

$$\dot{x} = \mathbf{A}x + \mathbf{B}\tau, \tag{F.52}$$

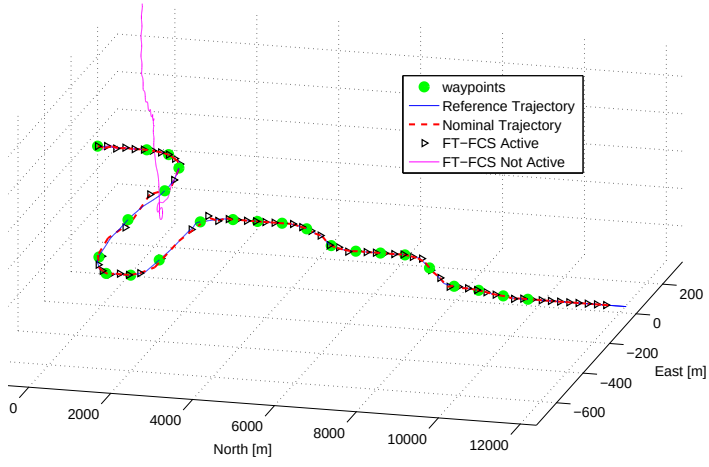

Figure F.19: Reference and actual trajectories under different scenarios.

$$y = \mathbf{C}x + \mathbf{D}\tau, \tag{F.53}$$

$$\tau = -\psi(t, y), \tag{F.54}$$

where $x \in \mathbb{R}^n$, τ and $y \in \mathbb{R}^p$, $(\mathbf{A}, \mathbf{B})$ is controllable and $(\mathbf{A}, \mathbf{C})$ is observable, Then $\{\mathbf{A}, \mathbf{B}, \mathbf{C}, \mathbf{D}\}$ is a minimal realisation of $G(s)$,

$$G(s) = \mathbf{C}\left[s\mathbf{I} - \mathbf{A}\right]^{-1}\mathbf{B} + \mathbf{D}. \tag{F.55}$$

Furthermore, $\psi : [0, \infty) \times \mathbb{R}^p \to \mathbb{R}^p$ is a memoryless, possibly time varying, nonlinearity piecewise continuous in t and locally Lipschitz in y where the nonlinearity belongs to a specific sector. For all the nonlinearities belonging to this sector, if we succeed in showing that the origin is uniformly asymptotically stable, then the system is said to be absolutely stable. This problem is known as the Lure's problem [79].

The nonlinear feedback (saturations) belongs to a specific sector, $[\alpha, \beta]$, which are not related to the angles of the same names. The state space model of the linear component and its transfer function $G(s)$ are:

$$x = \left[x_1, x_2, x_3, x_4, x_5\right]^T, \tag{F.56}$$

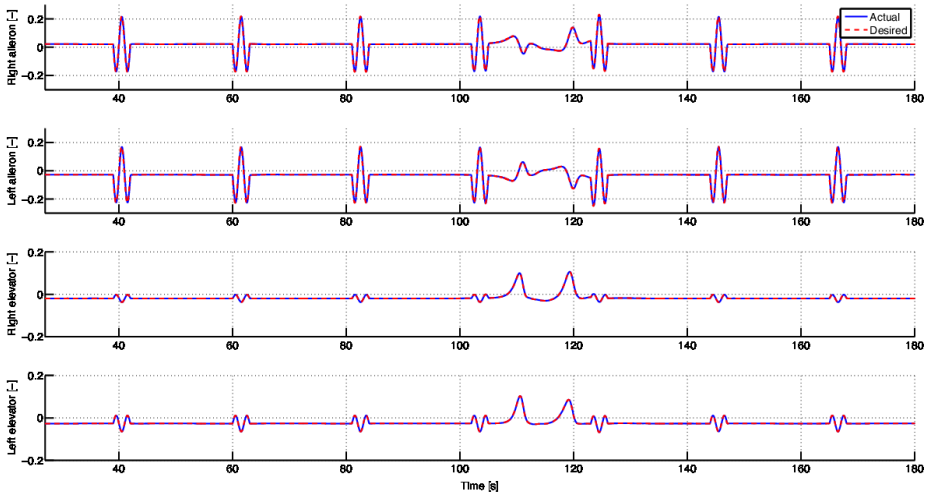

Figure F.20: Actuator activity - Nominal case.

$$\mathbf{A} = \begin{bmatrix} -\frac{1}{T_1} & 0 & 0 & 0 & 0 \\ \frac{K_1}{T_1} & 0 & 0 & 0 & 0 \\ 0 & K_2 & 0 & 0 & 0 \\ 0 & 0 & 0 & -\frac{1}{T_0} & 0 \\ 0 & 0 & K_h & 0 & 0 \end{bmatrix}, \quad \mathbf{B} = \begin{bmatrix} 1 \\ 0 \\ 0 \\ -\frac{1}{K_p} \\ 0 \end{bmatrix}, \tag{F.57}$$

$$\mathbf{C} = K_p \begin{bmatrix} \frac{K_1}{T_1} & P & PK_h & \frac{1}{T_0} & \frac{P}{T_h} \end{bmatrix}, \quad \mathbf{D} = 0. \tag{F.58}$$

We must check the conditions for controllability and observability to ensure a minimal realisation of $G(s)$ where

$$G(s) = \frac{y}{\tau}(s) = \mathbf{C}\left[s\mathbf{I}_5 - \mathbf{A}\right]^{-1}\mathbf{B}. \tag{F.59}$$

After computation, it is obvious that $G(s)$ is not Hurwitz. Thus, the best we can hope is to prove the absolute stability with a finite domain.

Absolute stability

Lets call $Z(s) = \frac{1+\beta G(s)}{1+\alpha G(s)}$. To satisfy the circle criterion, $Z(s)$ must be strictly positive real (see [79]). Since the nonlinear function $\psi(t, y)$ is the saturation, it belongs to the sector $[0, 1]$. For the following, we set $\beta = 1$ which is the upper limit of the sector. α determines the domain of absolute stability. The function $Z(s)$ is SPR if

$$Re\{Z(s)\} = Re\{\tfrac{1+G(j\omega)}{1+\alpha G(j\omega)}\} > 0 \,\forall \omega \in \mathbb{R}. \tag{F.60}$$

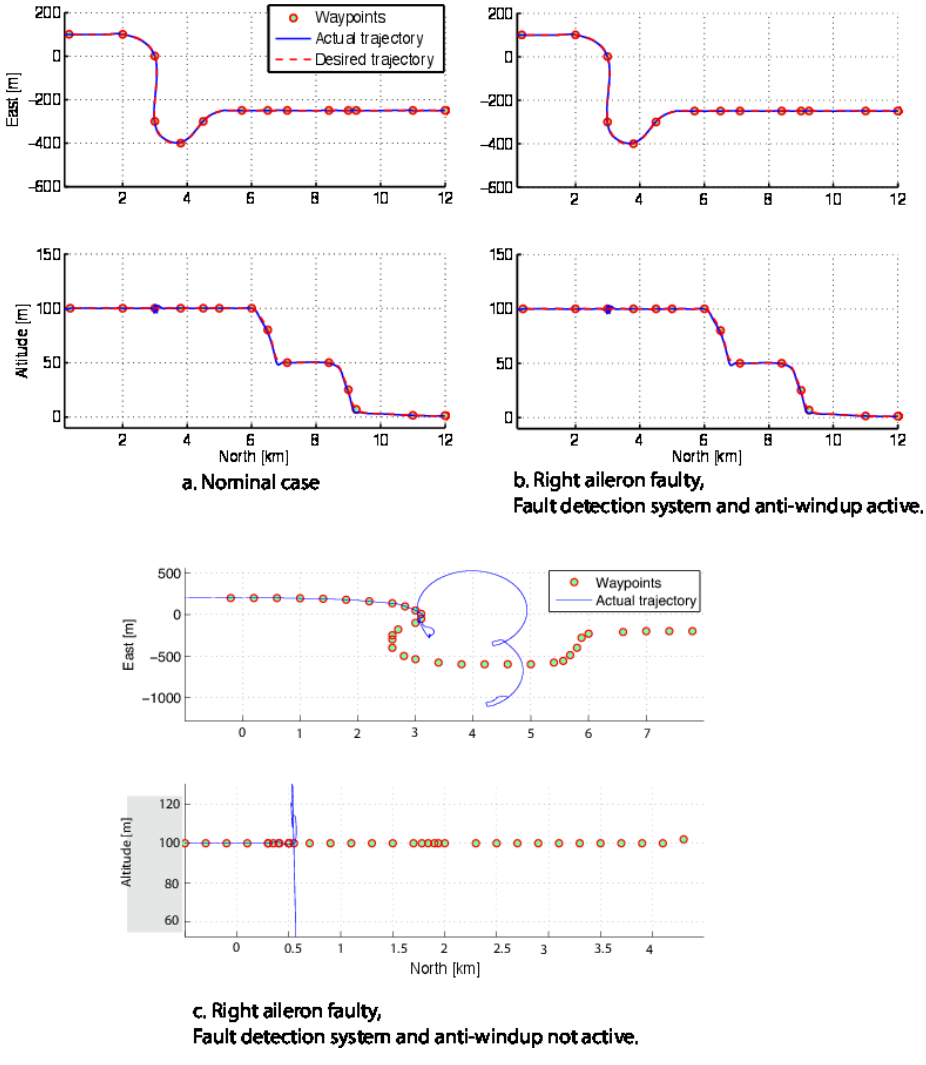

Figure F.21: Waypoints, actual and desired trajectories.

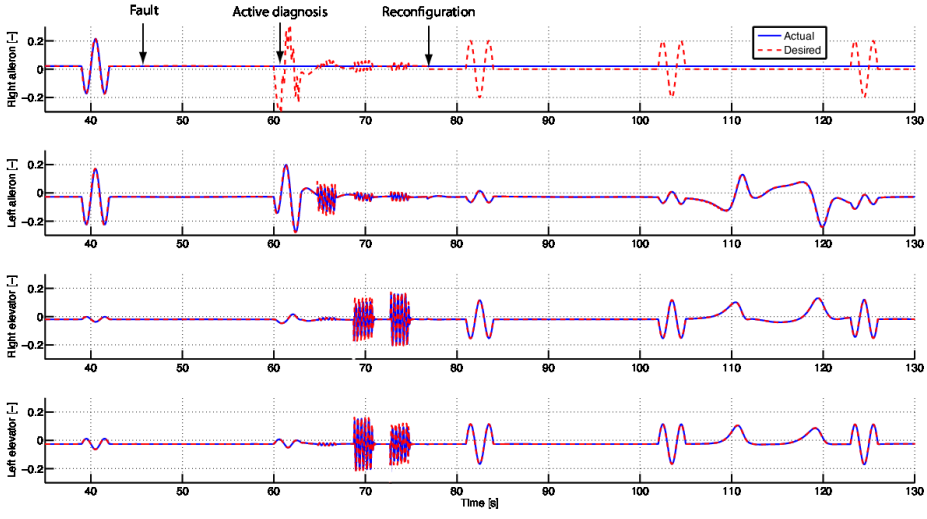

Figure F.22: Actuator activity - right aileron faulty, fault detection system and anti-windup active.

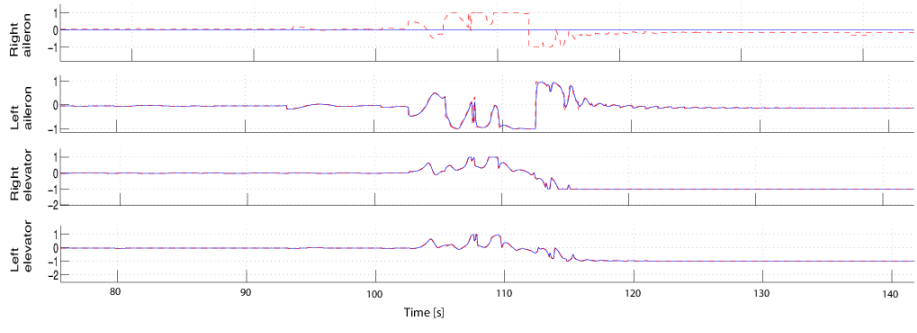

Figure F.23: Actuator activity - right aileron faulty, fault detection system and anti-windup not active.

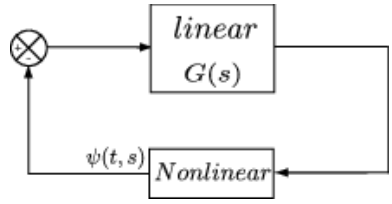

Figure F.24: Feedback connection, Lure's problem

The sector condition is satisfied on the interval $[-\frac{1}{\alpha}, \frac{1}{\alpha}]$.
The analytical study gives constraints on the controller parameters, K_h, T_h, T_0, K_p and P, and the sector boundaries, α and β to ensure the minimal realisation of $G(s)$ and the strictly positive realness of $Z(s)$.
The tuning of the controller and the choice of the sector allow to build the function $Z(s)$ such that it is SPR [38]. Conditions for a transfer function $Z(s) = \frac{a(s)}{b(s)}$ to be SPR includes that $a(s)$ belongs to a Kharitonov set and the coefficients of the numerator of the real part of $Z(s)$ are strictly positive [6]
Corollary: The controller proposed in this paper has the transfer function of the linear part,

$$Z(s) = \frac{a(s)}{b(s)} = \frac{s^5 + fs^4 + gs^3 + hs^2 + is + j}{s^5 + as^4 + bs^3 + cs^2 + ds + e}, \tag{F.61}$$

That is, with the domain $[0; \alpha]$, if,

1. $f, g, h, i, j > 0$ such that $a(s)$ belongs to a Kharitonov set, and
2. $fa - b - g > 0$, $gb - fc + d - ha + i > 0$, $fe - gd + ja - bi + hc > 0$, $-eh - jc + id$ and $je > 0$,

then $Z(s)$ is SPR and hence the closed loop of the proposed controller is absolutely stable with a finite domain and robust to model uncertainties. ■

Region of attraction

A quadratic Lyapunov function $V(x) = x^T \mathbf{P} x$ is used to estimate the region of attraction. Lets recall the state model,

$$\begin{aligned}
\dot{x}_1 &= -\tfrac{1}{T_1} x_1 + \tau \\
\dot{x}_2 &= \tfrac{K_1}{T_1} x_1 \\
\dot{x}_3 &= K_2 x_2 \\
\dot{x}_4 &= -\tfrac{1}{T_I} x_4 - \tfrac{1}{K_p} \tau \\
\dot{x}_5 &= K_h x_3.
\end{aligned} \tag{F.62}$$

The Kalman-Yakubovich-Popov lemma requests the nonlinear feedback to belong to the sector $[0, \infty)$. This motives the loop transformation proposed in Figure F.25 given by

$$\begin{aligned} \tau &= -\alpha y + \tilde{\tau} \\ \tilde{y} &= (\beta - \alpha) y + \tilde{\tau}. \end{aligned} \tag{F.63}$$

The linear system becomes,

$$\dot{x} = \tilde{\mathbf{A}} x + \tilde{\mathbf{B}} \tilde{\tau} \qquad \tilde{y} = \tilde{\mathbf{C}} x + \tilde{\mathbf{D}} \tilde{\tau} \tag{F.64}$$

where,

$$\tilde{\mathbf{A}} = \begin{bmatrix} -\frac{1}{T_1}(\alpha K_p K_1 + 1) & -\alpha K_p P & -\alpha K_p K_h P & -\frac{\alpha K_p}{T_I} & -\frac{K_p \alpha P}{T_h} \\ \frac{K_1}{T_1} & 0 & 0 & 0 & 0 \\ 0 & K_2 & 0 & 0 & 0 \\ -\alpha \frac{K_1}{T_1} & -\alpha P & -\alpha K_h P & -\frac{2\alpha}{T_I} & -\frac{\alpha P}{T_h} \\ 0 & 0 & K_h & 0 & 0 \end{bmatrix}, \tag{F.65}$$

$$\tilde{\mathbf{B}} = \begin{bmatrix} 1 \\ 0 \\ 0 \\ -\frac{1}{K_p} \\ 0 \end{bmatrix}, \quad \tilde{\mathbf{C}} = (\beta - \alpha)\mathbf{C}, \quad \tilde{\mathbf{D}} = 1. \tag{F.66}$$

There is an ϵ such that $\tilde{G}(s - \frac{\epsilon}{2})$ is positive real and $[\frac{\epsilon}{2}\mathbf{I} + \tilde{\mathbf{A}}]$ is Hurwitz where

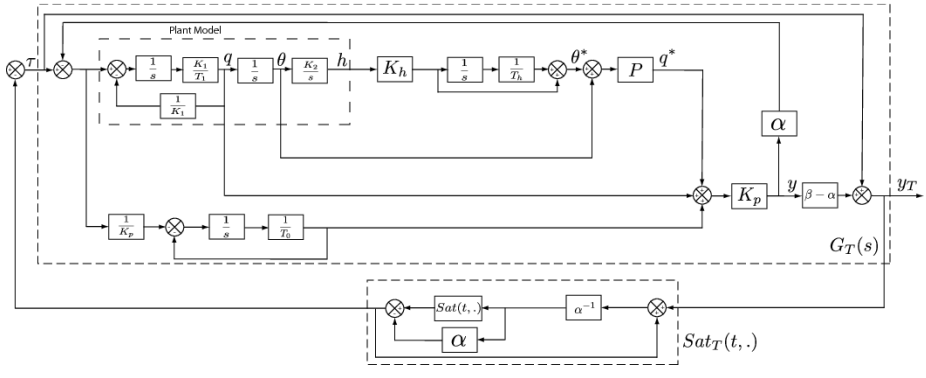

Figure F.25: Closed Loop Transformation to satisfy the sector $[0, \infty)$

$\tilde{G}(s) = \tilde{\mathbf{C}}(s\mathbf{I} - \tilde{\mathbf{A}})^{-1}\tilde{\mathbf{B}} + \tilde{\mathbf{D}}$. The matrix $\mathbf{P}$ is computed by solving the Riccati equation

$$\mathbf{P}\mathbf{A}_0 + \mathbf{A}_0^T \mathbf{P} - \mathbf{P}\mathbf{B}_0 \mathbf{P} + \mathbf{C}_0 = 0, \tag{F.67}$$

where $\mathbf{A}_0 = -\frac{\epsilon}{2}\mathbf{I} - \tilde{\mathbf{A}} + \tilde{\mathbf{B}}(\tilde{\mathbf{D}} + \tilde{\mathbf{D}^{\mathbf{T}}})^{-1}\tilde{\mathbf{C}}$, $\mathbf{B_0} = \tilde{\mathbf{B}}(\tilde{\mathbf{D}} + \tilde{\mathbf{D}^{\mathbf{T}}})^{-1}\tilde{\mathbf{D}^{\mathbf{T}}}$, and $\tilde{\mathbf{C_0}} = -\tilde{\mathbf{C}^{\mathbf{T}}}(\tilde{\mathbf{D}} + \tilde{\mathbf{D}^{\mathbf{T}}})^{-1}\tilde{\mathbf{C}}$ [79].

Under those conditions, the matrix $\mathbf{P}$ satisfies the Kalman-Yakubovitch-Popov equations.
Thus, $V(x) = x^T\mathbf{P}x$ is a Lyapunov function for the system. We estimate the region of attraction by

$$\Omega_c = \{x \in \mathbb{R}^5 | V(x) \leq c\} \tag{F.68}$$

where $c \leq min_{\{|y|=\frac{1}{\alpha}\}}V(x)$.

Test with a selected set of parameters

Table F.2 summarised the parameters used in simulation. The function $Z(s)$ is

Table F.2: Parameter values.

Parameter	Value
P	4.36
K_p	830
T_0	0.4
K_h	0.02
T_h	3
α	0.1

found to be Hurwitz, hence stability is ensured. To ensure robustness, we assume a variation of 20% of the plant parameters. We need to check if the numerator of $Z(s)$ is a Kharitonov polynomial; that is, its four characteristic polynomial must be Hurwitz. This is confirmed by applying the Routh's theorem to all of these. The matrix $\mathbf{P}$ satisfies the Kalman-Yakubovitch-Popov lemma where

$$\epsilon = 0.02,\ \mathbf{P} = 10^8 \begin{bmatrix} 0.0000 & 0.0061 & 0.0004 & 0.0119 & 0.0024 \\ 0.0061 & 4.2447 & 0.1861 & 5.0328 & 1.5293 \\ 0.0004 & 0.1861 & 0.0918 & 0.3662 & 0.0735 \\ 0.0119 & 5.0328 & 0.3662 & 9.9030 & 1.9866 \\ 0.0024 & 1.5293 & 0.0735 & 1.9866 & 1.7229 \end{bmatrix}, \tag{F.69}$$

$$\mathbf{L} = 10^3 \begin{bmatrix} -0.0923 & 3.8883 & 0.1319 & 4.9849 & 1.4174 \end{bmatrix}, \tag{F.70}$$

and $\mathbf{W} = \sqrt{2}$.
Thus, $V(x) = x^T\mathbf{P}x$ is a Lyapunov function for the system. We estimate the region of attraction by

$$\Omega_c = \{x \in \mathbb{R}^5 | V(x) \leq c\} \tag{F.71}$$

where $c \leq min_{\{|y|=\frac{1}{\alpha}\}} V(x)$. With the chosen parameters, $c = 3.2549$. Then choosing $c = 3.25$ we ensure Ω_c is contained in the set $\{|y| \leq \frac{1}{\alpha}\}$. The proposed controller is absolutely stable with the finite domain $[-\frac{1}{0.1}, -\frac{1}{0.1}]$ and robust to a 20% variation of the model parameters.